



## Experimental study of relative, turbulent diffusion

**Mann, J.; Ott, Søren; Andersen, J.S.**

*Publication date:*  
1999

*Document Version*  
Publisher's PDF, also known as Version of record

[Link back to DTU Orbit](#)

*Citation (APA):*  
Mann, J., Ott, S., & Andersen, J. S. (1999). *Experimental study of relative, turbulent diffusion*. Denmark. Forskningscenter Risoe. Risoe-R No. 1036(EN)

---

### General rights

Copyright and moral rights for the publications made accessible in the public portal are retained by the authors and/or other copyright owners and it is a condition of accessing publications that users recognise and abide by the legal requirements associated with these rights.

- Users may download and print one copy of any publication from the public portal for the purpose of private study or research.
- You may not further distribute the material or use it for any profit-making activity or commercial gain
- You may freely distribute the URL identifying the publication in the public portal

If you believe that this document breaches copyright please contact us providing details, and we will remove access to the work immediately and investigate your claim.

# Experimental Study of Relative, Turbulent Diffusion

Jakob Mann, Søren Ott & Jacob Sparre Andersen

Risø National Laboratory, Roskilde, Denmark  
September 1999

**Abstract** The purpose is to study relative turbulent diffusion under controlled, reproducible conditions in the laboratory in order to estimate the constant  $C$  in Richardson-Obukhov's law. We get  $C \approx 0.4 - 0.6$ . We furthermore measure the distance-neighbour function, which is the probability density function of the separation of two fluid particles that are initially close to each other. We find that the model proposed by Richardson is far superior to the one suggested by Batchelor.

To obtain these results we use the Particle Tracking (PT) technique to measure trajectories of fluid particles in a water tank with two oscillating grids generating turbulence. In the experiments reported here we have obtained Reynolds numbers based on Taylor's microscale of about one hundred. The PT system, which is also described in this report, consists of four CCD cameras, a synchronous light source and a recording system with two computers each equipped with a frame grabber card.

In the search for the best experimental methods we have revised the concept of local homogeneity and derived a law for the velocity-acceleration structure function. A second by-product of this effort is a relatively simple derivation of Kolmogorov's four-fifth law based on the assumption of local homogeneity.

Finally, we measure the full velocity structure tensor.

The Particle Tracking Project was sponsored by the Danish Technical Research Council under contract 9601244 "Eksperimentelt studium af relativ, turbulent diffusion" (Experimental study of relative, turbulent diffusion).

ISBN 87-550-2370-3; 87-550-2603-6 (Internet)  
ISSN 0106-2840

Information Service Department · Risø · 1999

# Contents

<b>1</b>	<b>Introduction</b>	<i>5</i>
<b>2</b>	<b>Apparatus and electronics</b>	<i>6</i>
2.1	Design of tank and turbulence generator	<i>6</i>
2.2	The particles	<i>11</i>
2.3	Cameras and light	<i>12</i>
2.4	Recording system	<i>16</i>
<b>3</b>	<b>From video data to particle tracks</b>	<i>16</i>
3.1	Determination of positions on images	<i>18</i>
3.2	Calibration and recalibration	<i>23</i>
3.3	Reconstruction of 3D positions	<i>26</i>
3.4	Tracking	<i>29</i>
3.5	Uncertainty of the position determination	<i>31</i>
<b>4</b>	<b>Basic flow characteristics</b>	<i>34</i>
4.1	Where are the velocities measured?	<i>36</i>
4.2	Mean flow	<i>36</i>
4.3	Standard deviations	<i>38</i>
4.4	The second order structure function	<i>39</i>
<b>5</b>	<b>Determination of the energy dissipation</b>	<i>42</i>
5.1	Method 0 – using global homogeneity	<i>44</i>
5.2	Method 2 – using local homogeneity	<i>45</i>
5.3	Method 3 – using global stationarity	<i>53</i>
5.4	Summary of results	<i>57</i>
<b>6</b>	<b>Kolmogorov’s four-fifth law</b>	<i>58</i>
<b>7</b>	<b>Relative dispersion</b>	<i>62</i>
7.1	The Distance–Neighbour Function	<i>64</i>
<b>8</b>	<b>Further investigations</b>	<i>67</i>
8.1	Expansion of the Eulerian velocity tensor	<i>67</i>
8.2	One particle Lagrangian autocorrelation functions	<i>71</i>
<b>9</b>	<b>Summary and conclusions</b>	<i>72</i>
	<b>Acknowledgments</b>	<i>73</i>
	<b>References</b>	<i>73</i>



# 1 Introduction

Turbulent diffusion is a subject of great importance for example in the assessment of consequences of industrial accidents. Today the risk assessment of accidental gas releases is based on absolute or single-particle diffusion models. These models predict the ensemble mean concentration field which typically is a very smooth distribution in space. In reality the instantaneous concentration fields are highly inhomogeneous and vary on short scales. For some purposes, such as the estimation of long term effects of pollution, the mean field is fully adequate. However, there is a series of cases of practical importance, where a description of the instantaneous concentration field is necessary, and where the determination of only the mean field is insufficient. One example is the assessment if the effect of an explosive gas, where the mean concentration could be below in the threshold of ignition, without this being the case of the actual, instantaneous concentrations.

Another issue of current interest is HF (hydrogenfluoride). HF is used in large quantities by the industry, among other things in the production of unleaded petrol, and the dispersion of HF is of serious concern for the industry and the environmental authorities. A special feature about HF is that it can transform into oligomers, such that the molecular weight depends strongly and non-linearly of the concentration. For a given *mean* concentration the density of the gas can therefore be lower or higher than air depending on how uneven the *actual* distribution of HF is. The question of whether a cloud of HF is buoyant is crucial for the risk assessment. Likewise, concentration fluctuations are of importance for odor perception, effects of toxic gases, and for chemical processes in the atmosphere in general.

A common ingredient in the processes is relative turbulent diffusion, i.e. the description of how turbulence disperses a “puff” of (fluid) particles (see figure 1). This *relative* dispersion of particles caused by the turbulent movements of the fluid is the subject of this project.

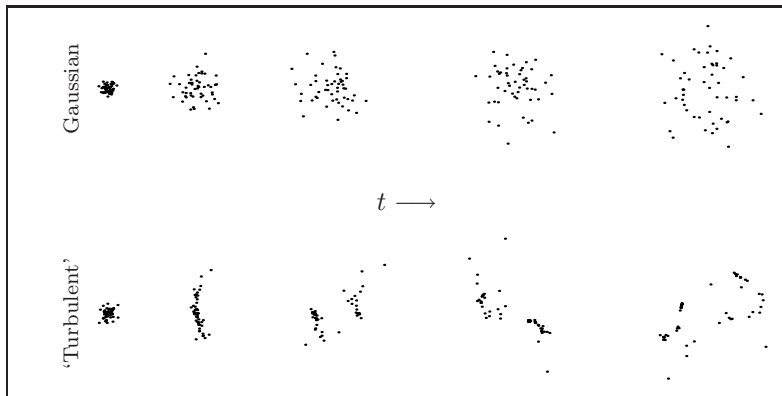


Figure 1. Sketch of the diffusion of two puffs with the same single particle statistics, but different two-particle statistics. Top: Molecular diffusion. Bottom: Turbulent.

A central issue in relative dispersion is the distance-neighbour function, which is, unfortunately, not very well determined experimentally. In the inertial subrange  $\langle \Delta r^2 \rangle = C \varepsilon t^3$ , where  $\Delta r$  is the distance between two fluid particles initially close to each other,  $\varepsilon$  the rate of specific, kinetic energy dissipation, and  $t$  the time (Richardson 1926, Obukhov 1941). This relation is by Monin and Yaglom (1975) called the most important result in relative, turbulent diffusion. Despite of this, the constant  $C$  is only determined within an order of magnitude and the theoretical

suggestions vary within two orders of magnitude (Kraichnan 1966, Larchevêque and Lesieur 1981, Mikkelsen 1982, Kristensen and Kirkegaard 1987, Thomson 1990, Ott 1992, Fung, Hunt, Malik and Perkins 1992). In other words, the second order moment of the distance-neighbour function is not well known. With respect to the shape of the function there are diverging opinions. In two classical works Batchelor (1952) and Richardson (1926) suggest a Gaussian shape and a more peaked shape, respectively. Recently, Virant and Dracos (1997) has given support to Batchelor’s model, while Jullien, Paret and Tabeling (1999) find Richardson’s model superior in a 2D flow, just as we do in a 3D flow.

The quantitative understanding of relative diffusion is currently rather rudimentary. Computation Fluid Dynamics (CFD) is of little use, since relative diffusion relies on the chaotic motions on small scales. The best methods available are direct numerical simulation (DNS) and experiments.

Kraichnan’s Lagrangian version of Direct Interaction Approximation (DIA) (Kraichnan 1966) may offer the best theoretical understanding, while random flight models can be a good solution for many practical purposes (Durbin 1980). These methods are based on various statistical assumptions, some of which are only weakly supported by experiments. One of the goals of this project is to provide experimental data for the investigation of these assumptions.

The report is organized as follows. The design of the experiment which involves choice of particles, configuration of cameras, design of light source, electronics and computer system is described in section 2. In section 3 the algorithms developed for extracting the three-dimensional particle positions from the video signals is presented. Basic flow characteristics are (section 4) mean flow, variances and second order structure functions. From these various length scales and the energy dissipation are derived. More fundamental ways of estimating the energy dissipation are considered in section 5 followed by a discussion of Kolmogorov’s four-fifth law (section 6). Finally, in section 7, we study relative dispersion of pairs of particles, including the distance-neighbour function. In section 8 we report preliminary results on the Eulerian velocity tensor.

*The order of the two first authors (JM and SO) has been decided by tossing a coin.*

## 2 Apparatus and electronics

This section contains a description of the design of the tank experiment. A diagrammatic overview of the experiment is shown in figure 2. The tank and the grids generating the turbulence are discussed in section 2.1 and the preparation of neutrally buoyant particles in section 2.2. The stroboscope, shown in figure 9 together with its power supply, is triggered by the master video camera through a circuit taking out every second sync signal and a tunable delay. The other three cameras are slaves of the master providing perfect synchronization as described in section 2.3. The compression and storage of the video signals on two computers are presented in section 2.4.

### 2.1 Design of tank and turbulence generator

The ideal is to have a tank with a homogeneous, isotropic and (statistically) stationary turbulent flow with zero mean flow. This flow has been subject to numerous theoretical investigation, primarily because it is the most symmetric flow one can imagine and symmetry greatly reduces mathematical complexity. Therefore homogeneous isotropic turbulence is important as ‘the simplest case’ and

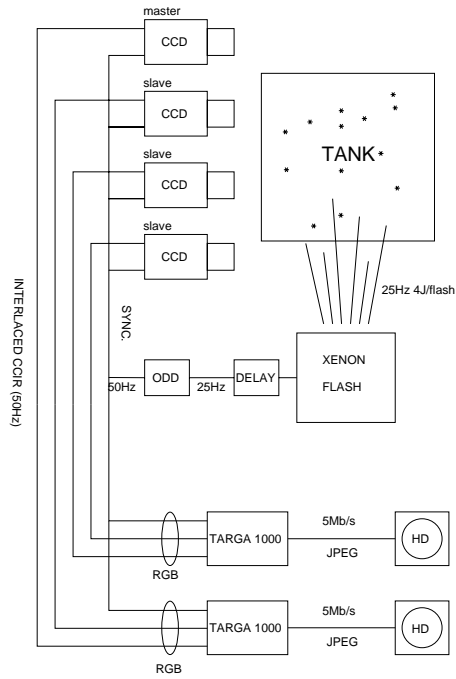


Figure 2. Diagram of the tank being illuminated by a Xenon flash light (stroboscopic). One of the four cameras is the master whose synchronization signal is used by the other cameras and the flash. Video signals are digitized and compressed by the pc-cards Targa 1000 Pro and stored on two hard disks.

the natural starting point for all turbulence theories. Besides, the general tendency towards isotropy within inertial range scales makes this flow an important case. By *Occams razor* we therefore prefer the simplest, yet non-trivial, case. However, the requirement of exact homogeneity and isotropy is a theoretical abstraction, which in practice can only be fulfilled to a certain degree of approximation (the presence of boundaries will, for example, always violate isotropy).

There are basically two ‘traditional’ methods for obtaining approximately homogeneous and isotropic turbulence. One consists in moving a grid through the fluid. Using a wide grid made from thin bars with a narrow spacing and moving it sufficiently rapidly the turbulence present after the passage of the grid will be approximately homogeneous. It will also be decaying, hence non-stationary. Isotropy is also violated by the choice a direction for the motion of the grid, but as the turbulence decays it becomes more isotropic. Alternatively one can set up a grid in a wind tunnel. This produces stationary turbulence, but isotropy is broken by the flow direction and homogeneity is broken by the decay of turbulence downstream of the grid. Again there is a strong tendency to restore isotropy away from the grid. The degree to which the turbulence is isotropic is, according to Monin and Yaglom (1975), “not quite clear”, since different result has been obtained in different wind tunnels, and there has been some controversy over calibration procedures (see Monin and Yaglom (1975) for references). Even if the two methods produce the same flow (in two different frames of reference) the experimental situation is different. Hot wires, which are frequently used in wind tunnels, need a large mean flow in order to work properly and hence they be cannot be used in a moving grid type of experiment. This is so because Taylor’s hypothesis must be valid, i.e eddies must pass the sensor fast enough that the turbulence can be regarded as frozen.

Unfortunately this prevents the study of non-frozen, Lagrangian properties. The need for Lagrangian statistics therefore favors the moving grid.

At an early stage it was clear that a water tank would be the best choice. The main reasons for choosing water rather than air were the lower kinetic viscosity of water and the fact that opaque and neutrally buoyant air borne particles (e.g. bubbles filled with smoke and Helium) are difficult to produce and control. Also we wanted to make use of the experience already existing at Risø with respect to particle tracking in two-dimensional water flows.

The next question was the generation of turbulence. The ‘towed grid’ method described above was one possibility, in many ways a simple and obvious choice, although the decay of the turbulence is a disadvantage, because ‘hand waving arguments’ must be applied in order to interpret results in terms of stationary turbulence. An alternative would be to consider an oscillating grid, which produces stationary (but inhomogeneous and somewhat anisotropic) turbulence. We had the impression that a single oscillating grid would produce no mean flow, but when we tried it, we learned that this is not the case. In fact, a mean flow develops streaming from the bulk towards the grid with return flow jets at the walls and in the corners, as reported in the literature (Fernando and Silva 1993, De Silva and Fernando 1994). According to Srdic, Fernando and Montenegro (1996) “the secondary [i.e. mean] flow remains the bane of all oscillating grid experiments”. All kinds of ‘motors’ were discussed until, thanks to Arkady Tsinober of Tel Aviv University, our attention was drawn to some recently made two-grid experiments. Measurements have shown that two oscillating grids placed at opposite ends of the tank produce almost no mean flow. Furthermore, according to Srdic et al. (1996) there is a region approximately 40% the width of the tank where the turbulence is nearly homogeneous and isotropic, and much more so than in wind tunnel grid turbulence. At least this is so as far as second order moments (the Reynolds’ stress tensor) are concerned. Higher order moments (in particular the kinetic energy flux) obviously must be non-isotropic. Even if the flow is not ideal it still seems to be the one that comes closest for the time being, and we decided to make a tank with two oscillating grids. We are aware of alternative methods, e.g. magneto-hydrodynamical forcing.

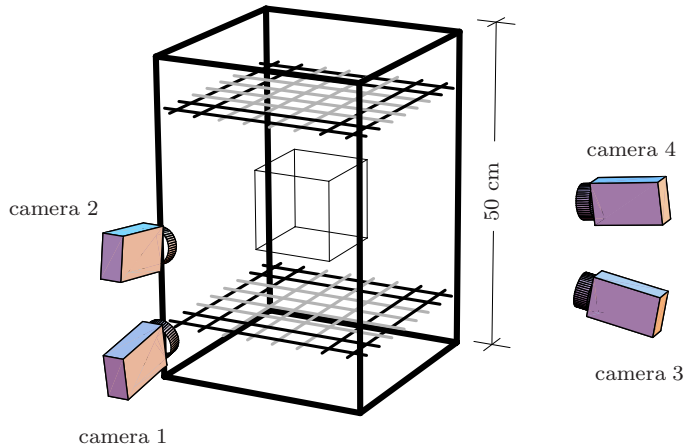


Figure 3. The basic system with the tank, the two grids and the four CCD cameras. The tank is  $32 \times 32 \times 45$  cm (inner dimensions) and the average distance between the grids is approximately 300 mm. The box inside the tank is the measuring volume.

In the beginning a fairly large tank containing about  $1 \text{ m}^3$  was planned, but, realizing the practical difficulties in handling a ton of clean water, we soon became

less ambitious and decided to build a smaller tank measuring 32cm × 32cm × 45cm. It was judged that an acceptable scale separation could still be obtained with the smaller tank, because the spatial resolution of the small scales was better than initially expected.

The tank design is depicted on figure 3. The tank is placed in a steel frame made from heavy steel profiles and bolted to the floor. The weight of the construction suppresses vibrations. Since vibrations were foreseen as a potential problem we chose a laboratory with a solid stone brick floor located in the basement in order to ‘stand on solid ground’. The bottom and two vertical sides of the tank have windows made from 10 mm glass. The four cameras look through the vertical windows while the bottom window is used for illumination. For this reason the grids need to be transparent. As a first attempt each grid was made from eight steel bars and eight Perspex bars. Unfortunately the steel was of poor quality and rusted and Perspex turned out to be too fragile for the purpose. New grids were made from Polycarbonate. This material is transparent like Perspex, but much stronger, and the grids could be cut out in a single piece from an 8 mm Polycarbonate plate using a programmable high precision milling machine. The mesh size is (grid constant)  $M = 40$  mm with 8 mm × 8 mm rods (see figure 4). The grid solidity is 0.36.

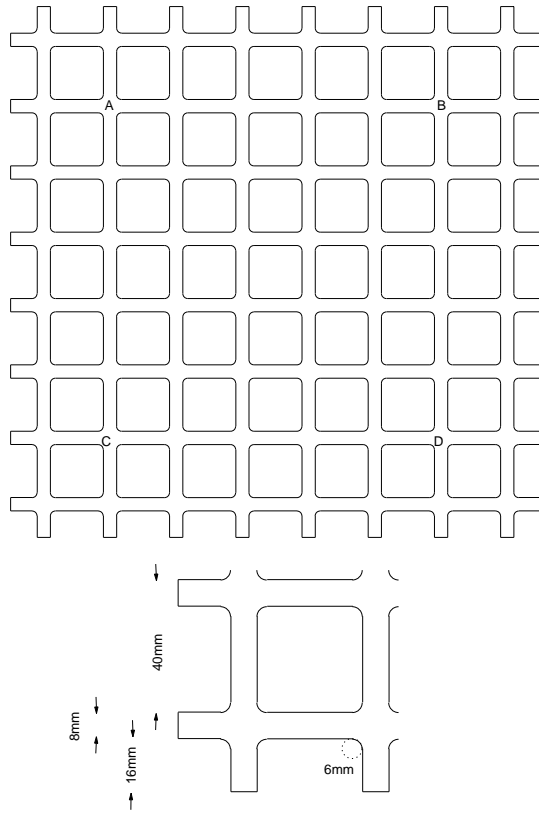


Figure 4. Grid geometry. The grids were cut from an 8 mm sheet of Polycarbonate using a tool of radius 3 mm, hence the corners of the square holes are slightly rounded. Steel rods are fixed to the grid at positions A, B, C and D.

The index of refraction of Polycarbonate (and Perspex) is 1.5 as opposed to 1.3 for water. Therefore the grids cast faint shadows. In order to blur these, and also to enhance illumination efficiency, we glued a mirror to the top plate of the tank.

Normally the tank is closed, but the lid can be removed to enable cleaning etc.

Particles can be injected with a syringe through a small hole in the lid.

Each grid is moved up and down by four 8mm rods that enter the tank through gaskets. We have had some problems making these completely airtight. Bubbles can be mistaken for particles, and since they are definitely not neutrally buoyant they can spoil the measurements. Simple torus shaped O-rings did not work but O-rings with ‘four finger’ cross sections were found to give sufficient sealing.

The transmission rods move in and out of the tank. We have the possibility to move the grids either in phase or completely in anti-phase. In the latter case the volume in the tank available for the water changes in time, and without pressure relief this would surely rupture the tank. Therefore the tank is equipped with eight pipes (‘chimneys’), one in each corners of the lid and one in each corner of the bottom. The four upper chimneys are just straight pipes with open ends. The lower ones make a U-turn and are connected to an air reservoir at the open end. The idea is to pressurize the air reservoir enough to make the water columns in the chimneys equally long. This ensures that the middle section of the tank does not oscillate due to pressure fluctuations caused by the rods going in and out of the tank. With this arrangement an open surface at the tank ceiling, where bubbles can be produced, is also avoided. However, pressure fluctuations are not eliminated in this way, and with the grids in anti-phase these are large enough to deform the windows. We therefore ended up operating the grids in phase for the last three runs, where no deformation of the windows can be observed. In this mode there is no volume change due to the motion of the rods, because some move in while others move out. However, there is a net displacement of the fluid, making it oscillate up and down. It should be noted that the amplitude of this oscillation is less than  $50\ \mu\text{m}$  in a typical experiment, and that the motion is correlated throughout the mid section of the tank, so it should not influence *relative* dispersion measurements and measurements involving velocity *differences*. Had we known in advance that the anti-phase arrangement causes these problems, we could have simplified the design considerably.

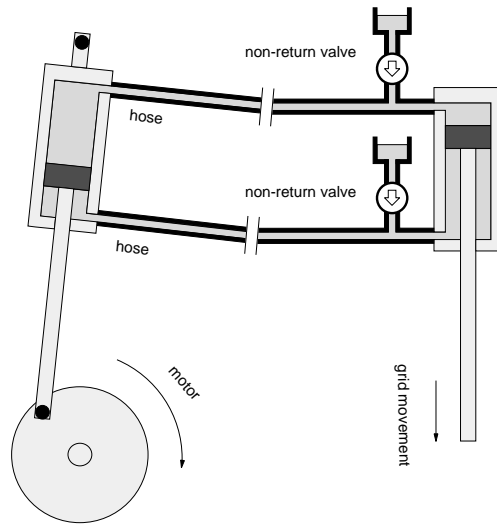


Figure 5. Hydraulic system used to move one of the grids. For the sake of simplicity valves that are normally closed are not shown.

The grid motion is produced by an electric motor fed by a frequency changer set and connected to a 14:1 gear. The rotation frequency of the gear shaft is read out to an electronic tachometer. Two hydraulic systems provide transmission from

the gear shaft to the grids. The idea is to shield the tank from the vibrations generated by the motor. Each hydraulic system consists of two double action cylinders connected by two hoses, see figure 5. The two hoses together with the two cylinders form two separate closed spaces filled with hydraulic oil. We had some troubles with cavitation in the hydraulic system<sup>1</sup>. This can happen in the branch which is ‘sucking’. We tried to avoid it by pressurising the system before start to 7 bars (available from compressed air), but it did not work. It turned out to be a better solution to install non-return valves connected to an oil reservoir at ambient pressure. In this way the system pressurizes itself whenever the pressure drops below ambient pressure in one of the branches. Due to the compressibility of the oil the stroke (i.e. the peak-to-peak movement of the grid) is slightly reduced. The stroke is easily measured with a pen fixed to one of the rods.

A circulation pump and a filter (20 $\mu$ m pores) is used to keep the water clean.

## 2.2 The particles

Several types of particles have been tried. Ideally particles should

- be spherical with a definite diameter
- have the same density as water
- be opaque and reflect light evenly

In reality the diameter and the density will have a certain tolerance, and the intensity of scattered light will depend on the angle of deflection. The best particles we have tried are Styrocell particles made by Shell Chemicals. They are made from Polystyrene containing a small amount of Propylene, which can evaporate and make them pop like popcorn when they are heated. In the industry Styrocell particles are used for manufacturing e.g. coffee cups. Looked at in a microscope they appear perfectly spherical<sup>2</sup> and they also reflect light reasonable well. The density is 1.02 g/cm<sup>3</sup>, which is slightly too high. We have found that the density can be changed if the particles are boiled for a few seconds. Most particles pop immediately, but a small fraction becomes neutrally buoyant. After boiling the particles are dropped in cold water and set aside for about half an hour. Thereafter the particles still suspended in the water can be extracted with a syringe. The termination velocity of these particles is just a few centimeters per hour. The density changes slightly over a couple of days, so fresh particles have to be produced for every experimental day. The treatment also makes the particles appear more milky white. They are still opaque, since they have no dark side. The particles are sorted at the factory and various particle sizes are available. We use a sorting machine (essentially a vibrating stack of sieves) to narrow the tolerance. Clearly the particles should be as small as possible, preferably much smaller than the Kolmogorov length scale. However, smaller particles reflect less light, require cleaner water, stronger light source and better contrast. Our favorite particles have diameters in the range 500–600  $\mu$ m. They are large enough to cover a few pixels which is essential for a good position determination.

It would be nice if we could use smaller particles. However, using smaller particles that only cover one pixel would deteriorate the position determination. A point-like particle would only produce counts in *one* pixel, leaving no possibility to say anything about where within the pixel the particle is located. We have considered several ways of blurring a point-like image. The ideal solution would be

---

<sup>1</sup>Cavitation happens when the pressure drops below the vapour pressure of the oil, and it can produce a so-called liquid hammer. In the first version of the hydraulic system the balls of the ball valves were simply knocked out of their housings by a liquid hammer.

<sup>2</sup>Placed between two plated they roll easily like balls in a ball bearing. If they are spilled the floor becomes dangerous to walk on.

to make the camera lens diameter small enough that diffraction smears the image over several pixels. Simple calculations show that for our experimental setup the required relative aperture (ratio of focal length to diaphragm diameter) is  $f/D \approx 22$ . We do not have sufficient light for such a large aperture.

We note that in direct measurements of the velocity gradients, using two hot-wires, it is common to accept separations of several Kolmogorov lengths  $\eta \equiv (\nu^3/\varepsilon)^{1/4}$ . In other words, practical experience shows that the velocity field can be considered linear over distances somewhat larger than  $\eta$ . As we show later (see section 5) 500–600  $\mu\text{m}$  corresponds to 2 or 3  $\eta$  and the particles therefore most probably small enough to be considered as ideal fluid points.

## 2.3 Cameras and light

The CCD<sup>3</sup> cameras are industrial standard monochrome cameras equipped with simple inexpensive 25 mm lenses. We used the CV-M50 model from JAI<sup>4</sup>. It is built around a 1/3" Sony CCD chip with a resolution of 720×576 square pixel elements. Each pixel element is equipped with a microscopic lens so that the ‘dead area’ of the chip is minimal.

The camera speed is 50 *frames* (half pictures) per second or 25 *fields* (full pictures). All affordable frame grabbers work with interlaced images, so this technique had to be used in order to keep the costs at a reasonable level. The fact that the two frames of a picture are not exposed at the same time is a problem, since the vertical resolution of a single frame is poor. Some cameras, such as the CV-M50, can run with the electronic shutter almost completely off so that each frame is exposed all the time except for a short period when the frame is read out and reset. This means that the exposure periods of the two frames overlap for about 20 ms. With proper timing the flash can therefore be fired while both frames are open for exposure.

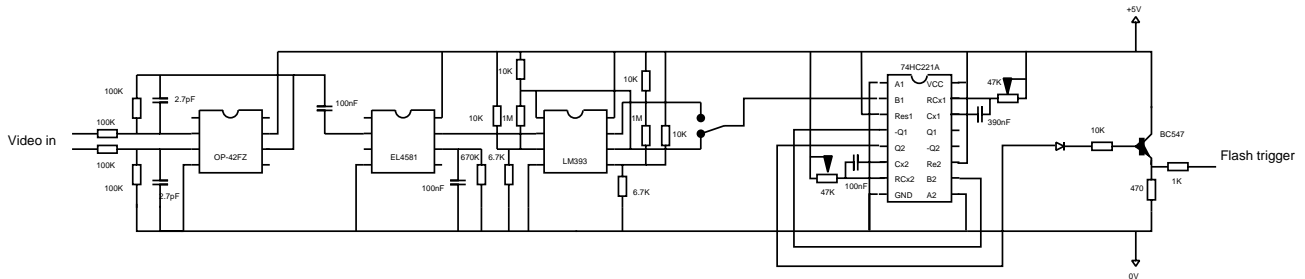


Figure 6. Synchronous trigger pulse generator. There are five stages (left to right): a differential amplifier, a sync separator producing ODD/EVEN indication, a Schmidt trigger, two mono-stable multi-vibrators (on a single chip) for delay and pulse width shaping and finally an output transistor.

One of the cameras (camera 1) is the master, delivering synchronization signals to the three other cameras, the Xenon flash and the frame grabber cards (see figure 2). Both vertical (VD) and horizontal (HD) synchronization signals are fed from camera to camera via two standard 75  $\Omega$  co-axial cables terminated with

<sup>3</sup>CCD stands for Charge Coupled Device. CCD electronics trap electric charges generated in a light sensitive pixel element in potential pockets. The trapped charges are moved by moving the pockets.

<sup>4</sup>Details can be found on JAI’s homepage <http://www.jai.dk/>

a 75  $\Omega$  resistor at camera 4 (this cabling gives the least jitter). The cameras run in normal interlaced mode, meaning that they output *frames* (half-pictures) consisting of lines with odd or even line numbers. Composite video signal from camera 1 (the master) is fed to a sync separator, which can output a TTL signal (ODD/EVEN output) indicating which of the two frames is active. This signal is delayed and used as external trigger for the flash. In this way the flash is fired at the right moment. Details of the trigger pulse generator are shown in figure 6.

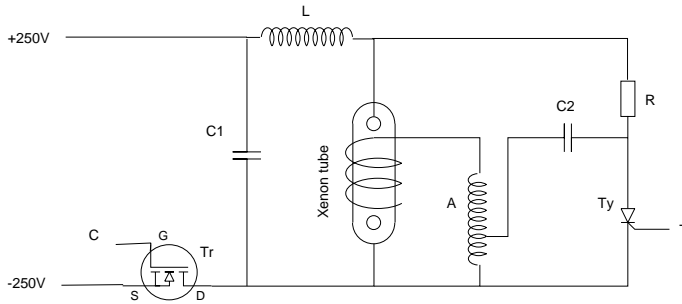


Figure 7. Simplified stroboscope diagram.

The Xenon flash was constructed by us, since powerful Xenon flashes with a continuous repetition rate of 25 Hz are not commonly used. Conventional stroboscopes (used e.g. as tachometers in the workshop) have fast repetition rates but they are by far not powerful enough. More powerful stroboscopes, used e.g. in medico-technique, are available, but they are very expensive and deliver only 2 Joules per shot where we aimed at 4 Joules per shot. We have found that the price level of *disco strobes* is much more reasonable. They are not designed for 25 Hz and the triggering is unreliable, but they have sufficient power and the discharge tube, the reflector and the cabinet are fine. We used these components, made new circuitry, and installed forced air cooling in order to be able to raise the flash rate to 25 Hz. The stroboscope and the power supply are shown in figure 9.

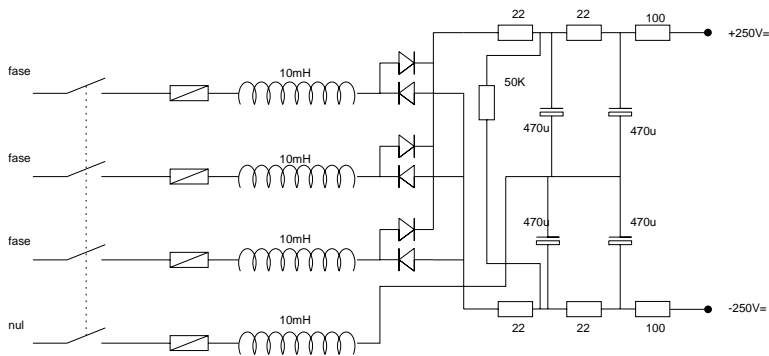


Figure 8. Simple 500V DC power supply.

The flash light is powered by a 500 V DC power supply shown on figure 8. It is a simple construction that does not produce electro-magnetic noise.

Flashes are produced by discharging a capacitor through a Xenon tube. The basic circuit is shown on figure 7. It is based on ideas from AG&G (1995), Giesberts



*Figure 9. The rebuilt disco strobe together with its 500 V DC power supply.*

(1994) and Koecher (1976). The input C activates charging of capacitor  $C_1$  through transistor Tr (a power CMOS). Input T (the gate of the thyristor Ty) triggers the tube by discharging  $C_2$  through the trigger coil A producing a 5 kV pulse at the secondary winding of the coil. A thin wire wound around the tube transmits the high voltage pulse to the tube and initiates the discharge of capacitor  $C_1$  through the tube via a discharge coil L. The purpose of coil L is to shape the discharge pulse and limit the peak current in order to red shift the light output and also to increase the life time of the tube. Choosing the right value of the inductance in combination with  $C_1$  and flash tube characteristics the pulse can be shaped to single 50  $\mu$ s peak with no transient ‘ringing’ (see AG&G (1995) and Koecher (1976) for details).

It is important that the tube is not triggered while Tr is on and  $C_1$  is being charged, since this would discharge the large power supply capacitors and destroy the discharge tube. Both inputs (C and T) are at a high and varying DC levels, and opto-couplers are used to provide galvanically insulated inputs (see figure 10 for details). The control signals to C and T are produced by the flash control circuitry shown on figure 11. It basically consists of four non-retriggerable monostable multivibrators ( $V_1$ ,  $V_2$ ,  $V_3$  and  $V_4$ ) with an opto-coupler at the external trigger input (for safety).  $V_1$  and the opto-coupler serve as an input filter rejecting the external trigger shorter than 1 ms and inhibiting triggering while  $C_1$  is being charged. At the moment an external trigger pulse is accepted  $C_1$  is therefore already charged. As the  $V_1$  output rises it triggers  $V_3$  and  $V_2$  with a small delay.  $V_3$  goes high for 15 ms and this signals inhibits charging. Shortly after  $V_2$  goes high for 100  $\mu$ s and the signal is transmitted to input T of the flash circuit. At the negative going edge of the  $V_3$ , output  $V_4$  is triggered and goes high for 15 ms activating charging of  $C_1$  and disabling the external trigger. The control circuit is ready for the next trigger at the negative going edge of  $V_4$ .

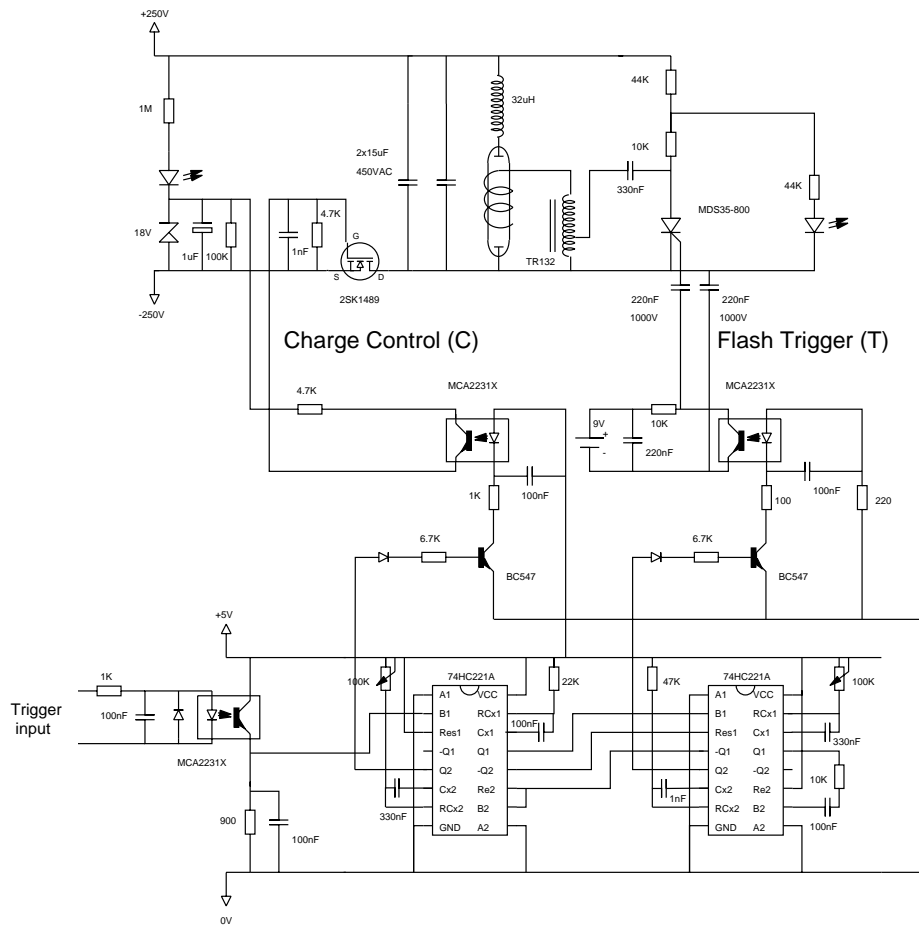


Figure 10. Strobe diagram.

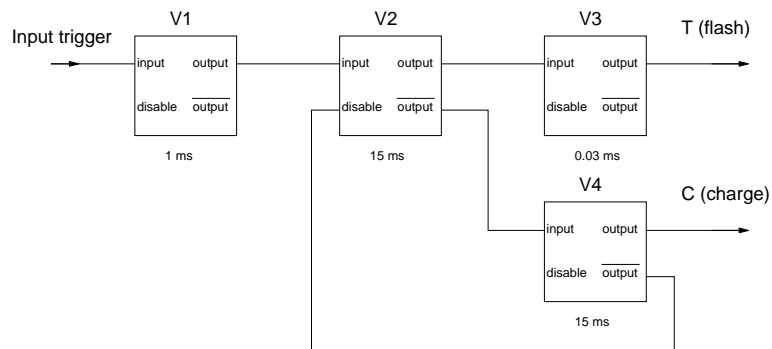


Figure 11. Simplified trigger sequence generator circuit using four monostable multivibrators.

## 2.4 Recording system

It was a design criterion that the system should be able to digitize and record continuously. Most systems use random access memory to store digitized images, but this severely limits the length of sequences. Until recently on-line storage to hard disk of the digital output from a frame grabber has not been possible with commercial off-the-shelf equipment. The finite rate of rotation of the hard disk has been the bottle-neck, and it still is, even if the speed of new models continue to improve. At present (as of early 1997 when the hardware was purchased) it is relatively easy to store 5 Mb/s continuously, which should be compared to the 10 Mb/s output of a single digitized monochrome video channel. In order to store the 40 Mb/s stream from four cameras we use two frame grabber cards with hardwired JPEG compression and two computers. Each card is connected to two cameras via the red and blue channels of the RGB input, while the green channel is used for the sync. The cameras are synchronized so they can be treated as if they were separate colors in a color video signal<sup>5</sup>. The Targa 1000 Pro card is able to do this. Since the images consist of small bright dots on a dark background a considerable degree of compression should be possible, and it is our experience that the loss of quality due to the (in fact rather modest) 1:4 JPEG compression is insignificant. The two computers, each with its own Targa 1000 Pro card and a fast AV disk, form a local network with synchronized system clocks and each runs a digital VCR. The synchronization allows the two digital VCRs to be started at the same vertical sync pulse. The digital VCRs (see figures 12 and 13) were developed in visual C++ on the basis of source code that comes with the cards.

## 3 From video data to particle tracks

There is a long way from the raw video sequences to the three-dimensional particle tracks. The procedure can be divided in four steps:

1. Determine particle positions on CCD images
2. Convert these to lines in the measuring volume via calibration
3. Combine lines from the four cameras to 3D positions
4. Track 3D positions in time

These steps will be discussed in the following subsections, but first a few words on the software we are using to obtain the video movies.

The software ‘tape recorder’ which was included in the purchase of the Targa compression card was modified in order to make the two data acquisition computers start recording at the same instant.

The original user interface is shown in figure 12 with buttons for recording, stopping, pausing, one frame back, play, and one frame forward. Concurrently the video images are shown either on an area of the computer screen or on an auxiliary monitor. Under the buttons is a window and a slide bar for fast positioning in the video sequence. In the next panel in figure 12 the length of the video sequence can be typed in together with the Q-factor, which is a parameter determining the compression rate in the JPEG compression. The Q-factor can also be determined ‘dynamically’ in which case the data rate has to be set. With this configuration the Q-factor is adjusted continuously as the video is recorded and compressed in order to maintain the given data rate. For our computers approximately 5 Mb/s

---

<sup>5</sup>Actually we ended up using YUV with sync on Y channel and the two cameras on U and V. YUV is like RGB except that Y, U and V are certain linear combinations of R, G and B.

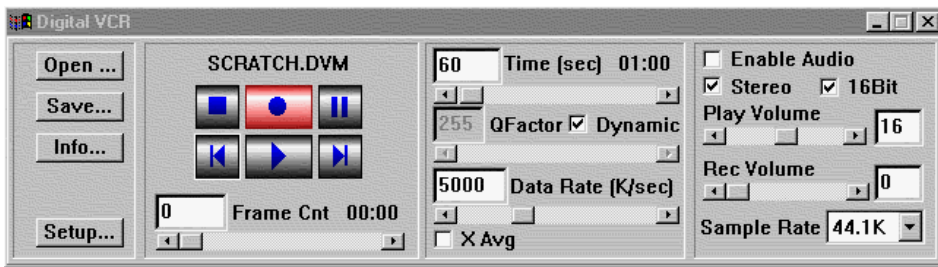


Figure 12. User interface of the Targa digital tape recorder (VCR).

is the highest continuous rate. In the last panel parameters regarding sound are adjusted. These are of course irrelevant for this project.

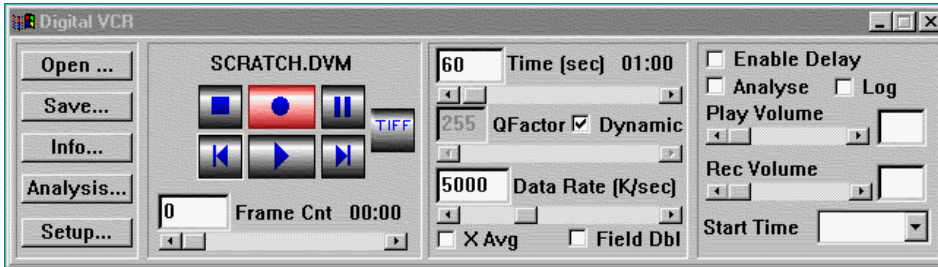


Figure 13. User interface of the modified Targa tape recorder.

The tape recorder provided by True Vision is well suited for visual inspection of the recorded sequences. However, there are several deficiencies which must be amended for our particular purpose.

Firstly, the button ‘TIFF’ has been added, see figure 13. Pushing this button saves the current image as a TIFF file, which later can be studied in detail in an image manipulation program. The program xv has been very useful in this respect and it can be down-loaded from the Internet, free of charge (see <http://www.trilon.com/xv>). When the recorder is not playing back, the current image will not undergo compression during saving. In this way the effect of compression on the image quality can be studied.

Secondly, the button ‘Analysis...’ hides a hierarchy of menus for the adjustment of parameters relating to the determination of particle image positions on the CCD images, as described in section 3.1. In order to analyse a previously recorded sequence the ‘Analysis’ box has to be checked before the play button is pushed. If the ‘Log’ box is checked a log file containing information on problems during the analysis is created.

Lastly, the check box ‘Enable Delay’ enables the recorder to start at a pre-determined time set in the ‘Start Time’ box. Proper synchronization of the two computers ensures that the recordings of the four cameras start simultaneously.

Each black and white camera produces 576 times 720 pixel of one byte 25 times per second, yielding a the data flow rate of approximately 10 Mb/s per camera. Since the signal from two cameras are combined into one Targa compression card with a typical output rate to the hard disk of 5 Mb/s, the signals are compressed down to 25%. The data rate per minute is approximately 300 Mb.

The recorder is coded in C++ and we have used, as recommended by TrueVision, Microsoft Visual C++ 5.0 with its ‘Developer Studio’ for the modification.

This integrated programming and debugging environment is very nice to work with. However, the compiler itself, when the executable is optimized for speed, has many severe errors.

### 3.1 Determination of positions on images

The basic and most important observation is that images of particles of the size of a few pixels in each direction can give rise to a much better position determination than images occupying only one pixel. This fact is well known by astronomers, who use de-focused CCD images for accurate determination of the position of stars.

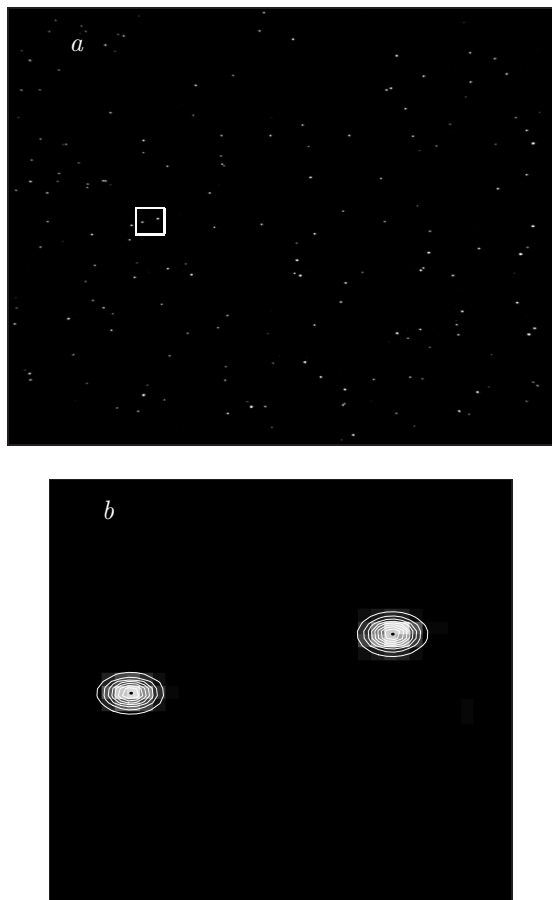


Figure 14. Low particle density CCD image; a:  $720 \times 576$  pixels, b: close-up of the small white rectangle on a.

A typical low particle density CCD image is shown in figure 14 and a high density image is shown in figure 15.

A straight forward way of determining the particle position is to calculate the barycenter of the pixel intensities in a small image area engulfing the particle. If  $I(x, y)$  denotes the pixel intensity with the background subtracted and  $x$  and  $y$  are the integer pixel coordinates, then the center could be estimated as

$$\begin{aligned} x_c &= \frac{\sum_{x,y} xI(x,y)}{\sum_{x,y} I(x,y)} \\ y_c &= \frac{\sum_{x,y} yI(x,y)}{\sum_{x,y} I(x,y)}, \end{aligned} \tag{1}$$

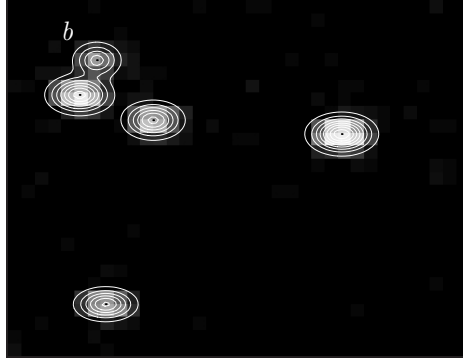
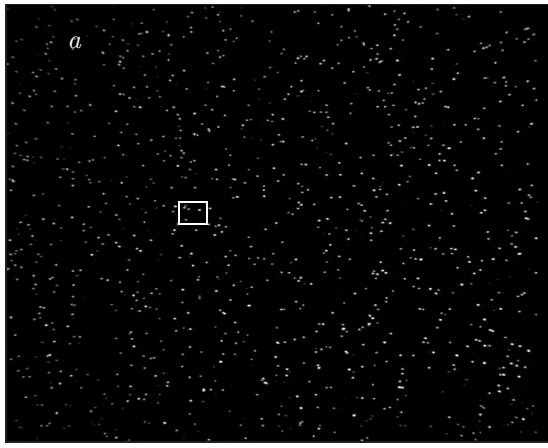


Figure 15. High particle density CCD image; *a*:  $720 \times 576$  pixels, *b*: close-up of *a*.

where the summation is over all pixels in the small area surrounding the particle. However, as seen in the top left corner of figure 15*b*, the particles often overlap, and it is impossible to use the simple bary-center technique.

Instead, each particle is fitted with a Gaussian shape function:

$$I_p(x, y) = \frac{M}{2\pi\sigma_x\sigma_y} \exp \left[ -\frac{1}{2} \left\{ \left( \frac{x - x_c}{\sigma_x} \right)^2 + \left( \frac{y - y_c}{\sigma_y} \right)^2 \right\} \right], \quad (2)$$

where  $M$  is the total intensity of the particle,  $(x_c, y_c)$  its position, and  $\sigma_x$  and  $\sigma_y$  its width in the  $x$  and  $y$  directions. In this expression, the  $\sigma$ 's are generally different. This is caused by the way the CCD chip works: The accumulated electrons in each pixel are read out in rows in the  $x$ -direction, and in this process there might be some 'spill over' or smearing from pixel to pixel. Also the electronics may smear out the signal in the  $x$ -direction. Therefore,  $\sigma_x$  will typically be larger than  $\sigma_y$ .

The entire algorithm for finding particle position on the images may be summarized as follows:

1. The image is scanned until a local maximum larger than ParticleThreshold (see table 1) is found.
2. An area which engulfs the local maximum, such that every intensity on its border is less than some level is located. The intensity in this area may have more than one local maximum and it is assumed that the number of local maxima is equal to the number of particles  $n$  in that area.
3. A sum of  $n$  Gaussian functions as given by (2) are fitted to the pixel intensities giving  $n$  times 5 parameters. The efficient Levenberg-Marquard algorithm (Press, Flannery, Teukolsky and Vetterling 1992) is used for the fitting. At

Table 1. Input parameters for the determination of the particle positions on the CCD images

Parameter	Description
BackgroundLevel	This value is subtracted from all pixel values (ranging from 0 to 255). If the pixel value becomes negative it is truncated to 0.
IsolationLevel	The area around a local maximum is enlarged until every pixel on its boarder is less than IsolationLevel (over the background).
ParticleThreshold	If the local maximum is less than ParticleThreshold then it is skipped.
{XLow, XHigh, YLow, YHigh}	Limits of the rectangle on the CCD image used to locate particles. The largest size of the rectangle is {0,719,0,575}. Sometimes it is limited further, f.ex. if the oscillating grids are entering the field of view of the cameras.

Table 2. Output parameters given for each particle. All parameters are obtained from fits with a sum of  $n$  copies of (2).

Parameter	Description
$M$	The integrated intensity of the particle.
$x_c$	The $x$ coordinate of the particle center.
$y_c$	The $y$ coordinate of the particle center.
$\sigma_x$	The half-width in the $x$ -direction.
$\sigma_y$	The half-width in the $y$ -direction.
$n$	The number of particles entering in the fit. This parameter is usually one, but f.ex. for the three particle in the upper left corner of figure 15b it is 3.

rare occasions it fails (say, one out of  $10^6$ ), and the much less efficient but more robust downhill simplex method is used.

4. The area under investigation is zeroed, the parameters are saved and the algorithm returns to 1.

This loop stops when all local maxima have been investigated. Bearing in mind that a typical experimental run of one minute records of the order of 6 million particles through the four cameras, it is obvious that the algorithm above has to be carefully optimized for both robustness and speed.

Figure 16 show the distribution of the total particle intensity  $M$ , calculated from the four first seconds of run 22 (see table 5). The widths of the distributions are much larger than the variation in particle sizes suggests. The average intensity seen from camera 1 and 3 is significantly larger than from camera 2 and 4. This is probably because the light source is below the box (see figures 2 and 3) and the partially opaque particles are therefore brightest on their lower hemisphere. Camera 1 and 3 see more of the bright side of the particles.

In order of importance the reasons for the broadening of the distributions are:

- Inhomogeneous lighting. Particles may be in the transition between light and shadow or in the faint shadows of the polycarbonate grids. The light is also diverging.
- Variation in viewing angle.
- Variations in particle properties.

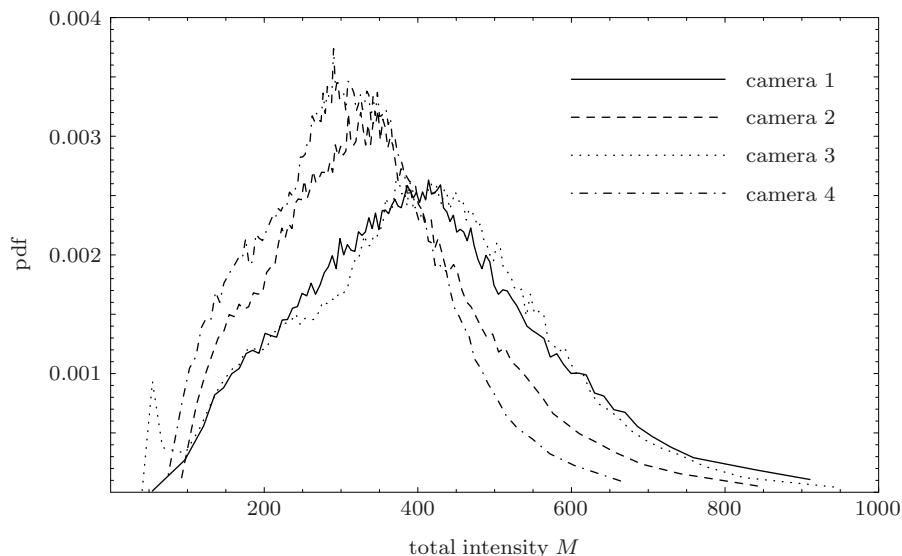


Figure 16. Probability density of the total intensity  $M$  defined by (2).

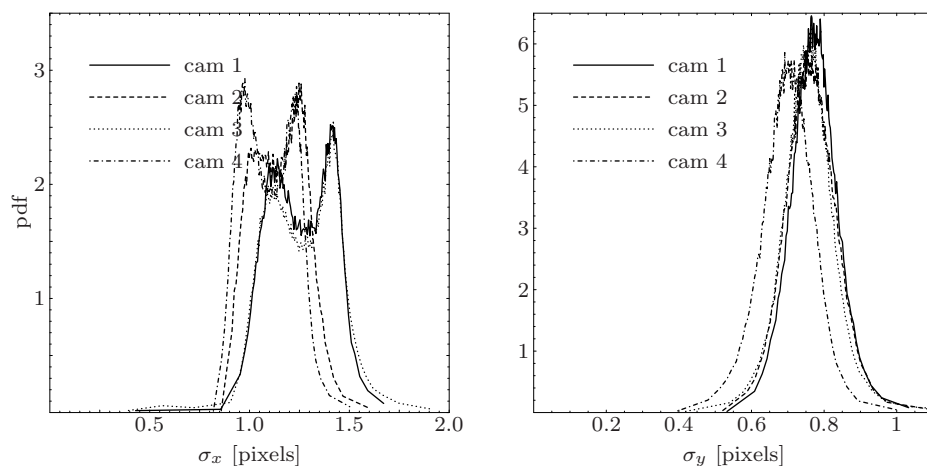


Figure 17. Probability density of the widths of the particle images  $\sigma_x$  and  $\sigma_y$ .

Probability distributions for the parameters  $\sigma_x$  and  $\sigma_y$  are shown in figure 17. The  $\sigma_x$  distribution has a strange bimodal shape, while  $\sigma_y$  has a nice, narrow distribution. The reason for the bimodal shape is still unclear, but observations of individual particle images reveal a low-intensity tail with a weak ghost image a few pixels to the left (in the positive  $x$  direction). Whether this ghost image is inside or outside the area used for fitting may influence the determination of  $\sigma_x$ . This adds to the uncertainty of the determination of  $x_c$ . The discussion below may also shed light on the strange behavior of  $\sigma_x$ .

### Estimation of the position error on the CCD chip

One can crudely estimate the uncertainty of the position determination by looking at the small, apparently random, fluctuations around a particle track which is known to be smooth. To do so we stopped the oscillating grids and waited for a while in order to produce very slow decaying motions of the fluid which presumably are smooth. In this way we also avoided any extra uncertainty due to floor vibrations caused by the motor driving the hydraulics. In other words we isolate

the error solely due to the recording and analysing system (cameras, digitization and compression cards, fitting routines, ...).

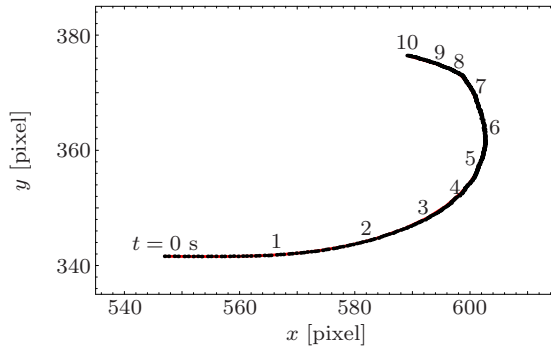


Figure 18. A calm 10 seconds long particle track from run 11.

An example of a track recorded under these conditions is shown in figure 18. From this track we subtract a smooth cubic spline anchored once every second (at every 25th position). The resulting residuals, shown in figure 19, show much larger errors in  $x$  than in  $y$ . We estimate the random errors to be

$$\sigma(x_c) < 0.1\text{pixels} \quad \sigma(y_c) < 0.02\text{pixels}. \quad (3)$$

The slow variation in the  $y$  residue after  $t = 6$  s are not due to random errors, but merely the inability of the cubic spline to fit the particle track.

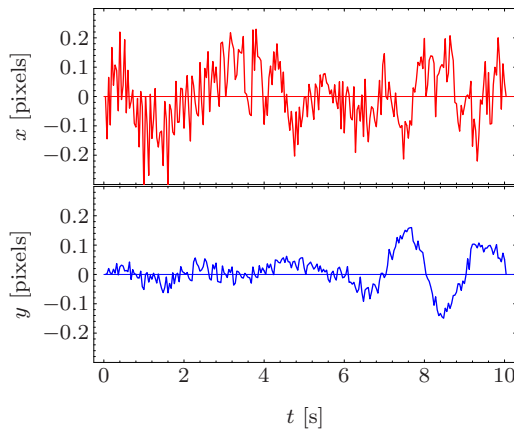


Figure 19. The  $x$ - and  $y$ -positions of the track shown in figure 18 with a smooth spline subtracted. The uncorrelated residuals are random measurement errors.

The main cause of the larger uncertainty in the  $x$ -direction is probably line jitter, i.e. small random time delays in the video signal corresponding to of the order of 0.1 pixel. There is no jitter problem for the  $y$  direction.

It should be stressed that this is not a very systematic way of investigating the error, and it is not applicable to the case with strong turbulence where the grids are oscillating because it is difficult to distinguish the fastest turbulent movements from random errors. In section 3.5 we estimate the random errors of the position determination in three dimensional space both in a quiescent and a turbulent flow using properties of the Lagrangian auto-correlation function.

### Position errors due to finite pixel size and to jitter

There is a small systematic error associated with the discretization of the continuous distribution of light (the image of the particle) into the square pixels of the

CCD chip. We have done quite a lot of work on this correction, but it seems to be swamped by the line jitter.

A future way of getting rid of jitter, which manifests itself in the upper plot of figure 19 and in the  $z$ -plot of figure 27b, would be to record a physical edge at constant  $x$ . If the position of this edge could be determined with less than 0.1 of a pixel we might be able to subtract the jitter. Another more viable way would be to use better hardware which synchronizes the analog to digital conversion in the frame grabber better. Perhaps digital cameras could do a better job?

The manufacturer of the cameras JAI states that the line jitter is approximately  $\pm\frac{1}{3}$  to  $\frac{1}{4}$  pixels. The jitter shown in figure 19 (top) is definitely smaller than this, probably because the determination of the  $x$ -position of the particle is an average over a few lines in the  $y$  direction.

## 3.2 Calibration and recalibration

As in Dracos (1996) the first step in the calibration is to take pictures of an object with known geometry. For that we have constructed a Perspex cube with an inner dimension of 130 mm. The cube has two “fronts”, one facing camera 1 and 2, the other facing camera 3 and 4. In each of the fronts there are a regular quadratic array of 6 by 6 holes separated with 17.5 mm drilled into the Perspex and filled with stearin. In the corresponding “backs” there are patterns of 7 by 7 points separated by 20 mm as shown in figure 20.

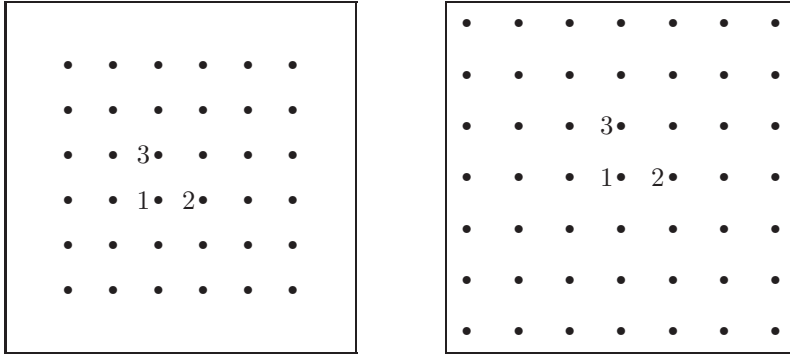


Figure 20. Front and back of the calibration box. For each camera the pixel coordinates of the three points indicated on each face has to be estimated.

The calibration box as seen from camera 2 is shown in figure 21. The overlapping quadratic patterns of bright spots from the front and the back of the box are clearly seen. Also the rows of white dots can be seen on the right and left side of the box, which are the front and the back as seen from camera 3 and 4. Particles both underneath and on top of the bottom and top plates are also seen.

A computer code has been made which uses as input the approximate pixel positions of the three numbered points on the front and back faces in figure 20. It also needs the parameters given in table 1. The code then finds as many of the calibration points as possible by fitting to (2). These pixel positions together with the known positions on the front or the back face makes it possible through a least squares fit to determine coefficients  $f_{ij}^k$  in a series expansion around the center of the CCD chip  $(x_p, y_p) = (360, 288)$  of the position on the face. For a given camera and a given face we can write this Taylor series as

$$F_k(x_p, y_p) = \sum_{i=0}^{n_{pf}} \sum_{j=0}^{n_{pf}-i} f_{ij}^k (x_p - 360)^i (y_p - 288)^j, \quad (4)$$

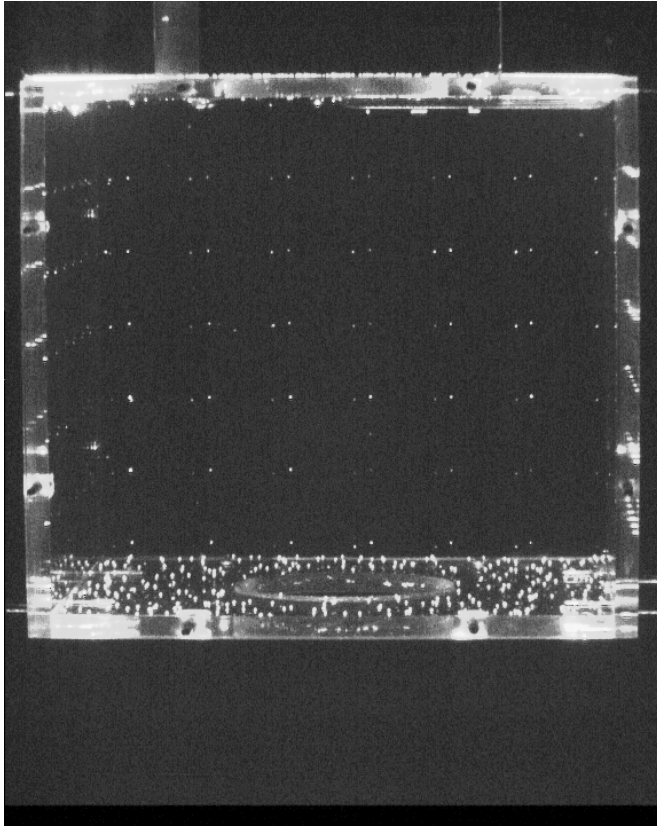


Figure 21. The Perspex calibration box as seen from camera 2.

Table 3. An example of the 40 calibration coefficients for camera 1. All the coefficients have the unit mm.

		$i$				
		$j$	0	1	2	3
FRONT	$f_{ij}^1$	0	0.486	-0.00262	$1.15 \times 10^{-6}$	$-2.33 \times 10^{-8}$
		1	-0.252	$9.48 \times 10^{-6}$	$4.44 \times 10^{-10}$	
		2	$-2.76 \times 10^{-6}$	$1.56 \times 10^{-8}$		
		3	$-1.56 \times 10^{-8}$			
	$f_{ij}^2$	0	-16.6	-0.277	$1.30 \times 10^{-5}$	$-3.60 \times 10^{-8}$
		1	0.00449	$-4.04 \times 10^{-6}$	$-9.80 \times 10^{-10}$	
2		$1.37 \times 10^{-6}$	$1.05 \times 10^{-11}$			
BACK	$f_{ij}^1$	0	-4.95	-0.00425	$-6.02 \times 10^{-7}$	$8.12 \times 10^{-9}$
		1	-0.284	$1.28 \times 10^{-5}$	$-3.66 \times 10^{-8}$	
		2	$-4.45 \times 10^{-6}$	$-4.70 \times 10^{-9}$		
		3	$-1.68 \times 10^{-8}$			
	$f_{ij}^2$	0	-3.15	-0.315	$1.07 \times 10^{-5}$	$1.40 \times 10^{-8}$
		1	0.00546	$-6.63 \times 10^{-6}$	$-1.49 \times 10^{-8}$	
2		$-1.69 \times 10^{-6}$	$-1.70 \times 10^{-8}$			
		3	$-7.71 \times 10^{-9}$			

where  $F_1(x_p, y_p)$  gives the  $x$  position on the face for a given pixel position,  $F_2$  gives the  $y$  position, and  $n_{\text{pf}}$  is the order of the polynomial. An ideal pinhole camera without the intervening air-glass-water interface would have  $f_{ij}^k = 0$  for  $i + j > 1$ . Lens aberration, the interface, and CCD chip imperfections make these coefficients non-zero. The number of coefficients in (4) for a single  $k$  is  $(n_{\text{pf}} + 1)(n_{\text{pf}} + 2)/2$ . There are four cameras, two faces (front or back) and two values of  $k$  used in the calibration, so a calibration has in total  $8(n_{\text{pf}} + 1)(n_{\text{pf}} + 2)$  coefficients. We use  $n_{\text{pf}} = 3$  so the number of coefficient to be extracted from four images like figure 21 is 160. Fourty of these (from camera 2) are displayed in table 3. Several things may be seen from this table:

- The size of a pixel projected to the front is roughly 0.25 mm and to the back closer to 0.3 mm.
- The size of the nonlinear terms may be estimated by inserting  $(x_p, y_p) = (360 + 250, 288)$ , which is close to the edge of the calibration box, into (4). For the back, looking at  $k = 2$ , the zeroth order term is  $-3.15$  mm, the first  $-0.315 \times 250 = -78.75$  mm, the second 0.67 mm, and the third 0.22 mm. The non-ideal terms, i.e. the second and third order terms, are small but certainly not negligible. Closer to the center of the field these term become smaller.

For later computational convenience (see section 3.3) the program also calculates an approximate function which gives the intersection of a line of sight (for a given camera) which goes through a point in space  $(x, y, z)$  and the back face. Given the calibration (4) this intersection can be calculated by iteration. However, it is more convenient to have it on the Taylor expansion form

$$G_k(x, y, z) = \sum_{i=0}^{n_{\text{sf}}} \sum_{j=0}^{n_{\text{sf}}-i} \sum_{l=0}^{n_{\text{sf}}-i-j} g_{ijl}^k x^i y^j z^l \quad (5)$$

where  $n_{\text{sf}} = 3$  in our experience is sufficient. Similar approximate function are calculated for the intersection between the line of sight and an imaginary middle face between the front and the back.

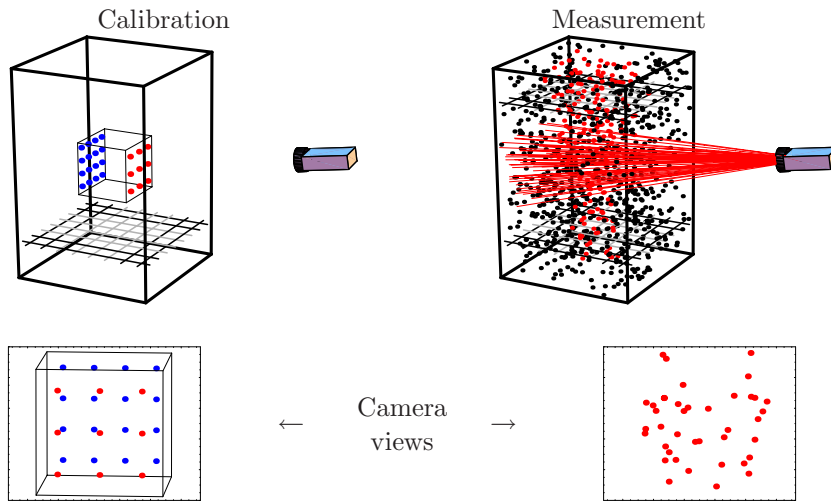


Figure 22. Sketch of the calibration procedure.

The calibration procedure may be summarized as follows (see figure 22). First the calibration box is lowered into the water of the tank. Then images are taken with all cameras. For a given camera analysis of the image gives a relation between positions on the video image and on the front and the back of the box, i.e. a relation

between points on the video images and lines in the measuring volume. Then the box is removed, the upper grid is reinstalled and particles are added to the water. Through (4) particle positions, as determined on the images, are translated into lines in space.

## Recalibration

Working with the equipment, adjusting the grids, mounting and unmounting the lid and various thermal expansion may change slightly the relative positions and angles of the cameras with respect to the tank. This may deteriorate the calibration and we have found it necessary to do a software recalibration. This is done by tracking up to one thousand particles evenly distributed over the measuring volume (see sections 3.3 and 3.4). We select the uninterrupted tracks, which we have the most confidence in, and select one point from each of these tracks. Each of these  $N$  points has an associated measure  $S$  of the mismatch of the lines that ‘hit’ the particle (see (6)). The recalibration or the improvement of the calibration is then done by tuning (most of the) 160 coefficients  $f_{ij}^k$  in (4) to minimize  $\sum_{i=1}^N S_i$ . This is a complicated minimization problem for which we use the downhill simplex method (Press et al. 1992).

The whole cycle of recalibration, 3D reconstruction and tracking is repeated a few times, and each time more and more particles get tracked in a larger and larger volume.

## 3.3 Reconstruction of 3D positions

In a typical run the four cameras see approximately 1000 particles each. How can we determine which combinations of lines of sight make particles? The simple answer is that we just have to look at lines crossing each other. However, the lines do never cross exactly due to the imperfect calibration and the random error in the position determination on the CCD chip. We therefore define the particle position  $\mathbf{p}$  for a given number of lines  $l_1, l_2, \dots, l_n$  as the minimum of the sum of the squared distances

$$S = \sum_{i=1}^n \text{dist}(\mathbf{p}, l_i)^2, \quad (6)$$

where  $\text{dist}(\mathbf{p}, l_i)$  denotes the shortest distance between  $\mathbf{p}$  and  $l_i$ , see figure 23. Had the lines crossed this sum would be zero. To find  $\mathbf{p}$  we introduce a parametric form for  $l_i$ :  $t \rightarrow \mathbf{a} + \mathbf{b}t$ , with  $\|\mathbf{b}\| = 1$ .  $\text{dist}(\mathbf{p}, l_i)$  is the length of the projection of  $\mathbf{p} - \mathbf{a}$  on to the plane perpendicular to  $\mathbf{b}$ , viz.

$$\text{dist}(\mathbf{p}, l_i) = \|P_{\mathbf{b}}(\mathbf{p} - \mathbf{a})\| \quad \text{with } P_{\mathbf{b}} = I - \mathbf{b} \otimes \mathbf{b}, \quad (7)$$

or, expressed with indices,  $P_{\mathbf{b},ij} = \delta_{ij} - b_i b_j$ . It is not difficult to show that  $\nabla_{\mathbf{p}} \text{dist}(\mathbf{p}, l_i)^2 = 2 P_{\mathbf{b}}(\mathbf{p} - \mathbf{a})$  implying that

$$\begin{aligned} \nabla_{\mathbf{p}} S = \mathbf{0} &\Rightarrow \sum_{i=1}^n P_{\mathbf{b}_i} \mathbf{p} = \sum_{i=1}^n P_{\mathbf{b}_i} \mathbf{a}_i \\ \mathbf{p} &= \left( \sum_{i=1}^n P_{\mathbf{b}_i} \right)^{-1} \sum_{i=1}^n P_{\mathbf{b}_i} \mathbf{a}_i \end{aligned} \quad (8)$$

and substitution into (6) gives the minimum  $S$ .

However, the number of calculation of  $S$  for all combinations of lines is of the order of  $1000^4 = 10^{12}$ , totally out of reach for a pc. We must therefore be very selective about the combinations to choose. We split up the procedure in several parts

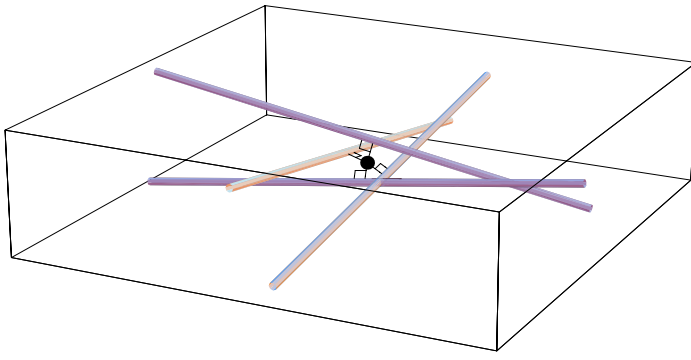


Figure 23. Four lines of sight almost crossing each other. The point in the middle is calculated by (8).

1. For any combination of two cameras, select pairs of lines that are close to each other (say, within a millimeter).
2. From the above mentioned sets of pairs, find quadruples of lines (i.e. lines from *four* cameras) that pairwise are close to each other and calculate  $S$  and particle positions according to (6) and (8). Return positions with  $S$  below a given threshold.
3. From the remaining pairs, find combination of lines from *three* cameras and return points with  $S$  below the threshold. Particles only defined by two cameras are not used.

The most computationally heavy task is 1. To see how we do that step, it is illustrative to look at the following simplified example: Imagine that the two cameras under investigation are very far from the tank and perfectly aligned such that the pixel coordinate  $y_c$  of each camera is proportional to the  $z$ -coordinate of the particle position. In this case lines are close to each other if and only if their  $z$ -coordinates are close to each other. Computationally, it is very fast to determine whether this is the case.

The trick is to generalise this simple algorithm to the case where the camera images no longer are simple linear mathematical projections, but are given by the calibration (4).

In the more general case we have two cameras not too far from the horizontal plane and that are oriented arbitrarily. (Pick any two cameras from figure 3.) Via the calibration (5) we are able to construct a line of sight  $l_1$  from the first camera which goes through the origo of the calibration box. We are able to make a similar line  $l_2$  from the second camera, and the the line through origo perpendicular to both lines is denoted  $l$ . We are now going to “project” all particle lines from both cameras onto this line. I.e. the line  $l$  has the same role as the  $z$ -axis in the simplified example above. If the cameras were exactly in the horizontal plane  $l$  would be the  $z$ -axis.

The way we project lines of sight from the first camera in to  $l$  is as follows. A point on a particle line (to be precise, the intersection of this line with the vertical midplane of the the calibration box) is first projected onto the plane spanned by  $l_1$  and  $l$  along lines of sight from the *second* camera (via the the calibration function (5)). Then the point is projected along the lines of sight from the *first* camera onto the plane spanned by  $l_2$  and  $l$ . Now the point is *very* close to the to the line  $l$  and it is projected orthogonally onto this line in order to find the  $l$ -coordinate corresponding to the  $z$ -coordinate in the simplified example above. In a similar way the lines of sight from the second camera are projected onto  $l$ .

We go through this complicated procedure because lines of sight that almost cross each other will also have almost the same  $l$ -coordinate, and it is *much* more computationally efficient than to calculate distances between *every* pair of lines of sight. If the cameras were perfect mathematical cameras (pin-hole cameras) with no intervening air-glass-water interface we would have: Two lines of sight crossing  $\iff$  The two lines have the same  $l$ -coordinate. This is not correct for a general calibration, but as long as the non-linear terms are small it is a good approximation. In practice we select all pairs of lines which have  $l$ -coordinate within 1 mm of each other.

Having found all pairs of lines of sight close each other for any combinations of cameras we are now able to go to the second item in the algorithm outlined above. Here we simply go through all combinations of close line pairs and say that we have found a potential particle if all four lines are mutually close to each other. We then calculate  $S$  for all the potential particles (see (6) and (8)), rank the particle according to  $S$  and take the particle with the lowest  $S$  as real. If the particle with the second lowest  $S$  does not have any lines in common with the first, we take that as a real particle. Otherwise it is dropped. We proceed in this way dropping particles that have lines in common with the ones with lower  $S$ .

Finally, among the remaining unused pairs we find all triples that pairwise are close to each other and prohibit the use of a line in more than one particle as with the quadruples above.

We could also have taken all pairs among the remaining unused pairs and postulated that these were particles. However, the probability of two particles accidentally having their lines of sight close to each other is too large. Moreover, particles only defined by camera 1 and camera 2 would have a relatively large uncertainty on the determination of the distance from the cameras, because the cameras are close to each other. Requiring at least one extra camera to be able to see the particles eliminates much of this uncertainty.

The procedure used here is quite different from the one used by Dracos (1996). They project the line of sight of one camera back through an other camera and find the point closest to this curve on the CCD chip. We prefer to work in physical space.

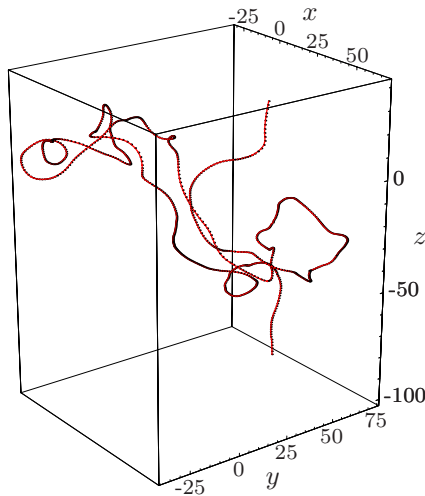


Figure 24. The longest track observed in the experiments. It consists of approximately one thousand points, i.e. 40 seconds.

### 3.4 Tracking

So far we have described how to obtain the three-dimensional positions of particles. This is done from video images obtained at a rate of 25 per second. The purpose of tracking is to correctly link particle positions at consecutive instants. In this way we can obtain long particle tracks that are necessary for the study of relative dispersion.

Malik, Dracos and Papantoniou (1993) show that an important parameter in determining whether tracking is possible is

$$p = \frac{\Delta_0}{\sigma \Delta t}, \quad (9)$$

where  $\sigma$  is the rms velocity fluctuation of one component of the velocity,  $\Delta t$  the time step (in our case 0.04 s), and  $\Delta_0$  the mean spacing of particles in the volume, defined as  $(V/N)^{1/3}$ , where  $V$  is the volume and  $N$  the number of particles in that volume. When  $p \ll 1$  tracking is impossible because in each time step the particles move much longer than the average spacing making mismatch very likely. When  $p \gg 1$  tracking is easy.

In our case we have  $\Delta_0 = 10 - 15$  mm and  $\sigma \Delta t \approx 1$  mm, so  $p \approx 10 - 15$ . Malik et al. (1993) show that in order to get long tracks  $p$  must be larger than 10. This restricts the simultaneous determination of high resolution velocity fields, but the main purpose of this work is to investigate Lagrangian statistics. When it is less important to obtain long tracks,  $p$  may be lowered considerably (Dracos 1996).

Our procedure, a slightly simplified version of Malik et al.'s (1993), may be summarized as follows: Four instants of the particle positions are present: 'remote past', 'past', 'present' and 'future'. As many links as possible are found between the remote past, the past and the present, and the exercise now is to link the present points with the future. The first step is for a given particle in the present to find its most probable future position. There are several possibilities:

1. The particle *is not* linked to the past:
  - (a) If it has neighbours within a radius  $r_0$  (to be defined later) that are linked to the past, the most probable change in its future position  $\mathbf{r}_{\text{fut}}$  is the average speed of its neighbours times  $\Delta t$ .
  - (b) If not,  $\Delta \mathbf{r}_{\text{fut}} = 0$ .
2. The particle *is* linked to the past:
  - (a) If the particle is not linked to the remote past,  $\mathbf{r}_{\text{fut}}$  is found by assuming constant velocity.
  - (b) If it is linked to the remote past,  $\mathbf{r}_{\text{fut}}$  is found by assuming constant acceleration.

For each most probable future position  $\mathbf{r}_{\text{fut}}$ , all particles in a spherical neighbourhood around this point are found. If no links were found to the past (i.e.  $\Delta \mathbf{r}_{\text{fut}} = 0$ ) the radius of the neighbourhood is  $3r_1$  and else  $3r_2$ , both to be defined later. Usually, there is only one point in this neighbourhood and the tracking is simple. However, there may be more than one and two particles in the present that point to the same particle in the future. To sort out which potential links to drop we attach a probability to each link:

$$P = \frac{1}{(2\pi)^{3/2} s^3} \exp\left(-\frac{1}{2} \frac{|\mathbf{r} - \mathbf{r}_{\text{fut}}|^2}{s^2}\right), \quad (10)$$

where  $\mathbf{r}$  is the position of the potential future particle, and  $s$  is either  $r_1$  or  $r_2$  according to whether links to the past have been found. Potential links with lower probabilities are dropped if they interfere with higher probability links. In this way a self consistent set of links are found.

The parameter  $r_0$  is the radius of the volume in which to search for velocities if the particle under consideration is not linked to the past. This only makes sense if all the particle velocities within  $r_0$  are well correlated. The Taylor microscale  $\lambda$ , is the relevant length scale in this context, so

$$r_0 = \lambda. \quad (11)$$

If the particle density is very high one may find a lot of particles within  $\lambda$  and  $r_0$  may be reduced even further to get a better estimate of the velocity at the particle under consideration. In our case we rarely find more than a few particles within  $\lambda$ .

The radius  $r_1$  is rms distance a particle can deviate from its current position in one time step without any knowledge of its past. This is  $\sigma\Delta t$ , where  $\sigma$  is the rms velocity of one component of the velocity vector. To follow Malik et al. (1993), we add the random error of the position determination  $r_{\text{jit}}$  and get

$$r_1 = \sqrt{(\sigma\Delta t)^2 + r_{\text{jit}}^2}. \quad (12)$$

The typical situation in our experiment is that  $\sigma\Delta t$  is by far the dominating term. The search radius of the neighbourhood is chosen to be  $3r_0$  which should cover almost all possibilities.

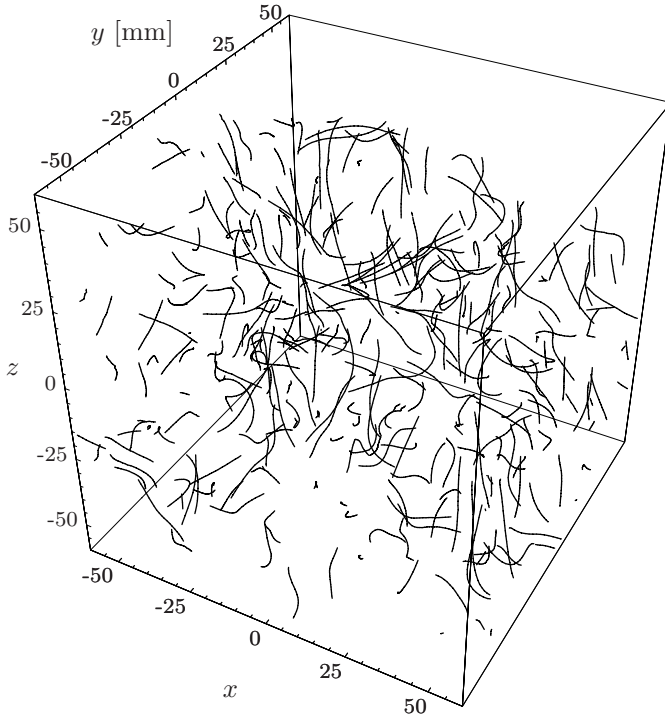


Figure 25. One second of data consisting of 400 unbroken tracks of each 25 points. Some of the tracks are almost point-like. i.e. almost zero velocity, while others move several centimeters.

The radius  $r_2$  is rms distance a particle can deviate from its current position in one time step assuming that its velocity is know. Malik et al. (1993) estimates crudely, that

$$r_2 \approx \sqrt{A\pi C^L L(\sigma\Delta t)^{3/2}}, \quad (13)$$

where  $C^L \approx 2.4$  is the Lagrangian frequency spectrum constant,  $L$  the integral scale, and  $A$  an empirical constant in the relation  $\varepsilon \approx A\sigma^3/L$ . Most parameters in this expression are not very well known, but the tracking performance does not depend very strongly on the choice of  $r_2$ . The random error  $r_{\text{jit}}$  is added to  $r_2$ .

Malik et al. (1993) are a bit more sophisticated in their analysis. If they encounter ambiguities in the tracking they favor the link with the smallest *change* in acceleration. Due to our large value of the particle tracking parameter  $p$  we have not felt it necessary to go to this level of sophistication. Malik et al. (1993) are testing for how low values of  $p$  they can track with reasonable yields. At  $p < 3$  they show that tracking is virtually impossible.

Examples of tracks found by our procedure are shown in figure 24 and 25. The probability of finding a particle in a track of a given length greater than zero is shown in figure 26. It can be seen that the length of the tracks decreases with increasing number of particles: Run 16 (solid curve) has almost 8 times as many particles as run 12 (dashed curve), all other things being equal.

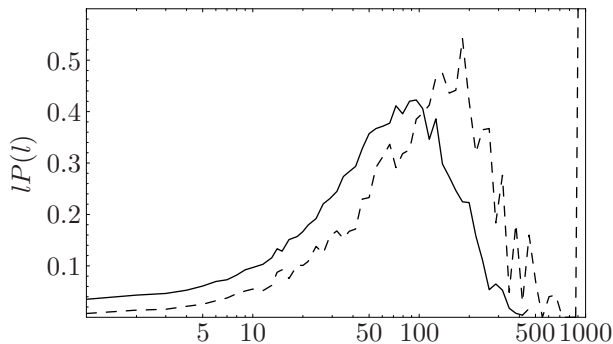


Figure 26. The probability of finding a particle in track of length  $l$ . The dashed curve is for run 12 which has much fewer particles than run 16, the solid curve. Note that the probability density function  $P(l)$  has been multiplied with  $l$  such that equal areas under the curve represent equal probabilities.

### Location of nearest neighbours

A crucial step for the efficiency of the computer code is how fast we are able to locate particles in a small neighbourhood (with radius  $r_0$ ,  $r_1$  or  $r_2$ ) around an extrapolated future position. We do that by “bucketing” in which we divide the space into a regular grid of boxes (buckets) and calculate in which boxes the particles are located. If  $n$  is the number of particles we divide the volume into of the order of  $n$  boxes, so on average there is one particle per box. The process of sorting into boxes is  $O(n)$  in time and is very simple to program. It is basically a truncation of the position  $(x, y, z)$  into a set of integers.

Once this is done it takes  $O(1)$  in time to locate all particles in small neighbourhood around a point  $\mathbf{r}$  as long as the radius is not larger than the mean average particle separation  $\Delta_0$ . This is done by only investigating the boxes that cover the sphere of interest.

## 3.5 Uncertainty of the position determination

In this section we shall estimate the uncertainty of the position determination in two ways. The first way is similar to the one shown in figure 18 and 19 concerning uncertainties on CCD positions in a quiescent flow, but here we will be interested in positions in space. However, this does not work in very turbulent flows, because it is difficult to distinguish noise from small scale turbulence. In the second method we are trying to make that distinction by investigating the Lagrangian acceleration auto-correlation.

The sources of the position uncertainties in these measurements are

- misalignment of scan lines in the cameras (jitter)
- oscillations in the experimental setup
- finite pixel size
- intensity resolution
- photon statistics

Jitter is probably the largest single source of measurement uncertainties. It is caused by misalignment of the scan lines in the video signal, and will result in random fluctuations of the particle positions along the scan lines. The scan lines are almost parallel to the  $z$  axis, so we expect much larger variations in the  $z$  component than in the  $x$  and  $y$  components.

The flow is forced by the two oscillating grids. This also results in movement of the container itself<sup>6</sup>. The eigenfrequencies of the container are in the kHz range so these oscillations will show up as uncorrelated noise in the 25 Hz measurements. We would of course expect the noise in the measurements to grow with growing driving frequency.

The finite size of the pixels and the limited intensity resolution sets a limit for how precise measurements we can make, even if there was no noise in the system. If the size of images of the particles on the CCD's were close to a single pixel, there would be a certain bias towards locating the particles at the center of a pixel position. With infinitely small particles, we would never have an image covering several pixels, and the particle would always be located at the center of a pixel position. With particles much larger than a pixel, we will always have overlap, and the precision of the position estimate (if we know the intensity distribution from a particle) is limited by the intensity resolution and the number of pixels where the intensity varies from that of the 'interior' of the particle (and from the background).

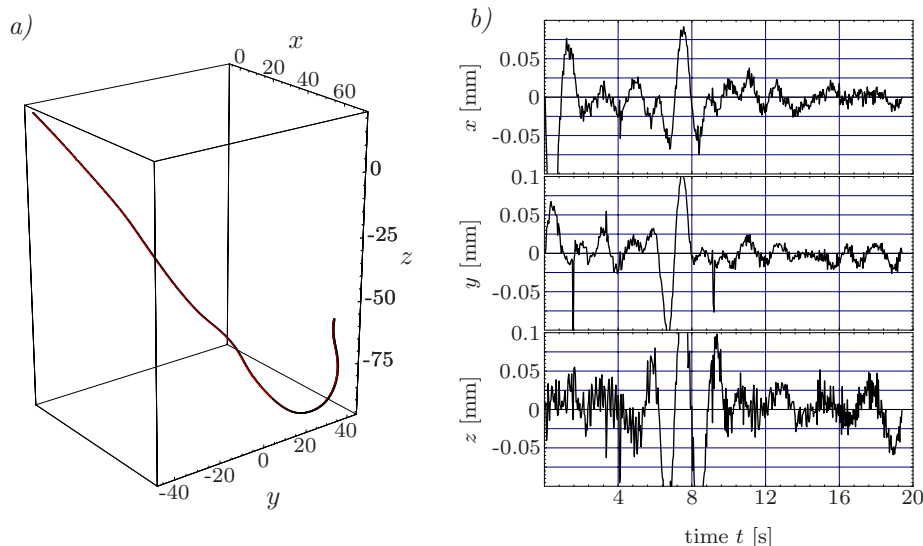


Figure 27. a) An approximately 20 seconds (485 points) long track in decaying turbulence. b) Residues of the  $x$ -,  $y$ - and  $z$ -component of the track with smooth curve subtracted.

Photon statistics is also a source of errors in the measurements, but we work with sufficient light intensities that we do not expect it to be visible among the other sources.

<sup>6</sup>At  $A = 50$  mm,  $f = 3.5$  Hz, counter phase we could even see the windows in the container vibrate. No tracking data were acquired with this setup.

In addition to this, there might be some small systematic errors due to the finite thickness of the plates we use for calibration (see section 3.2). The index of refraction of the plates is different from that of the water, and the finite thickness of the plates can thus result in a translation of the apparent position of the points on the back-plates in the calibration box.

### A ‘calm’ track

Figure 27a shows a track from an experimental run with decaying, weak turbulence and with the grid motors stopped. As done in the previous analysis with the estimation of the uncertainty on the CCD chip, a cubic spline fixed at one point every second is subtracted from the track in order to estimate the random uncorrelated noise for the 3D position. According to figure 27b the uncertainty is estimated to

$$\sigma_x \approx \sigma_y \approx 0.01 \text{ mm} \quad \sigma_z \approx 0.02 \text{ mm} \quad (14)$$

### Estimates of position uncertainties by Lagrangian statistics

We assume that the measured positions of a particle at the discrete times  $t_n$ ,  $\tilde{x}_i(t_n)$ , can be split up in the actual position,  $x_i(t_n)$ , and an uncorrelated noise term,  $\eta_i(t_n)$ :

$$\tilde{x}_i(t_n) = x_i(t_n) + \eta_i(t_n), \quad i \in \{x, y, z\}, \quad (15)$$

$$\langle \eta_i(t) \cdot \eta_j(t + \tau) \rangle = \delta_{ij} \cdot \delta(\tau) \cdot \sigma_i \sigma_j \quad (\text{nosummation}), \quad (16)$$

$$\langle \eta_i(t) \rangle = 0. \quad (17)$$

The mean squared separation of the noisy measurements is

$$\tilde{D}_i(\tau_m) = \langle \Delta \tilde{x}_i^2(\tau_m) \rangle = \langle (\tilde{x}_i(t_n + \tau_m) - \tilde{x}_i(t_n))^2 \rangle = \begin{cases} 0 & , \text{ for } \tau_m = 0 \\ D_i(\tau_m) + 2\sigma_i^2 & , \text{ for } \tau_m \neq 0 \end{cases} \quad (18)$$

If we knew the shape of  $D_i(\tau)$ , eg. a parabola, we would be able to estimate  $\sigma_i$ . However  $\sigma_i$  is very small and the shape of  $D_i(\tau)$  is not known with sufficient accuracy.

It turns out that it is more rewarding to look at the Lagrangian acceleration correlation

$$R_i(\tau) \equiv \langle a_i(t) a_i(t + \tau) \rangle, \quad (19)$$

where noise has a larger impact. The particle accelerations are estimated using three succeeding points:

$$\tilde{a}_i(t_n) = \frac{\tilde{x}_i(t_{n-1}) - 2\tilde{x}_i(t_n) + \tilde{x}_i(t_{n+1}))}{\Delta t^2}. \quad (20)$$

Using this estimate in stead of the actual accelerations we get

$$\tilde{R}_i(\tau) \equiv \langle \tilde{a}_i(t) \tilde{a}_i(t + \tau) \rangle = \begin{cases} R_i(\tau) + 6 \frac{\sigma_i^2}{\Delta t^4} & , \text{ for } \tau = 0 \\ R_i(\tau) - 4 \frac{\sigma_i^2}{\Delta t^4} & , \text{ for } \tau = \pm \Delta t \\ R_i(\tau) + \frac{\sigma_i^2}{\Delta t^4} & , \text{ for } \tau = \pm 2\Delta t \\ R_i(\tau) & , \text{ for } \tau = \pm n\Delta t, \text{ with } n > 2. \end{cases} \quad (21)$$

We do not have sufficient resolution of the Lagrangian acceleration correlation functions to allow us to use them for determining the position uncertainties directly, but their Fourier transforms can be used to find an upper limit of the noise intensity

$$R_i(\omega) = |a(\omega)|^2 \geq 0 \quad (22)$$

The same relation must be true for  $\tilde{R}_i(\omega)$  and  $R_{\eta_i}(\omega)$ . Since we assume that the noise is uncorrelated with the signal we have

$$|\tilde{a}_i(\omega)|^2 = |a_i(\omega)|^2 + |\eta_i(\omega)|^2. \quad (23)$$

Rearranging this and taking into account that power spectra are non-negative, we get

$$|\tilde{a}_i(\omega)|^2 > |\eta_i(\omega)|^2. \quad (24)$$

The power spectrum of the noise is similarly equal to the Fourier transform of the noise part of the autocorrelation function.

$$|\eta_i(\omega)|^2 = \frac{\sigma_i^2}{\Delta t^4} [6 - 8 \cos(\omega \Delta t) + 2 \cos(2\omega \Delta t)]. \quad (25)$$

Figure 28 shows the Fourier transform of a corrected measured acceleration auto-correlation function (equivalent to the corrected power spectrum of the measured accelerations) and the power spectrum of the noise estimate with  $\sigma_i$  maximised within the limits set by equation 24.

The spike in the power spectrum of the  $z$  component of the acceleration in data set 21 (lower graph in figure 28) is located at the drive frequency for those measurements. We never see such a spike when the two grids are moving in counter-phase.

Using this method we have found upper limits for  $\sigma_i$  for all the measurements. These data are found in table 4.

Table 4. Upper bounds for position standard deviations derived through equation 24.

Measurement	$\sigma_x$ [mm]	$\sigma_y$ [mm]	$\sigma_z$ [mm]
Decaying turbulence	0.0147	0.0126	0.0169
12	0.0291	0.0314	0.0281
13	0.0365	0.0484	0.0325
14	0.0354	0.0474	0.0325
15	0.0453	0.0612	0.0388
16	0.0446	0.0613	0.0394
17	0.0414	0.0590	0.0350
20	0.0596	0.0399	0.0390
21	0.0586	0.0383	0.0380
22	0.0587	0.0334	0.0316

## 4 Basic flow characteristics

Nine runs of approximately one minute length are analysed (see table 5). In this section we discuss the mean flow, variances and make estimates of the energy dissipation based on the second order structure function. In section 5 we explore the possibilities of a more rigorous way of estimating the energy dissipation.

Before the nine runs shown in the table we ran a 20 s run with decaying turbulence. This was done by running the grids at 3 Hz with a stroke of 50 mm for a while and stopping them 10 seconds before the recording. Examples of tracks from this run are shown in figures 18, 19 and 27.

The first column in table 5 is the run number. The second is the grid configuration (A: Grids oscillating in anti-phase; P: Grids in phase). The next column is

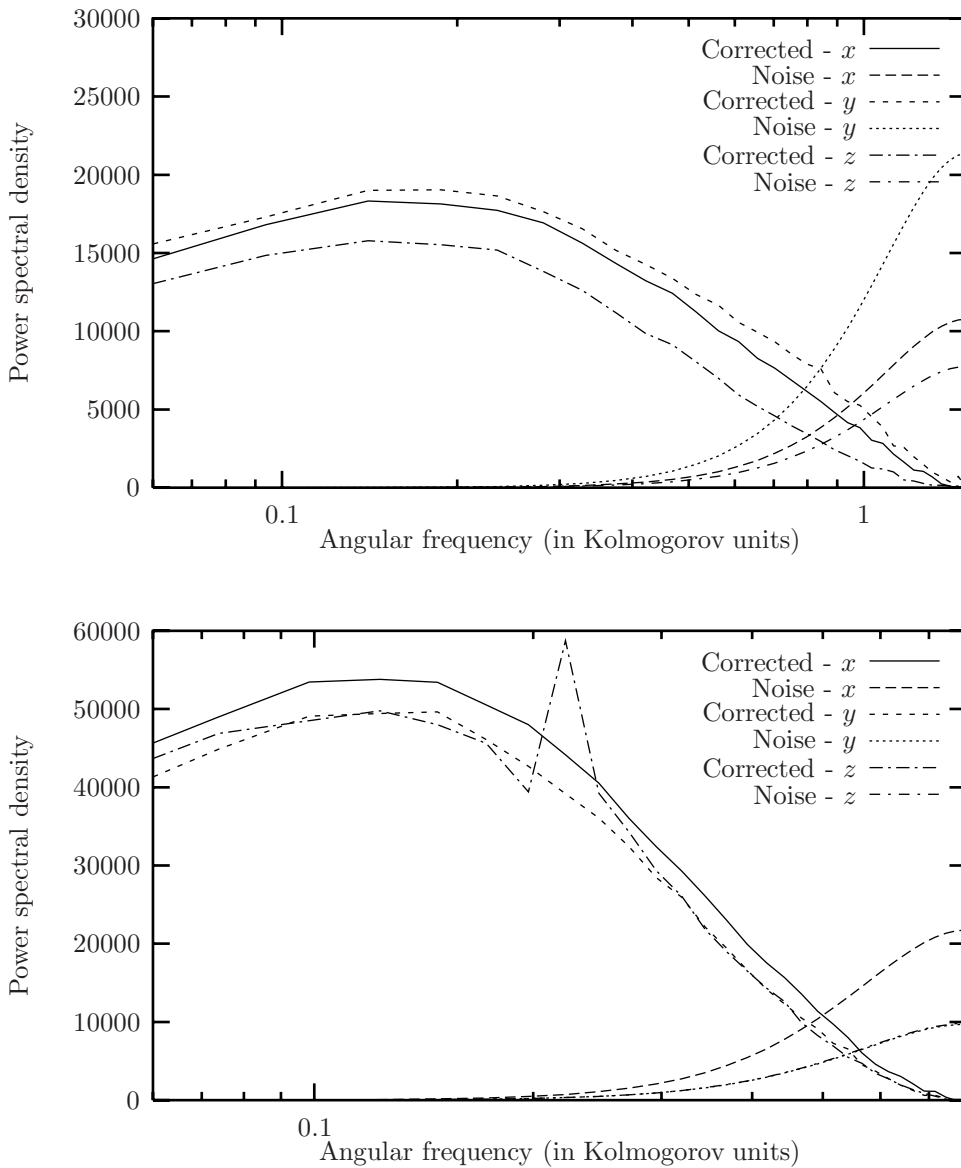


Figure 28. Acceleration power spectra for the data sets 17 (upper) and 21 (lower). Both data set corrected with the largest  $\sigma_i$ 's allowed by equation 24 with  $|\eta(\omega)|^2$  defined by 25. The corrections are also shown. The spike in the  $z$  component on the lower figure is located at the forcing frequency.

the oscillation frequency of the grids. The two following are the average number of measured velocities per time step and the average number of measured velocities in the sub-volume  $V_1 = [-70, 70] \times [-70, 70] \times [-80, 40]$  mm<sup>3</sup>, which is used for much of the analysis in this section<sup>7</sup>. The last four columns are the average number of particles identified by the four cameras.

After run 12 and 14 more particles were added to the water. It can also be seen that for the last three runs, where the grids run in anti-phase, there are slightly fewer measured velocities than in the previous runs, and there is fewer particles seen from the cameras (especially camera 1). Two things have probably happened. Firstly, changing the grid configuration has changed geometry of the experiment. This can be seen by the fact that the calibration for run 20, 21 and 22 is slightly

<sup>7</sup>Other averaging volumes used in the following section are given by (106).

Table 5. Summary of the experimental runs analysed in this report. Every run is slightly less than 60 s long, i.e. 1500 times steps. The peak to peak amplitude of the grid oscillation is 50 mm. The temperature of the water is 27.5 °C in run 12 slowly rising to 27.8 °C in run 22.

Run	Grid conf.	freq [Hz]	no. vel.	vel. in $V_1$	CCD 1	CCD 2	CCD 3	CCD 4
12	A	3.00	101	81	159	152	171	165
13	A	2.99	336	276	541	516	569	553
14	A	2.98	345	282	552	525	583	566
15	A	2.96	664	553	1111	1053	1174	1128
16	A	2.97	642	535	1094	1038	1177	1126
17	A	2.00	681	561	1092	1037	1166	1114
20	P	3.50	530	438	1010	1015	1139	1081
21	P	3.45	528	437	976	984	1100	1050
22	P	2.00	602	491	1051	1058	1187	1133

different from and presumably not so good as for the other runs. Secondly, in the few hours it took to change the grid configuration particles might have settled in the upper and lower corners of the box because of imperfect density. In the first few runs after this break not all particles might have been stirred into the bulk flow.

## 4.1 Where are the velocities measured?

The probability density function of particles inside tracks (i.e. positions where it is possible to calculate the velocity and acceleration) is shown in figure 29. Ideally, the probability density should be constant on a convex polyhedron defined by the intersection of the viewing cones of the cameras and the (ideally, sharply defined) light cone, and zero outside. It is calculated by counting velocities in a division of the volume  $[-140, 140] \times [-140, 140] \times [-140, 140] \text{ mm}^3$  in to  $15 \times 15 \times 15$  cubes. In total for all the runs 6.5 million velocities have been measured.

The left column in figure 29 are slices of this pdf. It seems that the inside of the pdf is fairly flat, but that the edges are somewhat blurred. Also shown in this figure is the sub-volume  $V_1 = [-70, 70] \times [-70, 70] \times [-80, 40] \text{ mm}^3$ , which is going to be used for much of the analysis in this section.

## 4.2 Mean flow

It is very important not to have a too large mean flow because we would like to track particles for as long time as possible. It is evident from figure 24 (from run 12) and just from looking at the experiment that a large mean flow is not dominating the flow. However, as we have discussed in section 2 a single oscillating grid produces a large mean flow, so one should expect at least some mean flow from two grids. In our experience, if the grids are not placed perfectly symmetrical with respect to the horizontal symmetry plane of the box, then there is a mean flow visible to the unaided eye. When the grids are placed symmetrical it is less clear to an observer what is fluctuations and what is an inhomogeneous mean flow.

In figure 30 is shown the mean velocity field calculated by averaging the velocities found in each of  $5 \times 5 \times 5$  boxes dividing the volume  $V_1$ . In order to get a clearer picture we have averaged all runs at the same grid frequency. The mean flow might be interpreted as somewhat inhomogeneous inflow through the top

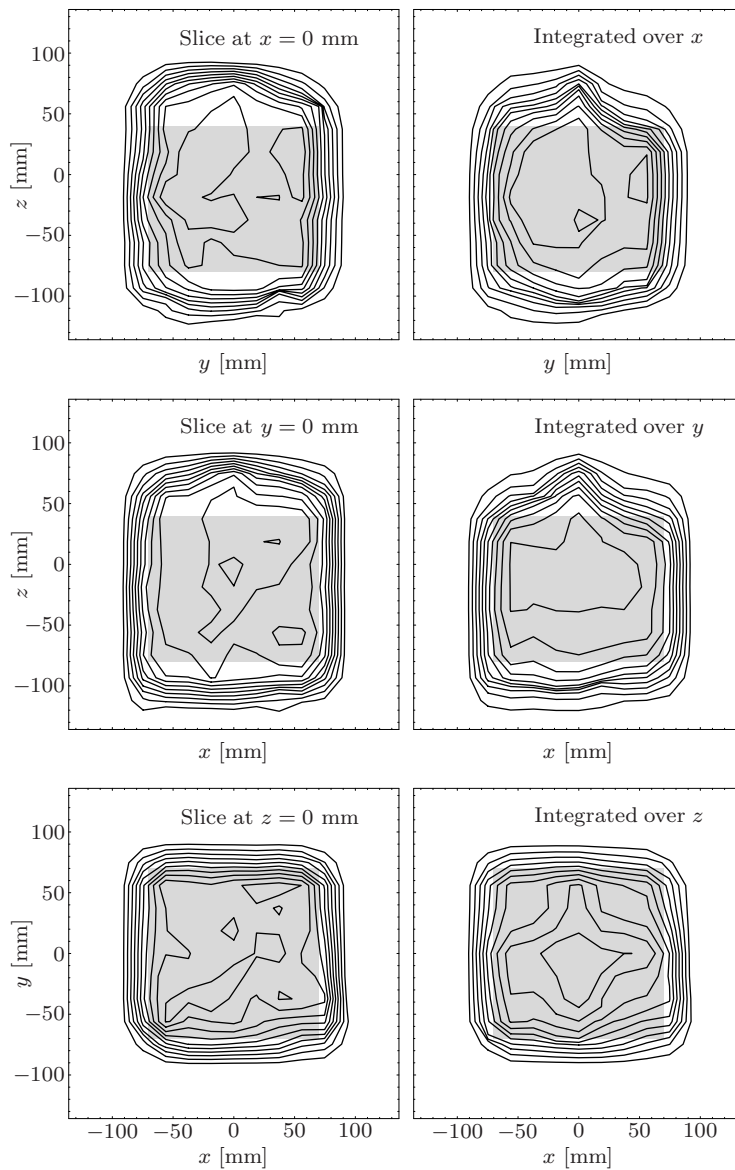


Figure 29. Equidistant contours of probability density functions of particle positions inside tracks. The plots in the left column are slices through the three-dimensional pdf. In the right column are two-dimensional pdf obtained by integration of the three-dimensional pdf. The shading indicates the measurement volume  $V_1$ .

and the bottom of the volume and outflow trough the sides. The mean flow at the center seems to be the smallest and the mean flow at all frequencies have many similarities making us confident that it really is a mean flow we are looking at. The root-mean-squared of the mean velocities averaged of the the entire field is shown in table 6.

As also seen from the fields in figure 30 the mean flow in the  $z$ -direction is strongest, and the  $x$ - and  $y$ -components grow in proportion with increasing frequency. However, it is a bit surprising that the  $z$ -component stays constant with grid frequency.

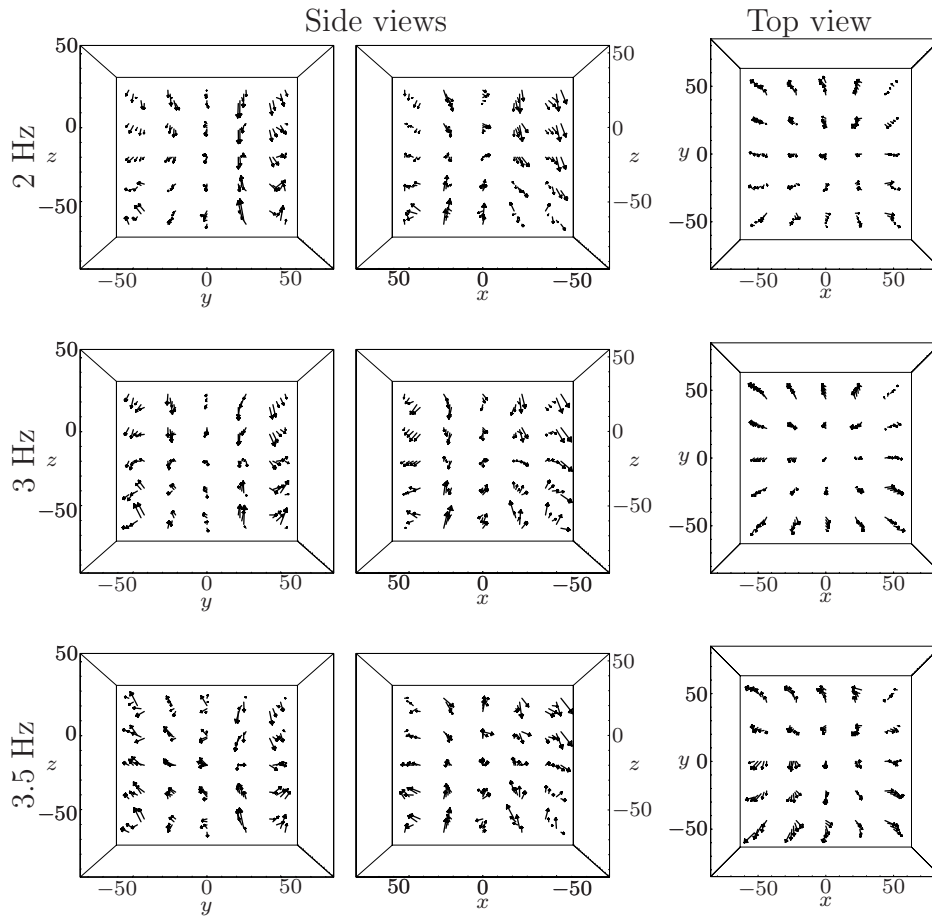


Figure 30. The mean flow as seen from the positive  $x$ - and  $y$ -axes (Side views) and from the positive  $z$ -axis (Top view). All axes have the unit of mm.

Table 6. The rms of the inhomogeneous mean velocity fields shown in figure 30 at the different grid driving frequencies. All numbers have the unit of mm/s, and  $u$ ,  $v$ , and  $w$  are velocities in the  $x$ -,  $y$ -, and  $z$ -direction, respectively.

	$u$	$v$	$w$
2.0 Hz	2.8	2.6	5.3
3.0 Hz	3.5	3.2	5.3
3.5 Hz	4.0	4.5	5.1

### 4.3 Standard deviations

The standard deviation of a component of the velocity is defined as

$$\sigma_u \equiv \sqrt{\langle (u - \langle u \rangle)^2 \rangle} \quad (26)$$

where  $\langle \rangle$  denotes the ensemble averaging. In practice, ensemble averages are not possible to obtain, so when calculating the standard deviation as a function of  $z$ ,  $\langle \rangle$  should be understood as the average over a horizontal slab with dimensions  $140 \times 140 \times 8 \text{ mm}^3$ . The spatial variations of the inhomogeneous mean flow will therefore slightly increase the calculated standard deviation.

The result is shown in figure 31 with one set of curves for each run. The two horizontal components are very similar,  $\sigma_v \approx \sigma_u$ , while  $\sigma_w \approx 1.25\sigma_u$ . This shows that the flow is anisotropic, but the results are consistent with axial symmetry.

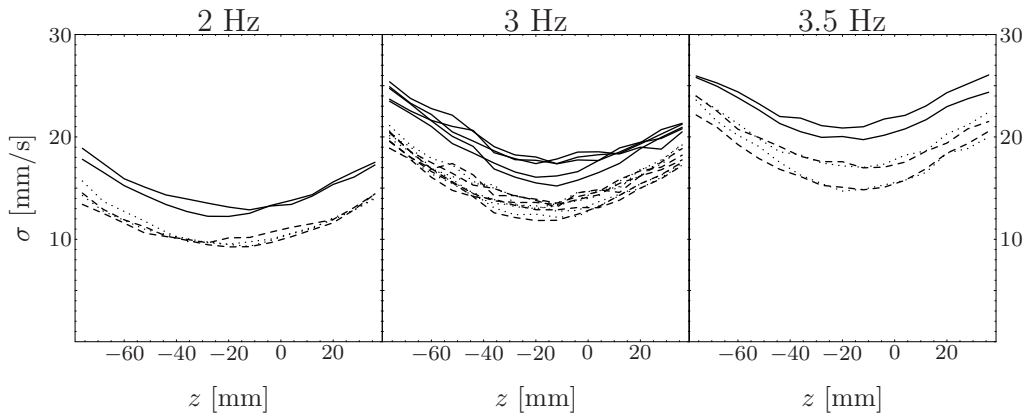


Figure 31. Standard deviation of the three velocity components  $u$  (dotted),  $v$  (dashed) and  $w$  (solid curve) as functions of the vertical coordinate  $z$ . Results for several experiments are shown together.

The same conclusion drawn from the more detailed analysis of the anisotropy presented in section 8.1, which also indicates that the flow is axi-symmetric.

#### 4.4 The second order structure function

In this section we will determine the second order structure function and from it extract the energy dissipation  $\varepsilon$  and the integral length scale. This is not a very fundamental way of calculating the energy dissipation because it relies on knowledge of an empirical constant, namely, the Kolmogorov constant. In section 5 we shall investigate more fundamental ways of calculating  $\varepsilon$  that are, at least in principle, possible with particle tracking data.

Two second order structure functions are calculated. The longitudinal structure function

$$f(r) \equiv \langle \delta v_{\parallel}^2(r) \rangle, \quad (27)$$

and the transversal structure function

$$g(r) \equiv \langle \delta v_{\perp}^2(r) \rangle. \quad (28)$$

The velocity difference  $\delta \mathbf{v}(\mathbf{r})$  is  $\mathbf{v}(\mathbf{r}_1) - \mathbf{v}(\mathbf{r}_2)$  and  $\delta v_{\parallel}$  is defined as the component of this in the direction of  $\mathbf{r} = \mathbf{r}_1 - \mathbf{r}_2$ , i.e.  $\delta \mathbf{v} \cdot \mathbf{r} / r$ . In principle, the structure functions should be functions of  $\mathbf{r}$  not  $r$ . However, in this section we calculate them by averaging over all  $\mathbf{r}_1, \mathbf{r}_2 \in V_1$  such that  $|\mathbf{r}_1 - \mathbf{r}_2|$  is in a small interval around  $r$ . In section 8.1 we look more carefully at the dependence on  $\mathbf{r}$ .

Kolmogorov (1941b) showed for inertial subrange separations that

$$\langle \delta v_{\parallel}^2(r) \rangle = C_K (\varepsilon r)^{2/3}, \quad (29)$$

and under the assumption of homogeneity and isotropy that

$$\langle \delta v_{\perp}^2(r) \rangle = \frac{4}{3} \langle \delta v_{\parallel}^2(r) \rangle \quad (30)$$

where  $C_K$ , the Kolmogorov constant, has to be determined experimentally. Through a review of many sources Monin and Yaglom (1975) found that  $C_K \approx 2.0$ . Later Chasnov (1991)<sup>8</sup> found that slightly newer experiments both in the atmosphere and in the laboratory scatter between 1.75 and 2.75 with an average of  $C_K \approx 2.1$ . Chasnov also compiled predictions from DNS (and a few LES), which has roughly the same Reynolds number as the flow in the middle of our tank. These values scatter between 2.1 and 3.2 with a single outlier at 5, and tended to cluster

<sup>8</sup>Chasnov actually cited values of  $\alpha$ . See the relation (32).

around  $C_K \approx 2.6$ . A newer collection of high Reynolds number experiments done both in the atmosphere and in a large wind tunnel in the Reynolds number range  $R_\lambda = (2.0 - 12.7) \times 10^3$  show a decrease of  $C_K$  with Reynolds number, starting at  $C_K = 2.5$  at the lower limit and  $C_K = 2.1$  at the highest  $R_\lambda$ . It seems that the Monin and Yaglom (1975) value of 2.0 is plausible, but might be somewhat low, at least for lower Reynolds numbers, and that  $C_K = 2.5$  could be just as good.

The energy spectrum corresponding to (29) and (30) is

$$E(k) = \alpha \varepsilon^{\frac{2}{3}} k^{\frac{5}{3}} \quad (31)$$

where  $k$  is the wavenumber, and the relation between  $C_K$  and  $\alpha$ , the so-called spectral Kolmogorov constant, is (Monin and Yaglom 1975)

$$C_K = \frac{27}{55} \Gamma\left(\frac{1}{3}\right) \alpha \approx 1.315\alpha. \quad (32)$$

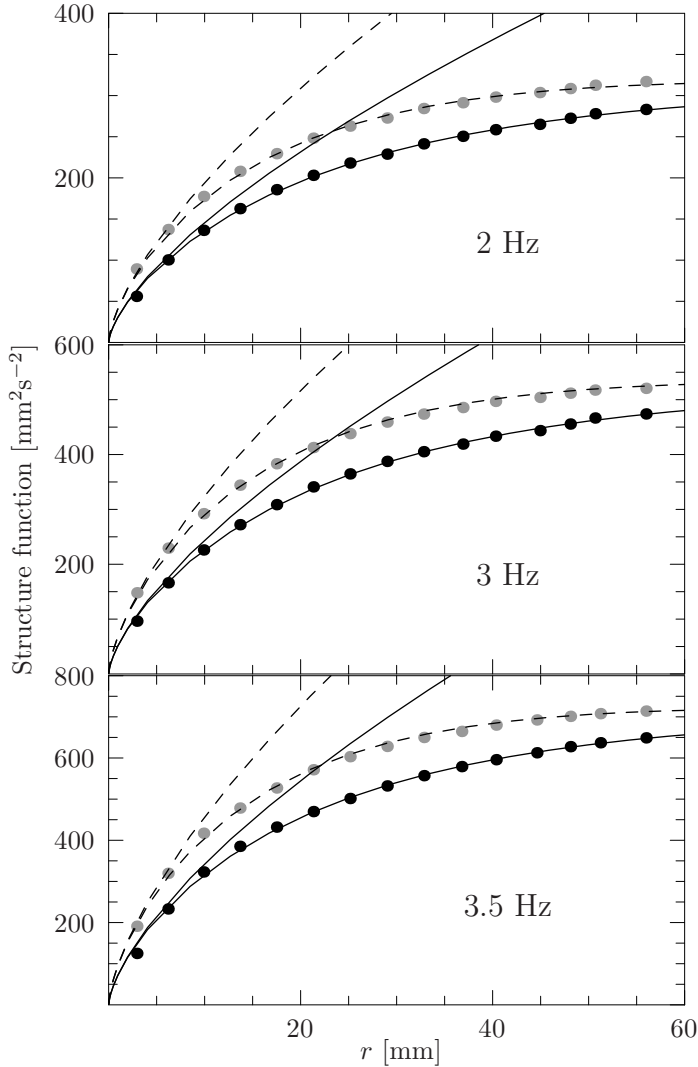


Figure 32. Measured longitudinal (black dots) and transversal (grey dots) structure functions from run 17 (2 Hz), 15 (3 Hz) and 21 (3.5 Hz). The solid curves are a fit of (34) to the data and the corresponding inertial subrange expression (29). The dashed curves are (35) and (30) using the parameters from the fit.

Under many circumstances, especially when turbulence is close to being isotropic, the energy spectrum proposed by von Kármán (1948)

$$E(k) = \alpha \varepsilon^{\frac{2}{3}} L^{\frac{5}{3}} \frac{(Lk)^4}{(1 + (Lk)^2)^{\frac{17}{6}}}, \quad (33)$$

where  $L$  is a length scale, fits measured data well. It can be shown (assuming isotropy and incompressibility), that the corresponding structure functions are

$$\langle \delta v_{\parallel}^2(r) \rangle = \frac{18 \pi^{\frac{1}{2}} 2^{\frac{2}{3}}}{55 \Gamma(\frac{5}{6})} \alpha \varepsilon^{\frac{2}{3}} \left\{ \frac{2^{\frac{1}{3}} \pi}{3^{\frac{1}{2}} \Gamma(\frac{2}{3})} - \left(\frac{r}{L}\right)^{\frac{1}{3}} K_{\frac{1}{3}}\left(\frac{r}{L}\right) \right\} \quad (34)$$

and

$$\langle \delta v_{\perp}^2(r) \rangle = \frac{18 \pi^{\frac{1}{2}} 2^{\frac{2}{3}}}{55 \Gamma(\frac{5}{6})} \alpha \varepsilon^{\frac{2}{3}} \left\{ \frac{2^{\frac{1}{3}} \pi}{3^{\frac{1}{2}} \Gamma(\frac{2}{3})} + \frac{1}{2} \left(\frac{r}{L}\right)^{\frac{4}{3}} K_{\frac{2}{3}}\left(\frac{r}{L}\right) - \left(\frac{r}{L}\right)^{\frac{1}{3}} K_{\frac{1}{3}}\left(\frac{r}{L}\right) \right\} \quad (35)$$

and that these reduce to (29) and (30) in the limit  $r \rightarrow 0$ .

Examples of measured structure functions are shown in figure 32. We have fitted the  $\langle \delta v_{\parallel}^2(r) \rangle$  data to (34) in order to obtain  $\alpha \varepsilon^{2/3}$  and  $L$ . These parameters are in turn used to calculate  $\langle \delta v_{\perp}^2(r) \rangle$  from (35). The dashed curves in the figure are thus not fits to the data but predictions. Clearly this works very satisfactory. Alternative methods to obtain  $\varepsilon$  will be discussed in section 5 .

### Derived quantities

The parameters  $\alpha \varepsilon^{2/3}$  and  $L$  obtained by the fit to (34) are shown in table 7. From these parameters we can calculate the variance of one component of the velocity through the identity

$$\frac{3}{2} \sigma^2 = \int_0^{\infty} E(k) dk = \frac{27 \pi^{\frac{1}{2}} \Gamma(\frac{1}{3})}{110 \Gamma(\frac{5}{6})} \alpha \varepsilon^{2/3} L^{2/3}, \quad (36)$$

where  $E(k)$  is the von Kármán form (33). The integral scale is defined via the correlation function  $R_{\parallel}(r) = \sigma^2 - \frac{1}{2} \langle \delta v_{\parallel}^2(r) \rangle$  as

$$L_{\text{int}} \equiv \int_0^{\infty} R_{\parallel}(r) dr = \frac{\pi \Gamma(\frac{5}{6})}{\Gamma(\frac{1}{3})} L. \quad (37)$$

The energy dissipation  $\varepsilon$  is obtained from  $\alpha \varepsilon^{2/3}$  through the relation (32) using Monin and Yaglom's (1975) value  $C_K = 2.0$ .

*Table 7. Summary of the derived parameters from the second order structure function based on measurements in the volume  $V_1$ .*

Run	$\alpha \varepsilon^{2/3}$ [mm $^{\frac{4}{3}}$ s $^{-2}$ ]	$L$ [mm]	$\sigma$ [mm/s]	$L_{\text{int}}$ [mm]	$\varepsilon$ [mm $^2$ s $^{-3}$ ]	$\tau_{\eta}$ [s]	$\eta$ [mm]	$\lambda$ [mm]	$R_{\lambda}$
12	43	30	17	23	149	0.077	0.26	5.1	96
13	45	31	18	23	160	0.075	0.26	5.1	100
14	41	27	16	20	140	0.080	0.27	4.9	88
15	40	29	16	22	135	0.081	0.27	5.1	93
16	45	28	17	21	160	0.075	0.26	4.9	91
17	24	29	12	22	62	0.120	0.33	5.8	81
20	65	29	21	22	279	0.056	0.22	4.5	104
21	56	28	19	21	225	0.063	0.24	4.6	97
22	25	27	12	20	65	0.117	0.32	5.6	78

The Kolmogorov length and time are defined by

$$\eta = \left(\frac{\nu^3}{\varepsilon}\right)^{1/4} \quad \tau_{\eta} = \left(\frac{\nu}{\varepsilon}\right)^{1/2}, \quad (38)$$

where the kinematic viscosity for water at 27.5 °C is  $\nu = 0.89 \text{ mm}^2/\text{s}$ . According to Hinze (1975) the Taylor micro-scale  $\lambda$  may be written as

$$\lambda = \sqrt{\frac{15\nu\sigma^2}{\varepsilon}} \quad (39)$$

and the Taylor micro-scale Reynolds number as

$$R_\lambda = \frac{\lambda^2}{15^{\frac{1}{2}}\eta^2}. \quad (40)$$

All these derived quantities are shown in table 7.

## 5 Determination of the energy dissipation

One of the most important characteristics of any turbulent flow is the mean rate of kinetic energy dissipation  $\langle\varepsilon\rangle$ , and the question of determining  $\langle\varepsilon\rangle$  from particle tracks arose early in the project. The method described in the previous section, which we will henceforth refer to as Method 1, is only one of several that we have tried.

A direct measurement from the definition

$$\langle\varepsilon\rangle = \nu \left\langle \frac{\partial v_i}{\partial x_j} \left( \frac{\partial v_i}{\partial x_j} + \frac{\partial v_j}{\partial x_i} \right) \right\rangle \quad (41)$$

involves simultaneous measurements of all components of  $\frac{\partial v_i}{\partial x_j}$ . This is extremely difficult because it requires the velocity field to be resolved down to the Kolmogorov scale  $\eta$ . By now the development of very small multi-hot-wire probes applicable to air flow measurements has reached a degree of perfection that enables differential velocity measurements to be taken with separations of only a few millimetres (e.g. Tsinober, Kit and Dracos 1992, Antonia, Zhou and Zhu 1998). We are unaware of similar results for measurements in liquids. However, the interpretation of hot-wire measurements rely on Taylor's hypothesis, hence they are best suited for flows with low turbulence intensity, i.e. large mean velocity magnitudes. This rules out hot-wires for our experiment (unless we use the difficult technique of moving hot wires). For a given experimental set-up the typical way to increase the Reynolds number would be to increase the speed of the turbulence generator, e.g. run the fan faster in a wind tunnel or oscillate the grids faster in our experiment. Thus the scale separation is increased by decreasing  $\eta$  while the integral scale is fixed. Therefore higher Reynolds numbers require better spatial resolution, and the use of (41) to determine  $\langle\varepsilon\rangle$  will become impossible as  $\eta$  gets too small to be resolved. Furthermore, in order to determine  $\left\langle \frac{\partial v_i}{\partial x_j} \frac{\partial v_i}{\partial x_j} \right\rangle$  from tracks, one must look for situations where two particles are simultaneously present in a volume on the order of  $\eta^{39}$ . Even for a massive seeding, this is a rare event, so the need for alternative methods to determine the energy dissipation is obvious.

Mean values involving spatial derivatives are difficult to measure, while spatial derivatives of mean values can be less problematic. For example the term  $\left\langle \frac{\partial v_i}{\partial x_j} \frac{\partial v_j}{\partial x_i} \right\rangle$  can be written as  $\nabla \cdot \langle \mathbf{a} \rangle$  (for a statistically stationary flow of an incompressible fluid). Evaluating  $\nabla \cdot \langle \mathbf{a} \rangle$  does not require resolution of small scales and is readily accessible from Particle Tracking (PT) estimates of the single-point average of

---

<sup>9</sup>In principle it is possible to determine the two-point statistic  $\langle v_i(\mathbf{x})v_i(\mathbf{x}') \rangle$ , and numerically compute  $\frac{\partial^2 \langle v_i(\mathbf{x})v_i(\mathbf{x}') \rangle}{\partial x_j \partial x'_j}$  for  $\mathbf{x} = \mathbf{x}'$ , but it does not work when  $\langle v_i(\mathbf{x})v_i(\mathbf{x}') \rangle$  is poorly determined for small separations  $\mathbf{x} \sim \mathbf{x}'$ .

the acceleration<sup>10</sup>. Thus we have found that this term is generally very small contributing by less than 1% to the energy dissipation.

It is natural to turn to structure functions since these are easily obtained from measured tracks. We define the symmetric second and third order structure functions in the following way:

$$B_{dd} \equiv \frac{1}{4\pi r^2} \int_{|\mathbf{y}|=r} \langle \delta v_{\parallel}^2 \rangle d^2y, \quad (42)$$

$$B_{ii} \equiv \frac{1}{4\pi r^2} \int_{|\mathbf{y}|=r} \langle \delta v^2 \rangle d^2y, \quad (43)$$

$$B_{ddd} \equiv \frac{1}{4\pi r^2} \int_{|\mathbf{y}|=r} \langle \delta v_{\parallel}^3 \rangle d^2y, \quad (44)$$

and

$$B_{dii} \equiv \frac{1}{4\pi r^2} \int_{|\mathbf{y}|=r} \langle \delta v_{\parallel} \delta v^2 \rangle d^2y. \quad (45)$$

The integrals are over a sphere and  $\delta v_i(\mathbf{y}) = v_i(\mathbf{x} + \mathbf{y}) - v_i(\mathbf{x})$ . These definitions make the structure functions invariant to rotations, because of the averaging over all directions of the separation. This invariance is a convenient property of the definitions which is independent of whether the flow ensemble is isotropic. The symmetric definitions require that all orientations of the separation are measured.

In the inertial range, we have the well known relations (Kolmogorov 1941b)

$$\langle \delta v_{\parallel}^2 \rangle = C_K (\langle \varepsilon \rangle r)^{2/3} \quad (46)$$

and (Kolmogorov 1941a)

$$\langle \delta v_{\parallel}^3 \rangle = -\frac{4}{5} \langle \varepsilon \rangle r. \quad (47)$$

Since these relations fail outside the inertial range, great care must be taken in using them to deduce  $\langle \varepsilon \rangle$  when no clear inertial range exists. The first relation, which was used in Method 1, has never been rigorously proved. Therefore a deduction of the Kolmogorov constant  $C_K$  from first principles is not available. Likewise there is no reason why  $\langle \varepsilon \rangle^{2/3}$  should not be replaced by  $\langle \varepsilon^{2/3} \rangle$ <sup>11</sup>. Even the two-third value of the exponent is debatable. Nevertheless, second order structure functions are widely used to obtain estimates of  $\langle \varepsilon \rangle$  - directly from (46) or by comparing the power spectrum with a Kolmogorov spectrum.

In (47), the four-fifth law, the numerical constant is exact. The relation can be proved under certain symmetry assumptions, as will be discussed in more detail later. From an experimental point of view, third order structure functions are more difficult to obtain than second order structure functions, because larger ensembles are needed to obtain reliable estimates. This is due to the long tails of the  $\delta v_{\parallel}$  distribution. The four-fifth law also seems to require larger Reynolds numbers than we can obtain. The advantage is that the numerical constant,  $4/5$ , is exact, even if several assumptions have to be made in order to derive the relation. In the derivation terms that may not be negligible at moderate Reynolds numbers are discarded. Despite such difficulty, an essentially direct determination of  $\langle \varepsilon \rangle$  would be a great advantage. It could for example be used to reverse Method 1 and determine  $C_K$ . We therefore felt that a careful rederivation of the four-fifth law, or

<sup>10</sup>Integrating over a test volume  $V$  we get  $\int_V \nabla \cdot \mathbf{a} dV = \int_{\partial V} \hat{\mathbf{n}} \cdot \mathbf{a} dA$ . The surface integral can be evaluated by averaging  $\hat{\mathbf{n}} \cdot \mathbf{a}$  over a thin shell.

<sup>11</sup>This would make Landau's objection to the formula obsolete (see e.g. Frisch 1995).

a similar relation, relying on a minimum of assumptions, was needed. Speculations along such lines lead to the alternative methods which will be described below. We shall return to the four-fifth law in the next section.

## Governing equations

Under normal circumstances water can be considered an incompressible fluid with uniform density (for simplicity we shall absorb  $\rho$  in the pressure term) governed by the Navier-Stokes equation (NSE)

$$a_i = -\frac{\partial P}{\partial x_i} + \nu \frac{\partial^2 v_i}{\partial x_j \partial x_j}, \quad (48)$$

where  $a_i = \frac{\partial v_i}{\partial t} + \frac{\partial v_j v_i}{\partial x_j}$  is the acceleration. Assuming constant density and incompressibility, mass conservation is expressed by

$$\frac{\partial v_j}{\partial x_j} = 0. \quad (49)$$

Real water is of course not incompressible, but we could never detect this at the Mach numbers encountered in the tank experiment. After filling the tank the water was circulated through the filter for three days in order to remove dust particles and bubbles. A convenient side-effect of this was the creation of nearly perfect thermal equilibrium, thus ruling out spatial variations of density and viscosity. For all practical purposes the governing equations can therefore be treated as 'first principles'.

## 5.1 Method 0 – using global homogeneity

From the NSE and the definition (41) of  $\langle \varepsilon \rangle$ , it readily follows that

$$\langle v_i a_i \rangle = -\langle \varepsilon \rangle - \frac{\partial}{\partial x_i} \langle v_i P \rangle + \nu \nabla^2 \frac{1}{2} \langle v^2 \rangle + \nu \frac{\partial^2}{\partial x_i \partial x_j} \langle v_i v_j \rangle \quad (50)$$

Since  $a_i$  is directly measurable the problem would be solved, if we could argue that the pressure transport term can be neglected. Global homogeneity would make the term vanish along with the terms containing  $\nu$ , and lead to the simple relation

$$\left\langle \frac{d}{dt} \frac{1}{2} v^2 \right\rangle = \langle \mathbf{v} \cdot \mathbf{a} \rangle = -\langle \varepsilon \rangle \quad (51)$$

Thus the mean kinetic energy of a particle should be a decreasing function time, which is, in fact, what we observe in the two-grid experiment. Figure 33 shows the mean kinetic energy of particles entering a central volume in the tank, with time measured from the moment each particle enters. The values of  $-\langle v_i a_i \rangle$  roughly agree with  $\langle \varepsilon \rangle$  obtained by other methods, indicating that pressure transport of kinetic energy is indeed small for two-grid turbulence. This may be linked to the fact that there is practically no mean flow, although we speculate if the lack of pressure transport of kinetic energy is a general feature. We refer to this as Method 0. The results are listed in Table 8.

It should be noted that the relation  $\langle \mathbf{v} \cdot \mathbf{a} \rangle = -\langle \varepsilon \rangle$  cannot possess general validity since it is not form-invariant under a Galilean transformation. For contracting or swirling flows, where the mean velocity is spatially varying, it could hold only for a specific choice of the co-ordinate system.

In order to justify  $\langle \mathbf{v} \cdot \mathbf{a} \rangle$  as a measure of the dissipation for a specific flow one would have to estimate the pressure term from data, which is not easily done. Since no technique is available for direct pressure measurements the inverse

Laplacian would have to be invoked in order to express the pressure in terms of velocities. This is problematic because it would involve estimates of slowly converging (perhaps not even converging) integrals over all space, whereas data is available only from a limited volume. Below we derive two additional methods, each of which circumvents these problems. The first is based on the assumption of (a weak form of) local homogeneity whereas the second relies solely on first principles.

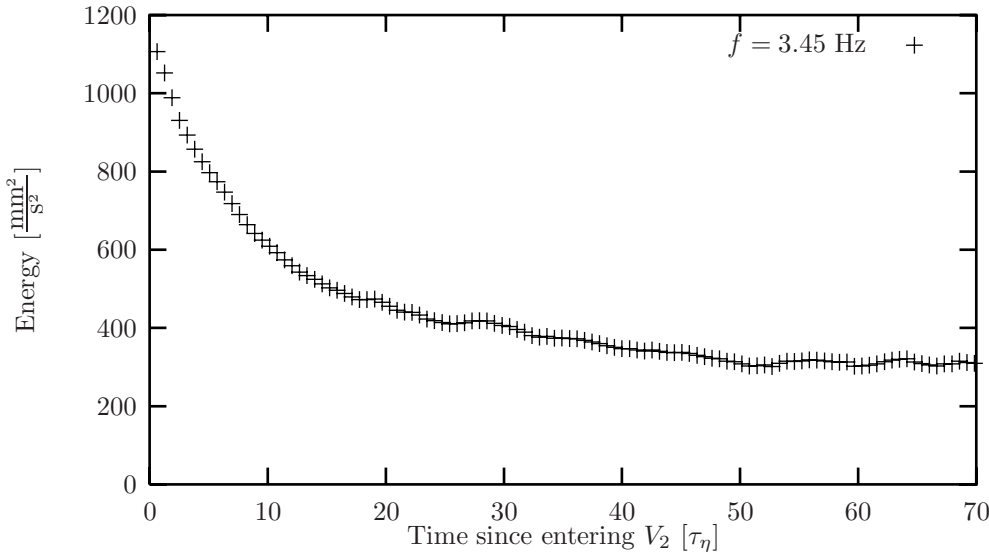


Figure 33. Decay of mean kinetic energy of particles entering a 90 mm thick horizontal slab in the middle of the tank. Time is counted from the moment each particle enters the slab and the average is over particles still within the slab.

## 5.2 Method 2 – using local homogeneity

From early days, symmetry has played an important role in turbulence theory. In his treatment of turbulent diffusion Taylor (1921) was perhaps the first to employ global homogeneity, isotropy and stationarity of turbulent flows. It is well known that grid generated turbulence to a fair degree of accuracy obeys these symmetries. The same can be said about decaying turbulence generated e.g. by towing a grid through a tank, although the symmetries are not perfectly satisfied for either type of flow, nor for any other real flow. Kolmogorov (1941b) introduced *local* symmetry which, loosely speaking, only regards the smaller scales of the turbulence. The obvious reason for making the weakest possible assumptions about symmetry is to enlarge the class of flows for which they are fulfilled, or at least fulfilled to an acceptable degree of approximation. At the same time, symmetry assumptions should be strong enough to enable us to derive non-trivial consequences from them. Local symmetry is weaker than the global symmetry since it applies only to statistics involving velocity increments. According to Frisch (1995) the modern view on turbulence is that all local symmetries are restored in the limit of infinite Reynolds numbers. Even if turbulence is produced at large scales in a highly non-symmetric way the small scale structure will, according to this view, tend to obey local symmetries at high Reynolds numbers, perhaps even in a universal way.

In the following we assume, besides incompressibility and uniform density, only local homogeneity, which is expected to be fulfilled in the bulk of the fluid away

from boundaries and points with peculiar properties. Local homogeneity lead Kolmogorov to some celebrated results: the two hypotheses (Kolmogorov 1941b) and the four-fifth law (Kolmogorov 1941a). The derivation of the four-fifth law and the related Monin (1959) equation have been reviewed lately by Lindborg (1996) and Hill (1997). According to both authors Monin's derivation is wrong, but they draw different conclusions regarding the applicability of local isotropy to demonstrate the vanishing of the correlation matrix  $\langle \delta v_i \delta \nabla_j P \rangle$ . Unfortunately this discussion is complicated by the fact that the authors use different definitions of local homogeneity. In order to avoid confusion, a precise definition of local homogeneity is stated below. It is equivalent to Yaglom's definition found on page 401 in Monin and Yaglom (1975). We note that this definition differs from Kolmogorov's (1941b) original definition as well as from Hill's (1997) 'operational calculus'. Following Monin and Yaglom (1975) no Reynolds decomposition is made, since the necessary high pass filtering should be ensured by the use of increments. In this respect the treatment differs from Lindborg (1996).

Local homogeneity will be defined in terms of a set of moving coordinate systems, which we will refer to as local coordinate systems. A local coordinate system is defined as a frame of reference whose origin follows the motion of one particular fluid particle. Thus if the flow field, as seen from the laboratory system, is denoted by  $v_i(\mathbf{x}, t)$  we define the local coordinates  $\mathbf{y}$  and the local time  $s$  by

$$\begin{aligned} y_i &= x_i - z_i(t) \\ s &= t \end{aligned} \tag{52}$$

where  $z_i(t)$  is a fluid particle trajectory so that

$$\frac{dz_i}{dt} = v_i(\mathbf{z}, t) \tag{53}$$

The connection between local and laboratory partial derivatives are as follows

$$\begin{aligned} \frac{\partial}{\partial y_i} &= \frac{\partial}{\partial x_i} \\ \frac{\partial}{\partial s} &= \frac{\partial}{\partial t} + v_j(\mathbf{z}, t) \frac{\partial}{\partial x_j} \end{aligned} \tag{54}$$

The velocity in the local coordinate system is denoted by  $\delta v_i$  and is defined as

$$\delta v_i(\mathbf{y}, s; \mathbf{z}) = v_i(\mathbf{z}(s) + \mathbf{y}, s) - v_i(\mathbf{z}(s), s) = v_i(\mathbf{x}, t) - v_i(\mathbf{z}(t), t) \tag{55}$$

The parameter  $\mathbf{z}$  in  $\delta \mathbf{v}(\mathbf{y}, s; \mathbf{z})$  is there to indicate that we are using the local system that passes through  $\mathbf{z}$  at time  $s$ . For the sake of brevity we will often omit it.

The acceleration in the local system is given by

$$\begin{aligned} \delta a_i(\mathbf{y}, s) &= \frac{\partial}{\partial s} \delta v_i + \frac{\partial}{\partial y_j} \delta v_j \delta v_i \\ &= a_i(\mathbf{x}, t) - a_i(\mathbf{z}, t) \end{aligned} \tag{56}$$

where  $a_i$  is the acceleration in the laboratory frame. The last identity follows from (54). It is interesting to note that this expresses  $\delta \mathbf{a}$  in terms of the local field  $\delta \mathbf{v}(\mathbf{y}, s)$  and derivatives of  $\delta \mathbf{v}(\mathbf{y}, s)$  with respect to  $s$  and  $\mathbf{y}$ . We shall refer to a quantity expressible in terms of  $\delta \mathbf{v}$  and derivatives of  $\delta \mathbf{v}(\mathbf{y}, s)$  with respect to  $s$  and  $\mathbf{y}$  as a *local quantity*. Note that it is not possible to express  $\delta \mathbf{a}$  in terms of  $\delta \mathbf{v}$  using partial derivatives of the laboratory coordinates  $t$  and  $\mathbf{x}$ , because the advection term will contain a factor  $\mathbf{v}$ .

Local homogeneity can be defined as homogeneity of all local quantities (with some geometric restrictions to be stated). In other words local homogeneity means that statistics formed from local quantities are independent of the local coordinate

system to which they refer. The geometric restrictions are 1) that only local coordinate systems having origins inside a specified domain (volume)  $V$  are considered and 2) that separations should be smaller than some upper bound, say  $|\mathbf{y}| < r_{\max}$ .

With this definition local homogeneity has no implications for other than statistics involving local quantities. It is therefore a weaker assumption than global homogeneity which claims translational invariance of all statistics. Our definition is essentially the same as that of Monin and Yaglom (1975) (used by e.g. Lindborg 1996) except slightly more explicit with respect to time derivatives. It is very much in the spirit of Kolmogorov's (1941b) original definition, where inertial systems co-moving with the flow at one space-time point are used to define local quantities. Kolmogorov also included stationarity in the definition of homogeneity, while we will keep stationarity as a separate concept. The 'operational calculus' of Hill (1997) implies translational invariance of statistics of quantities containing a factor in the form of an increment (e.g.  $\delta\mathbf{v}$  or  $\delta P$ ). Although a weaker assumption than global homogeneity, 'operational calculus' involves a larger class of statistics than our local quantities and is therefore a stronger assumption than we are making here.

Velocity gradients are local since they can be written as

$$\left\langle \frac{\partial v_i(\mathbf{x})}{\partial x_j} \right\rangle = \left\langle \frac{\partial(v_i(\mathbf{x}) - v_i(\mathbf{z}))}{\partial x_j} \right\rangle = \left\langle \frac{\partial \delta v_i}{\partial y_j} \right\rangle. \quad (57)$$

Here  $\mathbf{z}$  is arbitrary, so  $\left\langle \frac{\partial v_i(\mathbf{x})}{\partial x_j} \right\rangle$  must be a global constant  $A_{ij}$  independent of  $\mathbf{x}$ , and the mean flow must be of the linear form

$$\langle v_i(\mathbf{x}) \rangle = A_{ij}(x_j - x_j^0) \quad (58)$$

or

$$\langle \delta v_i(\mathbf{y}) \rangle = A_{ij} y_j. \quad (59)$$

In globally homogeneous flows only constant mean flows are possible. Local homogeneity, the way it is defined here, extends the repertoire of mean flows one step further allowing less trivial mean flows such as rigid rotations ( $A_{ij}$  skew-symmetric), linear contractions ( $A_{ij}$  symmetric), linear shear flows etc. A rigid rotation has an axis, and a converging-diverging flow may have a stagnation point. The existence of special points in absolute space violates global translational invariance, but local homogeneity is *not* violated because an axis of rotation or a stagnation point cannot be determined from the local velocity field  $\delta\mathbf{v}$ .

Transforming the NSE to a local coordinate system we find

$$\frac{\partial}{\partial s} \delta v_i + \frac{\partial}{\partial y_j} \delta v_j \delta v_i = -\frac{\partial}{\partial y_i} \tilde{P} + \nu \frac{\partial^2}{\partial y_j \partial y_j} \delta v_i + \delta f_i \quad (60)$$

where  $\tilde{P} = \delta P + y_j a_j(\mathbf{z}) - y_j f_j(\mathbf{z})$  and  $\delta P = P(\mathbf{z} + \mathbf{y}) - P(\mathbf{z})$ ,  $f$  being an external force. Thus we regain the NSE, now with  $\tilde{P}$  playing the part of the pressure. Since incompressibility also holds in local coordinates it appears that the governing equations are unchanged. As far as fluid dynamics is concerned, there is therefore no difference between local systems and inertial systems, but the local systems have a no-slip condition at the origin, i.e.  $\delta\mathbf{v}(0) = 0$ . In the absence of external forces the only way  $\delta\mathbf{v}$  can develop differently in different local systems is through the boundary conditions for  $\delta\mathbf{v}$  at  $|\mathbf{y}| \rightarrow \infty$ , which may depend slightly on the location of the origin. The fact that a local system moves around quite randomly makes it plausible to assume that its past is not heavily biased by the particular location of the origin at some instant in time, so that all these systems have equivalent statistical properties.

Equation (60) can also be written as

$$\delta a_i = -\delta \nabla_i P + \nu \delta \nabla^2 v_i + \delta f_i, \quad (61)$$

where

$$\delta \nabla_i P = \nabla_i P(\mathbf{y} + \mathbf{z}) - \nabla_i P(\mathbf{z}) = \frac{\partial \delta P}{\partial z_i} \quad (62)$$

and

$$\delta \nabla^2 v_i = \frac{\partial^2 \delta v_i}{\partial z_j \partial z_j} = \frac{\partial^2 \delta v_i}{\partial y_j \partial y_j} - \frac{\partial^2 \delta v_i}{\partial y_j \partial y_j} \Big|_{\mathbf{y}=0}. \quad (63)$$

Here the viscous term is evidently local.

We will assume that the external force increment  $\delta f_i$  is statistically homogeneous so that it can be treated as a local quantity. In many cases of interest, including the two grid flow, there is no external force  $\mathbf{f}$  and the condition is trivially fulfilled. In other cases the forcing acts on large scales so that  $\delta \mathbf{f}$  is small for small enough separations and can be neglected. We drop  $\delta \mathbf{f}$  in the following.

The pressure gradient term  $\delta \nabla_i P$  is therefore local, because all the other terms in (61) are local. This does not necessarily mean that the pressure increment  $\delta P = P(\mathbf{z} + \mathbf{y}) - P(\mathbf{z})$  is local, although both  $\tilde{P}$  and  $\int \delta \nabla_i P dy_i = \delta P - \mathbf{y} \cdot \nabla P(\mathbf{z})$  are. It might be argued that the formal solution to the Poisson equation

$$\delta P = \int \left( \frac{1}{4\pi|\mathbf{y} - \mathbf{y}'|} - \frac{1}{4\pi|\mathbf{y}'|} \right) \frac{\partial \delta v_k(\mathbf{y}')}{\partial y'_j} \frac{\partial \delta v_j(\mathbf{y}')}{\partial y'_k} d^3 y' \quad (64)$$

is a local expression, but, apart from the possible divergence of the integral, the integration extends over infinitely large separations which may not be allowed. Postulating locality of  $\delta P$  is therefore an additional assumption. Locality of  $\delta P$  is assumed by e.g. Monin (1959), Monin and Yaglom (1975) and Hill (1997) and it is possibly justified for a number of flows. However, a simple rigid rotation  $v_i(x) = \epsilon_{ijk} \Omega_j x_k$  is an example of a locally homogeneous flow for which  $\delta P$  is not local. According to the alternative definitions of local homogeneity (Hill's as well as Kolmogorov's) rigid rotations are not locally homogeneous. We note that (60) implies that  $\tilde{P}$  is local (when  $\delta \mathbf{f}$  is local). Therefore  $\mathbf{a}$  is local when  $\delta P$  is local. Within the operational calculus definition (Hill 1997) of local quantities this further implies that  $v_i(\mathbf{x}, t + \tau) - v_i(\mathbf{x}, t)$  is local. We note this because such an assumption is needed for interpretation of hot-wire data.

It is natural to define *local stationarity* as meaning stationarity in the local coordinate system, i.e. that  $\left\langle \frac{\partial Q}{\partial s} \right\rangle = 0$  for any local quantity  $Q$ . For a local quantity  $Q$  made from simultaneous velocity increments of the form  $\delta \mathbf{v}(\mathbf{y}_p, s; \mathbf{z})$  (all with the same  $s$ ) we have

$$\left\langle \frac{\partial Q}{\partial s} \right\rangle = \left\langle \frac{\partial Q}{\partial t} \right\rangle + \frac{\partial}{\partial z_j} \langle v_j(\mathbf{z}, t) Q \rangle. \quad (65)$$

Global stationarity means that the first term  $\left\langle \frac{\partial Q}{\partial t} \right\rangle$  vanishes. The second term involves the non-local quantity  $v_j(\mathbf{z}, t) Q$ , and hence local homogeneity allows the gradient  $\partial/\partial z_j \langle v_j(\mathbf{z}, t) Q \rangle$  to be non-zero. Therefore *local stationarity* is distinct from *global stationarity*, and one should not be tempted to believe that global stationarity implies local stationarity. Within the framework of operational calculus  $\partial/\partial z_j \langle v_j(\mathbf{z}, t) Q \rangle = 0$ , because  $v_j(\mathbf{z}, t) Q$  contains a local factor ( $Q$ ). Therefore operational calculus does not distinguish between local and global stationarity. The same is true when *global homogeneity* is assumed.

*Local isotropy* can be defined in a similar fashion as invariance of the statistical properties of the local velocity field  $\delta \mathbf{v}$  under rotations of the local coordinate

system around the origin (inside  $V$  and for small enough separations). Isotropy is a powerful symmetry that greatly simplifies the mathematics of turbulence. In the following we shall try to proceed without it.

### Relations for local homogeneity

Consider the vector field  $\delta q(\mathbf{y}) = q(\mathbf{y} + \mathbf{z}) - q(\mathbf{z})$  which happens to be a local quantity, for example  $q = a_i$ . For such a quantity we have the following trivial identities

$$\frac{\partial}{\partial y_i} \delta q(\mathbf{y}) = \frac{\partial}{\partial y_i} q(\mathbf{y} + \mathbf{z}), \quad (66)$$

$$\left( \frac{\partial}{\partial y_i} - \frac{\partial}{\partial z_i} \right) \delta q(\mathbf{y}) = \frac{\partial}{\partial z_i} q(\mathbf{z}), \quad (67)$$

$$\frac{\partial}{\partial z_j} \frac{\partial}{\partial y_i} \delta q(\mathbf{y}) = \frac{\partial}{\partial z_i} \frac{\partial}{\partial y_j} \delta q(\mathbf{y}), \quad (68)$$

$$\frac{\partial}{\partial y_j} \left( \frac{\partial}{\partial y_i} - \frac{\partial}{\partial z_i} \right) \delta q(\mathbf{y}) = 0. \quad (69)$$

Below we make frequent use of these identities.

Now define the quantity

$$Q(\mathbf{y}', \mathbf{y}) \equiv \left\langle \delta v_k(\mathbf{y}') \frac{\partial}{\partial y_k} \delta q(\mathbf{y}) \right\rangle. \quad (70)$$

Assuming local homogeneity it follows that

$$\begin{aligned} Q(\mathbf{y}', \mathbf{y}) &= \left\langle \delta v_k(\mathbf{y}') \frac{\partial \delta q(\mathbf{y})}{\partial y_k} \right\rangle = \frac{\partial}{\partial y_k} \langle \delta v_k(\mathbf{y}') \delta q(\mathbf{y}) \rangle \\ &= \left( \frac{\partial}{\partial y_k} - \frac{\partial}{\partial z_k} \right) \langle \delta v_k(\mathbf{y}') \delta q(\mathbf{y}) \rangle = Q(\mathbf{y}', 0), \end{aligned} \quad (71)$$

so that  $Q(\mathbf{y}', \mathbf{y})$  is independent of  $\mathbf{y}$ . We also have

$$\frac{\partial}{\partial y'_j} Q(\mathbf{y}', \mathbf{y}) = \left( \frac{\partial}{\partial y'_j} + \frac{\partial}{\partial y_j} - \frac{\partial}{\partial z_j} \right) Q(\mathbf{y}', \mathbf{y}) = \left\langle \frac{\partial v_k(\mathbf{z})}{\partial z_j} \frac{\partial \delta q(\mathbf{y})}{\partial y_k} \right\rangle, \quad (72)$$

where the right hand side is independent of both  $\mathbf{y}, \mathbf{y}'$  and  $\mathbf{z}$ . Integrating both sides we therefore get

$$\left\langle \delta v_k(\mathbf{y}') \frac{\partial \delta q(\mathbf{y})}{\partial y_k} \right\rangle = y'_j \left\langle \frac{\partial v_k(\mathbf{z})}{\partial z_j} \frac{\partial q(\mathbf{x})}{\partial x_k} \right\rangle \quad (73)$$

where  $\mathbf{z}$  and  $\mathbf{x}$  are arbitrary (within the geometric constraints). If the gradients of  $q$  and  $\mathbf{v}$  become uncorrelated for large separations we get

$$\left\langle \frac{\partial v_k(\mathbf{z})}{\partial z_j} \frac{\partial q(\mathbf{x})}{\partial x_k} \right\rangle \approx \left\langle \frac{\partial v_k(\mathbf{x})}{\partial z_j} \right\rangle \left\langle \frac{\partial q(\mathbf{x})}{\partial x_k} \right\rangle. \quad (74)$$

When  $\langle \mathbf{v} \rangle$  is constant follows that  $Q = 0$ . However, in order to arrive at this conclusion, it has to be assumed that local homogeneity works for large separations, several integral length scales, say.

Setting  $q = \delta v_i$  we find that

$$\left\langle \delta v_k(\mathbf{y}') \frac{\partial \delta v_i(\mathbf{y})}{\partial y_k} \right\rangle = G_{ij} y'_j, \quad (75)$$

where

$$G_{ij} = \left\langle \frac{\partial v_k(\mathbf{x}')}{\partial x'_j} \frac{\partial v_i(\mathbf{x})}{\partial x_k} \right\rangle \quad (76)$$

is a constant even if  $\mathbf{x}$  and  $\mathbf{x}'$  are arbitrary. We note that  $\nu G_{ii}$  is the 'rotational' part of the energy dissipation, which is most often assumed to be negligible. We find that  $\frac{\nu G_{ii}}{\varepsilon} < 0.01$  in agreement with recent detailed measurements by Antonia et al. (1998). When we set  $\mathbf{y} = \mathbf{y}'$  in (75), multiply on both sides by  $y_i$  and integrate over the sphere  $|\mathbf{y}| = r$ , we find

$$\frac{1}{3} G_{ii} r^2 = r \frac{\partial B_{dd}}{\partial r} + 3B_{dd} - B_{ii}. \quad (77)$$

With  $G_{ii} = 0$  this relation is well known for homogeneous, isotropic turbulence<sup>12</sup>.

Setting  $q = a_i$  we find

$$\left\langle \delta v_k(\mathbf{y}') \frac{\partial \delta a_i(\mathbf{y})}{\partial y_k} \right\rangle = F_{ij} y'_j, \quad (78)$$

where the tensor

$$F_{ij} \equiv \left\langle \frac{\partial v_k(\mathbf{z})}{\partial z_j} \frac{\partial a_i(\mathbf{x})}{\partial x_k} \right\rangle \quad (79)$$

is a another constant of the flow. We have used this relation to estimate  $F_{ij}$  for the nine experiments mentioned earlier. We find that the components are small with fairly unsystematic values. The trace  $F_{ii}$  is always found to be negative with values ranging from  $-10^{-1} \text{s}^{-3}$  to  $-10^{-2} \text{s}^{-3}$ . These results are probably consistent with  $F_{ij} = 0$  within the experimental scatter indicating  $|F_{ii}| < 10^{-1} \text{s}^{-3}$ .

The trace of  $F_{ij}$  can be written as

$$F_{ii} = \frac{1}{2} \frac{\partial G_{ii}}{\partial s} + \frac{1}{2} \frac{\partial^3 \langle \delta v_i \delta v_j \delta v_k \rangle}{\partial y_i \partial y_j \partial y_k} \quad (80)$$

If  $F_{ii} = 0$  and  $\partial/\partial s G_{ii} = 0$ , e.g. assuming local stationarity, this equation reduces to a corresponding equation of Hill (1997) derived using operational calculus. When both sides of (80) are integrated over a ball of radius  $r$  a few integrations by part yield the relation

$$\frac{4\pi}{3} r^3 \left( 2F_{ii} - \frac{\partial G_{ii}}{\partial s} \right) = \frac{4\pi}{r} \frac{\partial}{\partial r} \left( \frac{1}{r} \frac{\partial}{\partial r} r^4 B_{ddd} - 3r^2 B_{dii} \right) \quad (81)$$

or

$$\frac{r^3}{15} \left( 2F_{ii} - \frac{\partial G_{ii}}{\partial s} \right) = r \frac{\partial B_{ddd}}{\partial r} + 4B_{ddd} - 3B_{dii} \quad (82)$$

If the left hand side is set equal to zero the relation is well known for homogeneous, isotropic turbulence (e.g. Monin and Yaglom 1975). We only used local homogeneity and the definitions (42) – (45). It is noted that if we define  $G_{ii} \equiv \frac{3}{4\pi r^3} \int_{|\mathbf{y}| < r} \left\langle \frac{\partial \delta a_i}{\partial y_i} \right\rangle d^3 y$  and  $F_{ii} \equiv \frac{3}{4\pi r^3} \int_{|\mathbf{y}| < r} \left\langle \frac{\partial^2 \delta v_i \delta a_j}{\partial y_i \partial y_j} \right\rangle d^3 y$  the relation is exact. The main implication of local homogeneity is therefore that  $G_{ii}$  and  $F_{ii}$  are constants of the flow.

## Method 2

Using the NSE the acceleration gradient can be written as

$$\begin{aligned} \frac{\partial \delta a_i}{\partial y_k} &= \frac{\partial}{\partial y_k} \left( -\frac{\partial \delta P}{\partial z_i} + \nu \frac{\partial^2 \delta v_i}{\partial z_p \partial z_p} \right) \\ &= \frac{\partial}{\partial y_i} \left( \delta a_k - \nu \frac{\partial^2 \delta v_k}{\partial z_p \partial z_p} \right) + \frac{\partial}{\partial z_k} \nu \frac{\partial^2 \delta v_i}{\partial y_p \partial y_p} \end{aligned} \quad (83)$$

<sup>12</sup>If we define  $G_{ii} \equiv \frac{3}{4\pi r^3} \int_{|\mathbf{y}| < r} \left\langle \frac{\partial \delta a_i}{\partial y_i} \right\rangle d^3 y$  the relation becomes exact.

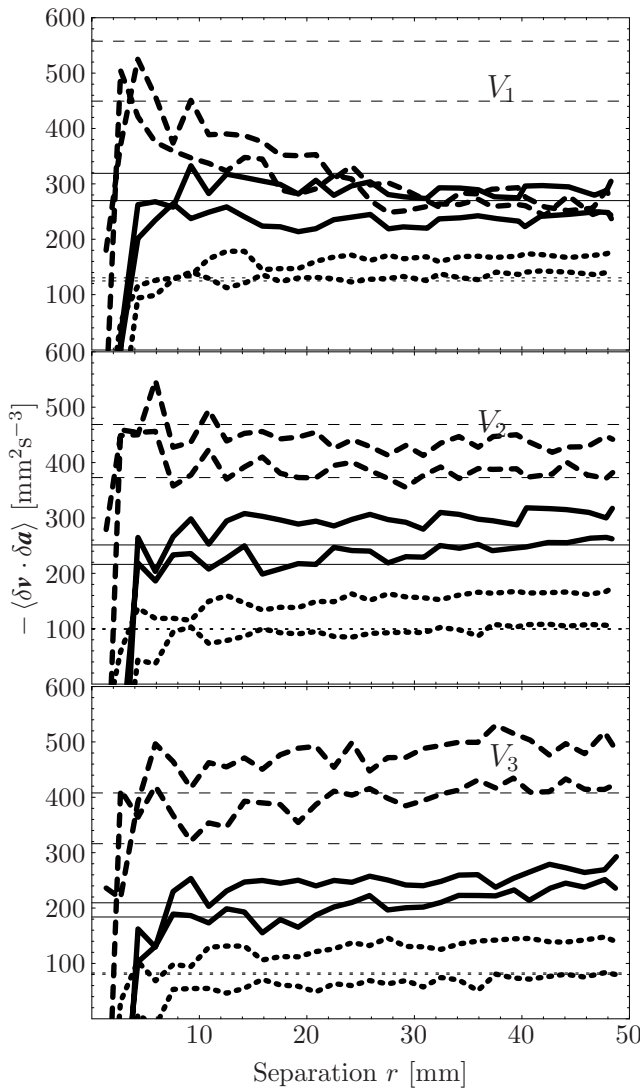


Figure 34. The structure function  $\langle \delta \mathbf{v} \cdot \delta \mathbf{a} \rangle$  averaged over the volumes  $V_1$ ,  $V_2$  and  $V_3$ . The short dashed curves are the 2 Hz runs, the solid 3 Hz, and the dashed 3.5 Hz. The horizontal lines are values of  $2\varepsilon$  derived by fitting of the second order velocity structure function calculated in the corresponding volume  $V_1$ ,  $V_2$  or  $V_3$  as described in section 4.4, using  $C_K = 2.0$ .

Hence

$$\begin{aligned}
 F_{ij} y'_j &= \frac{\partial}{\partial y_i} \left\langle \delta v_k(\mathbf{y}') \delta a_k(\mathbf{y}) - \nu \delta v_k(\mathbf{y}') \frac{\partial^2 \delta v_k(\mathbf{y})}{\partial z_p \partial z_p} \right\rangle + \nu \frac{\partial}{\partial z_k} \left\langle \delta v_k(\mathbf{y}') \frac{\partial^2 \delta v_i(\mathbf{y})}{\partial y_p \partial y_p} \right\rangle \\
 &= \frac{\partial}{\partial y_i} \left\langle \delta v_k(\mathbf{y}') \delta a_k(\mathbf{y}) + \nu \frac{\partial \delta v_k(\mathbf{y}')}{\partial z_p} \frac{\partial \delta v_k(\mathbf{y})}{\partial z_p} \right\rangle \quad (84)
 \end{aligned}$$

Integrating both sides we get

$$F_{ij} y_i y'_j = \langle \delta v_k(\mathbf{y}') \delta a_k(\mathbf{y}) \rangle + \nu \left\langle \frac{\partial \delta v_k(\mathbf{y}')}{\partial z_p} \frac{\partial \delta v_k(\mathbf{y})}{\partial z_p} \right\rangle. \quad (85)$$

In this equation the viscous term can be written as

$$\begin{aligned}
 &\nu \left\langle \frac{\partial \delta v_k(\mathbf{y}')}{\partial z_p} \frac{\partial \delta v_k(\mathbf{y})}{\partial z_p} \right\rangle \\
 &= \langle \varepsilon \rangle - \nu G_{ii} - \nu \left( \frac{\partial}{\partial y'_p} \frac{\partial}{\partial y_p} + \frac{\partial}{\partial y'_p} \frac{\partial}{\partial y'_p} + \frac{\partial}{\partial y_p} \frac{\partial}{\partial y_p} \right) \langle \delta v_k(\mathbf{y}') \delta v_k(\mathbf{y}) \rangle. \quad (86)
 \end{aligned}$$

When  $|\mathbf{y} - \mathbf{y}'|$  is large (compared to the Kolmogorov scale) the last term can be neglected. If furthermore  $G_{ii}$  is small we conclude with the simple relation

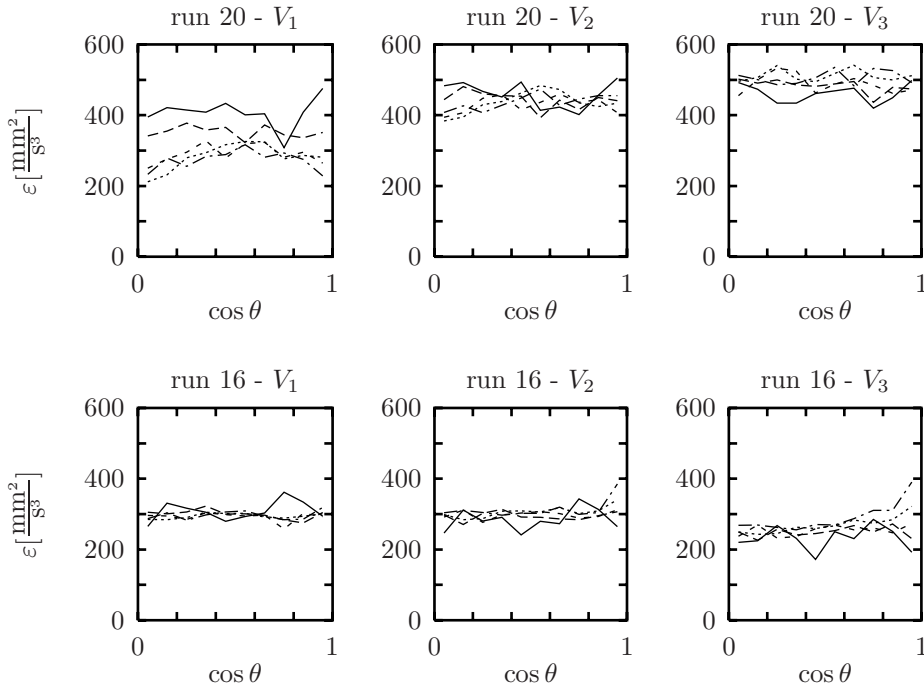


Figure 35. The (lack of) angular dependence of  $\langle \delta \mathbf{v} \cdot \delta \mathbf{a} \rangle$  for two runs. The five curves on each plot are for  $r = 10, 20, 30, 40$  and  $50$  mm.

$$\langle \delta v_k(\mathbf{y}') \delta a_k(\mathbf{y}) \rangle = -\langle \varepsilon \rangle + F_{ij} y_i y_j'. \quad (87)$$

When  $\mathbf{y}' = \mathbf{y}$  the viscous term becomes

$$\nu \left\langle \frac{\partial \delta v_k(\mathbf{y})}{\partial z_p} \frac{\partial \delta v_k(\mathbf{y})}{\partial z_p} \right\rangle = 2 \langle \varepsilon \rangle - 2\nu G_{ii} - \nu \frac{\partial}{\partial y_p} \frac{\partial}{\partial y_p} \langle \delta v_k(\mathbf{y}) \delta v_k(\mathbf{y}) \rangle \quad (88)$$

and (85) becomes

$$F_{ij} y_i y_j = \langle \delta v_k(\mathbf{y}) \delta a_k(\mathbf{y}) \rangle + 2 \langle \varepsilon \rangle - 2\nu G_{ii} - \nu \frac{\partial}{\partial y_p} \frac{\partial}{\partial y_p} \langle \delta v_k(\mathbf{y}) \delta v_k(\mathbf{y}) \rangle. \quad (89)$$

Neglecting the small viscous terms we get the following very simple relation

$$\langle \delta \mathbf{v}(\mathbf{y}) \cdot \delta \mathbf{a}(\mathbf{y}) \rangle = -2 \langle \varepsilon \rangle + F_{ij} y_i y_j \quad (90)$$

Finally we average over all directions of the separation to get

$$\frac{1}{4\pi r^2} \int_{|\mathbf{y}|=r} \langle \delta \mathbf{v}(\mathbf{y}) \cdot \delta \mathbf{a}(\mathbf{y}) \rangle d^2 y = -2 \varepsilon + \frac{r^2}{3} F_{ii} \quad (91)$$

Although somewhat uncertain, our estimates of  $F_{ii}$  indicate that the last term contributes less than 10% for separations of 25 mm.

We note that (90) implies isotropy of  $\langle \delta \mathbf{v}(\mathbf{y}) \cdot \delta \mathbf{a}(\mathbf{y}) \rangle$  for sufficiently small separations. This has been obtained without actually assuming isotropy. The same is true for  $\langle \delta \mathbf{v}(\mathbf{y}') \cdot \delta \mathbf{a}(\mathbf{y}) \rangle$  in (87). We also note that the only limitation for large separations is that local homogeneity should be valid. Therefore the relation should still hold for large separations outside the inertial range, provided that local homogeneity holds.

The dependence on separation have been investigated experimentally. In figure 34 values of  $-\delta\mathbf{v}(\mathbf{y}) \cdot \delta\mathbf{a}(\mathbf{y})$  averaged over shells  $r < |\mathbf{y}| < r + dr$  are shown for the three domains  $V_1$ ,  $V_2$  and  $V_3$  defined at the end of this section in (106). Three different grid frequencies were used. Generally the curves become rather flat for separations larger than  $\sim 10$  mm. However, the two curves at the top for the largest domain ( $V_1$ ) and the largest frequency (3.5 Hz) are clearly decreasing. Local homogeneity can be expected to break down for large domains, but we have no explanation for this to be more severe for the largest grid frequency. It could reflect a Reynolds number dependence of the flow in the vicinity of the grids, or it may simply have to do with mechanical deformations of the grids at larger frequencies. For the remaining curves the plateau values are in fair agreement with the values of  $2\varepsilon$  obtained from second order structure functions using  $C_K = 2$  (horizontal lines on the plots). It therefore seems that  $F_{ii} \sim 0$ .

If  $F_{ii} = 0$  equation (90) implies that  $\langle\delta\mathbf{v}(\mathbf{y}) \cdot \delta\mathbf{a}(\mathbf{y})\rangle$  is independent of direction. In order to check this experimentally  $\langle\delta\mathbf{v}(\mathbf{y}) \cdot \delta\mathbf{a}(\mathbf{y})\rangle$  was sampled as a function of  $|\mathbf{y}|$  and  $\cos\theta \equiv y_3/|\mathbf{y}|$ , where  $y_3$  is the vertical component of the separation. We call this quantity  $\langle\delta\mathbf{v}(r; \cos\theta) \cdot \delta\mathbf{a}(r; \cos\theta)\rangle$ . From (90) it follows that

$$\langle\delta\mathbf{v}(r; \cos\theta) \cdot \delta\mathbf{a}(r; \cos\theta)\rangle = -2\langle\varepsilon\rangle + r^2(a + b\cos^2\theta), \quad (92)$$

where

$$a = \frac{1}{2}(F_{11} + F_{22}) \quad (93)$$

and

$$b = F_{33} - \frac{1}{2}(F_{11} + F_{22}). \quad (94)$$

Figure 35 shows  $\langle\delta\mathbf{v}(r; \cos\theta) \cdot \delta\mathbf{a}(r; \cos\theta)\rangle$  for  $r$  ranging between 10 mm and 50 mm. Even if there is some scatter the independence of the direction is quite clear. This is true even for Run 20, one of the cases where  $\langle\delta\mathbf{v} \cdot \delta\mathbf{a}\rangle$  does not level off (top of figure 34). The dissipation can be obtained from best fits of the three parameters  $\langle\varepsilon\rangle$ ,  $a$  and  $b$  to all the data. This constitutes Method 2. Results are listed in Table 8.

Since there is little angular dependence we have  $b \sim 0$  and the cases where  $\langle\delta\mathbf{v} \cdot \delta\mathbf{a}\rangle$  varies with separation are fixed by the constant  $a$ . The question is whether  $a$  determined by such a fit has anything to do with  $F_{ij}$ . It probably has not because the estimated values of  $a$  far exceed the limit found on the magnitude of  $F_{ij}$ . We therefore interpret the results as a confirmation that  $F_{ij} = 0$  for the two-grid flow, and that local homogeneity does not work for the largest volume  $V_1$ .

To our knowledge (90) has not been published before, nor has the simplified version (91) with or without the  $F_{ii}$  term. We speculate that not much attention is given to fluid dynamic formulae containing accelerations, since traditionally accelerations have been difficult to measure. Equation (91) can be used to derive the four-fifth law, so we believe it has been deduced many times before, at least on the basis of stronger symmetry assumptions. For example it is trivial for globally homogeneous turbulence. The fact that it can be derived from rather weak assumptions makes it useful when the acceleration  $\mathbf{a}$  can be measured.

### 5.3 Method 3 – using global stationarity

The experimental results presented above test predictions based on local homogeneity. Although there is some support for local homogeneity for the smaller test domains  $V_2$  and  $V_3$ , it does not seem to work for the largest domain  $V_1$ . The results of Method 1 yield different values of  $\langle\varepsilon\rangle$  for the three volumes (see table

8). The values are consistently larger for larger volumes. This contradicts local homogeneity, because local homogeneity forbids spatial variations of  $\langle \varepsilon \rangle$ . Relying on local homogeneity for the experimental determination of  $\langle \varepsilon \rangle$  is therefore not satisfactory, and a the third method, based on global stationarity and first principles, was developed. The derivation goes as follows. In order to eliminate the pressure we rewrite the NSE differentiated in the form

$$\frac{\partial}{\partial y_j} (a_i(\mathbf{x} + \mathbf{y}) - \nu \nabla^2 v_i(\mathbf{x} + \mathbf{y})) = \frac{\partial}{\partial y_i} (a_j(\mathbf{x} + \mathbf{y}) - \nu \nabla^2 v_j(\mathbf{x} + \mathbf{y})). \quad (95)$$

For reasons soon to become clear the argument  $\mathbf{x} + \mathbf{y}$  is used rather than  $\mathbf{x}$ . Next step is to contract both sides of the equation with  $y_j$  and integrate over a ball of radius  $r$  centered at  $\mathbf{x}$ . This yields

$$\begin{aligned} & \int_{|\mathbf{y}| < r} y_j \frac{\partial}{\partial y_j} (a_i(\mathbf{x} + \mathbf{y}) - \nu \nabla^2 v_i(\mathbf{x} + \mathbf{y})) \, d^3 y \\ &= \int_{|\mathbf{y}| < r} y_j \frac{\partial}{\partial y_i} (a_j(\mathbf{x} + \mathbf{y}) - \nu \nabla^2 v_j(\mathbf{x} + \mathbf{y})) \, d^3 y \end{aligned} \quad (96)$$

The left hand side of (96) can be rewritten as

$$\begin{aligned} & \int_{|\mathbf{y}| < r} y_j \frac{\partial}{\partial y_j} (a_i(\mathbf{x} + \mathbf{y}) - \nu \nabla^2 v_i(\mathbf{x} + \mathbf{y})) \, d^3 y \\ &= r^4 \frac{\partial}{\partial r} \left[ r^{-3} \int_{|\mathbf{y}| < r} (a_i(\mathbf{x} + \mathbf{y}) - \nu \nabla^2 v_i(\mathbf{x} + \mathbf{y})) \, d^3 y \right] \end{aligned} \quad (97)$$

and the right hand side of (96) can be rewritten as

$$\int_{|\mathbf{y}| < r} y_j \frac{\partial}{\partial y_i} (a_j(\mathbf{x} + \mathbf{y}) - \nu \nabla^2 v_j(\mathbf{x} + \mathbf{y})) \, d^3 y = \frac{\partial}{\partial x_i} \int_{|\mathbf{y}| < r} y_j a_j(\mathbf{x} + \mathbf{y}) \, d^3 y \quad (98)$$

Hence (96) is equivalent to

$$\begin{aligned} & \frac{3}{4\pi r^3} \int_{|\mathbf{y}| < r} (a_i(\mathbf{x} + \mathbf{y}) - \nu \nabla^2 v_i(\mathbf{x} + \mathbf{y})) \, d^3 y - a_i(\mathbf{x}) + \nu \nabla^2 v_i(\mathbf{x}) \\ &= \frac{\partial}{\partial x_i} \int_0^r \frac{3}{4\pi r'^4} \left[ \int_{|\mathbf{y}| < r'} y_j a_j(\mathbf{x} + \mathbf{y}) \, d^3 y \right] \, dr' \end{aligned} \quad (99)$$

This form of the NSE is interesting because the pressure has been eliminated without having to pay for it with an integration over an infinite volume.

The next step is to contract both sides of this equation with  $v_i(\mathbf{x})$ , integrate over a test volume and take the ensemble average, but first we note that<sup>13</sup>

$$\left\langle v_i(\mathbf{x}) \frac{\partial}{\partial x_i} a_j(\mathbf{x} + \mathbf{y}) \right\rangle = \left\langle \frac{\partial}{\partial s} a_j(\mathbf{x} + \mathbf{y}) \right\rangle \quad (100)$$

We also need the relation

$$\nu v_i \nabla^2 v_i = -\varepsilon + \nu \nabla^2 \frac{1}{2} v^2 + \nu \frac{\partial^2}{\partial x_i \partial x_j} v_i v_j \quad (101)$$

---

<sup>13</sup>This is where we use global stationarity.

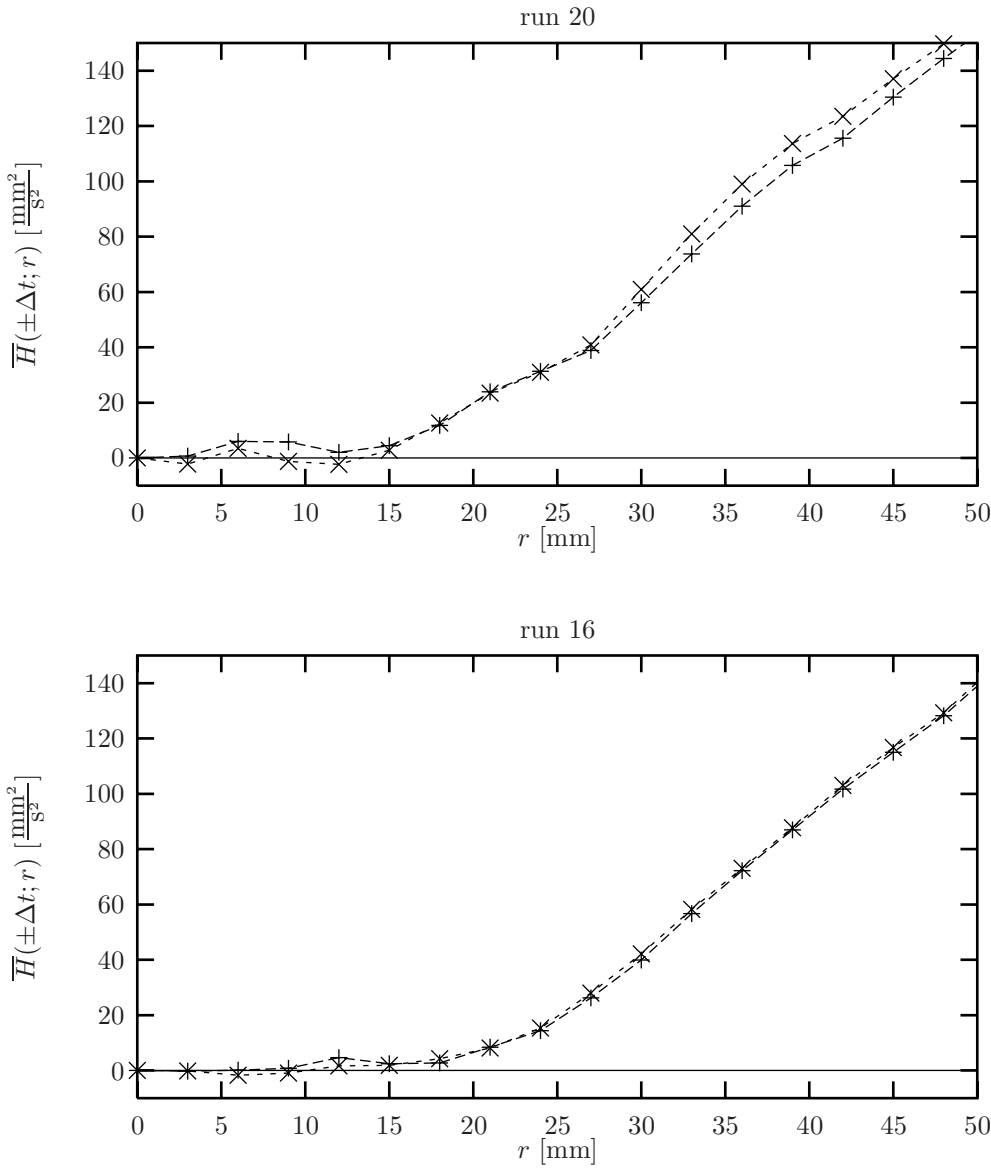


Figure 36. Examples of  $\overline{H}(\pm\Delta t; r)$ . The other runs are very similar. Crosses are for  $+\Delta t$  and pluses for  $-\Delta t$ .

and make the following definitions

$$U_i(\mathbf{x}; r) = \frac{3}{4\pi r^3} \int_{|\mathbf{y}| < r} v_i(\mathbf{x} + \mathbf{y}) d^3y \quad (102)$$

$$A_i(\mathbf{x}; r) = \frac{3}{4\pi r^3} \int_{|\mathbf{y}| < r} a_i(\mathbf{x} + \mathbf{y}) d^3y \quad (103)$$

$$H(\mathbf{x}, t; r) = \frac{3}{4\pi r^3} \int_{|\mathbf{y}| < r} a_j(\mathbf{x} + \mathbf{y}, t) y_j d^3y, \quad (104)$$

With this it follows that

$$\langle v_i(\mathbf{x}) A_i(\mathbf{x}; r) \rangle - \langle v_i(\mathbf{x}) a_i(\mathbf{x}) \rangle - \langle \varepsilon(\mathbf{x}) \rangle$$

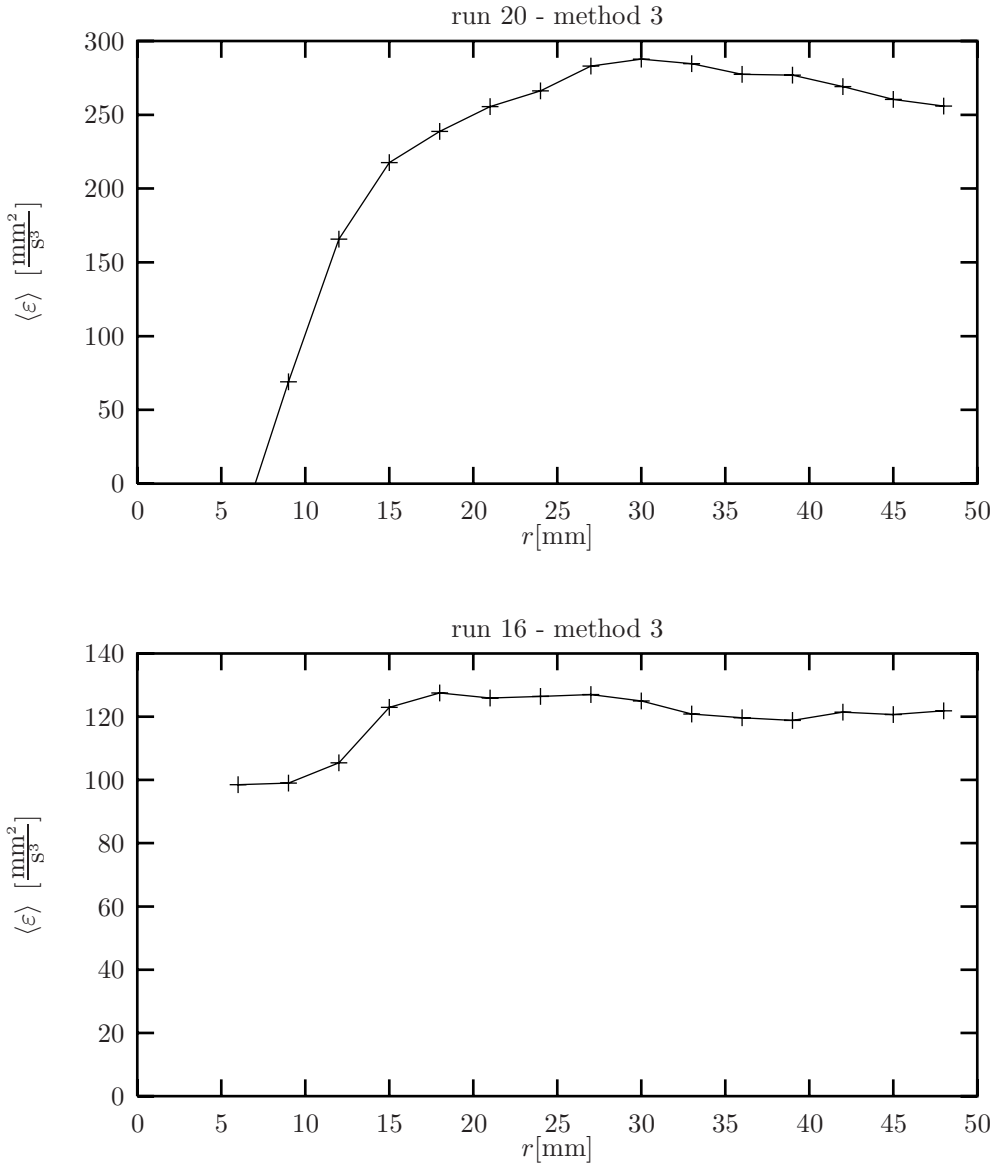


Figure 37. Energy dissipation results for Method 3.

$$\begin{aligned}
& -\frac{\nu}{r^4} \frac{\partial}{\partial r} r^4 \frac{\partial}{\partial r} \langle v_i(\mathbf{x}) U_i(\mathbf{x}; r) \rangle + \nu \nabla^2 \frac{1}{2} \langle v(\mathbf{x})^2 \rangle + \nu \frac{\partial^2}{\partial x_i \partial x_j} \langle v_i v_j \rangle \\
& = \left\langle \int_0^r \frac{1}{r'} \frac{\partial}{\partial s} \frac{1}{V} \int_{V(s)} H(\mathbf{x}(s), s, r') d^3 x(s) dr' \right\rangle \quad (105)
\end{aligned}$$

where  $V$  is the test volume. The differentiation with respect to  $s$  is a local derivative, i.e. it should be done in a local frame of reference following  $\mathbf{x}(s)$ . The flow is volume preserving, so averaging over  $V(s)$  is actually straight forward. Each particle located at a position  $\mathbf{x}(s)$  inside  $V$  at time  $s$  is followed one step forward in time and the average of  $a_j(\mathbf{x}(s + \Delta t) + \mathbf{y}, s + \Delta t) y_j$  over all particles within a distance  $r$  of  $\mathbf{x}(s + \Delta t)$  is calculated<sup>14</sup>. This is repeated for all  $s$  and an ensemble average,  $\overline{H}(+\Delta t; r)$ , is formed. In a similar way  $\overline{H}(-\Delta t; r)$  is calculated by going

<sup>14</sup>It does not matter if  $\mathbf{x}(s)$  leaves  $V$ .

one time step backwards. Finally  $\langle \partial/\partial s V^{-1} \int_{V(s)} H(\mathbf{x}, s; r) d^3x \rangle$  is estimated as  $(\overline{H}(+\Delta t; r) - \overline{H}(-\Delta t; r))/(2\Delta t)$ .

$\overline{H}(+\Delta t; r)$  and  $\overline{H}(-\Delta t; r)$  are shown in figure 36 for run 20 and run 16. Evidently  $\overline{H}(\pm\Delta t; r)$  becomes very small for small separations, but starts to grow for  $r \sim 20$  mm. For very small separation a Taylor expansion of the integrand shows that  $\overline{H}(r) \sim 0(r^2)$ . Within local homogeneity  $\overline{H}(r) = 1/8r^2 G_{ii}$ , which we expect to be small. Therefore the sudden, and seeming linear, growth at large separations is a surprising feature. The same behavior is seen in all experiments<sup>15</sup>. There could be some unresolved structure below 10 mm separation, but it seems reasonable to neglect it and set  $\overline{H}(\pm\Delta t; r) = 0$  for  $r < 10$  mm.

The idea is to make use of the fact that we resolve time down to about half a Kolmogorov time scale, which is much better than the spatial resolution. The pole in the integral on the right hand side of (99) is the problem. It is integrable, but  $\langle v_i(\mathbf{x}) a_j(\mathbf{x} + \mathbf{y}) \rangle$  peaks near  $\mathbf{y} = 0$ , and hence extremely good spatial resolution is required. The situation is better with  $\langle a_j(\mathbf{x} + \mathbf{y}) \rangle$ , and when  $\overline{H}(\pm\Delta t; r)$  is cut below 10 mm we get rid of the pole. Forming  $\frac{\overline{H}(\Delta t; r) - \overline{H}(-\Delta t; r)}{r^2 \Delta t}$  still requires good accuracy, so we are clearly pushing the particle tracking technique to its limits – and possibly beyond.

Figure 37 shows  $\langle \varepsilon \rangle$  determined by (105) as a function of  $r$ . The curves seem to approach constant values. Evidently there are problems for small  $r$ , where the statistical uncertainty is largest.

## 5.4 Summary of results

We have used the following volumes:

$$\begin{aligned} V_1 &= [-70, 70] \times [-70, 70] \times [-80, 40] \text{ mm}^3, \\ V_2 &= [-70, 70] \times [-70, 70] \times [-60, 30] \text{ mm}^3 \text{ and} \\ V_3 &= [-70, 70] \times [-70, 70] \times [-50, 10] \text{ mm}^3. \end{aligned} \tag{106}$$

The experimental conditions are described in the section 4. The results are listed in table 8 below. Note that Method 1 has been applied to all three test volumes.

The first three runs (12, 13 and 14) should be look at with caution because there were very few particles.

The methods generally give similar results, although there is no striking agreement between them. The variability, i.e. the difference between results for repeats with the same grid frequency, seems to less than the differences between the various methods.

Except for run 20 Method 0 gives the highest value. It sounds reasonable that pressure transport works against the kinetic energy flux.

The results for Method 1 and Method 2 differ for the three volumes generally with increasing energy dissipation for increasing volume. It is natural to expect that  $\langle \varepsilon \rangle$  increases nearer to the grids. Spatial variations of  $\langle \varepsilon \rangle$  make the results difficult to interpret because the spatial averaging within the test volume differs for the methods. Non-constant  $\langle \varepsilon \rangle$  contradicts local homogeneity making it is difficult to say exactly what kind of spatial average of  $\varepsilon$  is involved in Method 2.

We are not sure whether the disagreement between Method 2 and Method 3 is due to broken local homogeneity or it is simply experimental scatter.

In principle Method 3 should be the best, but it requires space around the test volume, hence only  $V_3$  has been used for this method. Statistical uncertainty is

---

<sup>15</sup>The onset of the growth is independent of  $V$ , but seems to decrease when the grid frequency is increased.

Table 8. Summary of results for the four different methods to determine  $\langle \varepsilon \rangle$ . Method 1 uses the second order structure function, Method 0 the correlation between velocity and acceleration, Method 2 the velocity acceleration structure function at small separations, and Method 3 more complicated statistics from (105). The first three runs have fewer particles than the last six.

Run	freq [Hz]	$\langle \varepsilon \rangle$ [mm <sup>2</sup> s <sup>-3</sup> ]							
		V <sub>1</sub>		V <sub>2</sub>		V <sub>3</sub>			
		Meth. 1	Meth. 2	Meth. 1	Meth. 2	Meth. 0	Meth. 1	Meth. 2	Meth. 3
12	3.00	149	145	120	137	189	98	126	35
13	2.99	160	164	127	159	206	108	142	141
14	2.98	140	152	109	140	121	87	116	70
15	2.96	135	120	108	113	150	92	92	128
16	2.97	160	151	126	144	149	105	119	123
17	2.00	62	63	49	42	70	41	27	52
20	3.50	279	185	234	224	200	204	236	284
21	3.45	225	163	186	194	217	160	191	184
22	2.00	65	81	50	73	65	40	60	67

larger for smaller volumes, so even if Method 3 is ‘exact’ it does not appear to be better than the other methods for the present data set. This might change with longer runs and denser particle seeding. Method 1, on the other hand, is robust because the second order structure function can be determined relatively better than velocity-acceleration correlations. For V<sub>3</sub> Method 3 gives consistently larger values than Method 1. This seems to indicate a lower value of the Kolmogorov constant than C<sub>K</sub>=2 used in Method 1, but the results are too uncertain to allow firm conclusions to be drawn. The results of Method 3 for V<sub>3</sub> agree better with the results of Method 1 for the larger volumes V<sub>1</sub> and V<sub>2</sub>, so perhaps it is also a matter of different spatial averages.

## 6 Kolmogorov’s four-fifth law

From the beginning it was the intention to use Kolmogorov’s (1941a) four-fifth law to determine the energy dissipation. The law is assumed to be exact for separations in the inertial range in the limit of infinite Reynolds numbers. Since R<sub>λ</sub> is always finite, the proper use of the four-fifth law to determine  $\langle \varepsilon \rangle$  involves an experimental verification in each situation. This is usually done by plotting the quantity  $K = -\langle \delta v_{\parallel}^3 \rangle / (\langle \varepsilon \rangle r)$  against r/η. The graph typically rises, levels off in a plateau with a maximum value K<sub>max</sub> and decreases again as r/η → ∞. The atmospheric measurements of Dhruva, Tsuji and Sreenivasan (1997) at high Reynolds numbers (R<sub>λ</sub> ~ 10000) confirm the four-fifth law. The dissipation was derived from measurements of the streamwise velocity component assuming isotropy, essentially a direct measurement. They found a clear plateau hitting K<sub>max</sub>=0.8 very closely. Even for these very high R<sub>λ</sub> the width of the plateau, defined as K being between 0.7 and 0.8, is only about one decade. Similar plots of boundary layer wind tunnel measurements were made by Saddoughi and Veeravalli (1994) for R<sub>λ</sub> = 1450 and R<sub>λ</sub> = 600. They find K<sub>max</sub> ~ 0.6 – 0.7, with  $\langle \varepsilon \rangle$  obtained from hot-wire measurements. Sreenivasan et al. (1996) made pipe flow measurements (R<sub>λ</sub> = 270) as well as direct numerical simulations (DNS) of isotropic and homogeneous turbulence

( $R_\lambda = 220$ ). The pipe data show a narrower plateau than for the DNS data.  $\langle \varepsilon \rangle$  was not measured in the pipe, but the DNS data hit 0.8 within a fraction of a percent over nearly one decade. Mydlarski and Warhaft (1996), using an active grid to generate shearless decaying turbulence, made measurements in the range  $R_\lambda = 43$  to 473. The dissipation was measured independently. Their results are qualitatively similar to the shear flow data of Saddoughi & Veeravalli and show progressively less distinct plateaus for decreasing  $R_\lambda$ . From figure 38 the maximum is 0.7 for  $R_\lambda = 448$  decreasing to only 0.45 at  $R_\lambda = 99$ . The analysis by Sreenivasan (1999) of several DNS box-flow simulations yield

$R_\lambda$	$K_{\max}$	Source
38	0.43	Yeung
90	0.63	Sreenivasan
140	0.68	Sreenivasan
212	0.80	Chen
240	0.76	Sreenivasan

The various results for  $K_{\max}$  are summarized in figure 39.

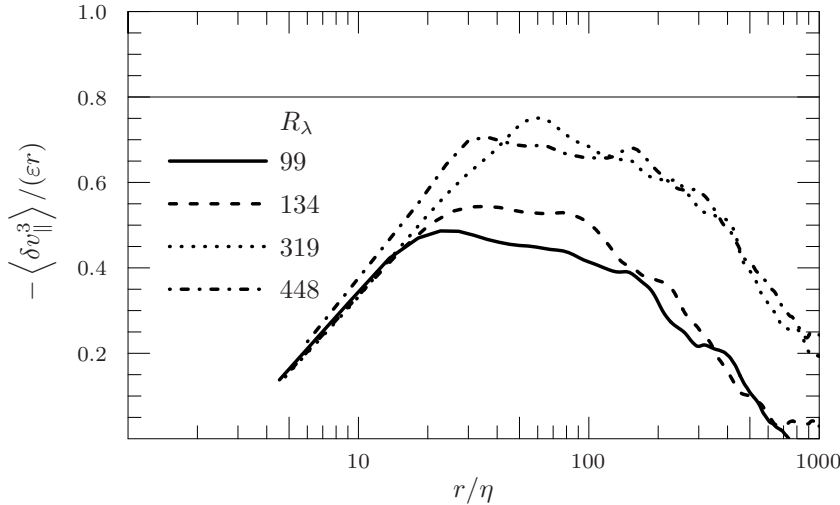


Figure 38. Experimental test of Kolmogorov’s four-fifth law. Data from Mydlarski and Warhaft (1996).

All these results indicate a rather limited range of separations for which the four-fifth law is valid even for quite high Reynolds numbers. Using the law to deduce  $\langle \varepsilon \rangle$  works well for large  $R_\lambda \sim 1000$ , but it seem to lead to large ( $\sim 100\%$ ) overpredictions for moderate  $R_\lambda \sim 100$ . The relatively modest success of the four-fifth law for smaller Reynolds numbers is not well understood, and it is worth noting that DNS simulations generally seem to obey the four-fifth law better than measurements, see figure 39. For large separations the deviations could be explained as lack of local homogeneity, local isotropy or local stationarity. Hill’s (1997) derivation assumes all three symmetries (using a strong definition of local symmetry). The use of Taylor’s hypothesis to obtain  $\delta v$  from hot-wire measurements confines separations to be along the streamwise direction, in which case local isotropy must be assumed in order to interpret the data. Particle tracking does not favor any particular direction and hence the experimental value of  $\langle \delta v_{||}^3 \rangle$

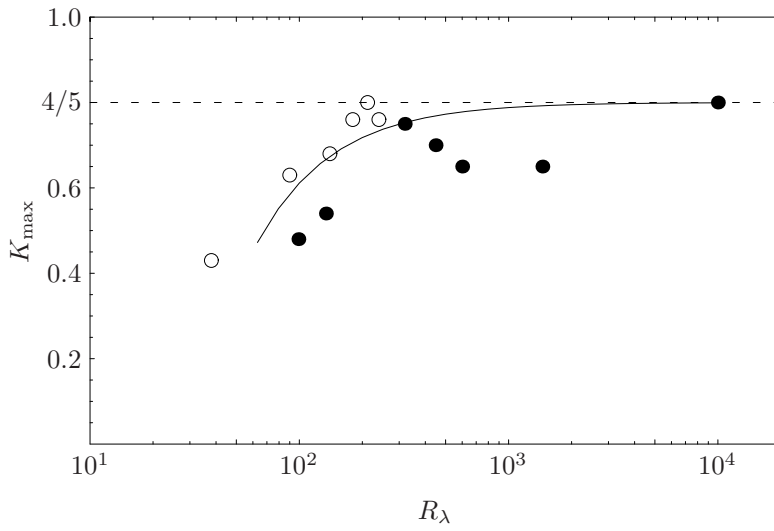


Figure 39. Values of  $K_{\max}$  determined experimentally (filled circles) and by DNS (open circles). The thin curve is given by Moisy et al. (1999), as a fit to their measurements in helium between counter-rotating disks.

can be determined as an average over the sphere  $|\mathbf{y}| = r$  of separation vectors  $\mathbf{y}$ . With this isotropic definition of structure functions isotropy need not be assumed to derive the four-fifth law. Below we offer a proof based only on local homogeneity and local stationarity.

Note that

$$\int_{|\mathbf{y}| < r} \langle \delta \mathbf{v} \cdot \delta \mathbf{a} \rangle d^3 y = \frac{\partial}{\partial s} \int_{|\mathbf{y}| < r} \left\langle \frac{1}{2} \delta v^2 \right\rangle d^3 y + \int_{|\mathbf{y}| = r} \left\langle \delta v_{\parallel} \frac{1}{2} \delta v^2 \right\rangle d^2 y \quad (107)$$

Equation (91) can therefore be written as

$$\frac{1}{r^2} \int_0^r r^2 \frac{\partial}{\partial s} B_{ii}(r) dr + B_{dii} = -\frac{4}{3} \langle \varepsilon \rangle r + \frac{2}{15} F_{ii} r^3, \quad (108)$$

where, for simplicity, we have dropped the small viscous terms. The term  $\frac{2}{15} F_{ii} r^3$  is new<sup>16</sup>. It is relevant when the mean flow is non-trivial, which is seldom the case in laboratory experiments. It could be important at high Reynolds numbers too. Large eddies live longer than small eddies and, if they live long enough for small eddies to adjust to them, they could be thought of as acting as a random ensemble of non-trivial mean flows. Seen in this way  $F_{ij} = 0$  looks like the exception.

The main point is that the time derivative refers to the local time. In other words,  $\frac{\partial}{\partial s} B_{ii}$  is due to the decay of kinetic energy *in a local system*. Therefore we cannot drop the term unless we assume *local* stationarity, which may not be a good idea for experimental flows, even if these are globally stationary. The reason is that measurements are confined to a domain located away from the places where energy is produced. We conjecture that in the tank, local kinetic energy is renewed each time the local system visits the grids, and, since this happens outside the test volume, we only observe an energy decay. The decay of local kinetic energy is seen on figure 40. At the smallest separations there is no decay, but at a moderate separation of about 13 mm it becomes larger than the divergence of the flux of kinetic energy  $\nabla \cdot \langle \delta \mathbf{v} \delta v^2 \rangle$ . What we see is the energy cascade of local kinetic

<sup>16</sup>A similar  $r^3$ -depending term was proposed by Novikov (1963) to describe the energy production due to random stirring forces. In our experiment, as in most other experiments, there are no external forces in the test domain.

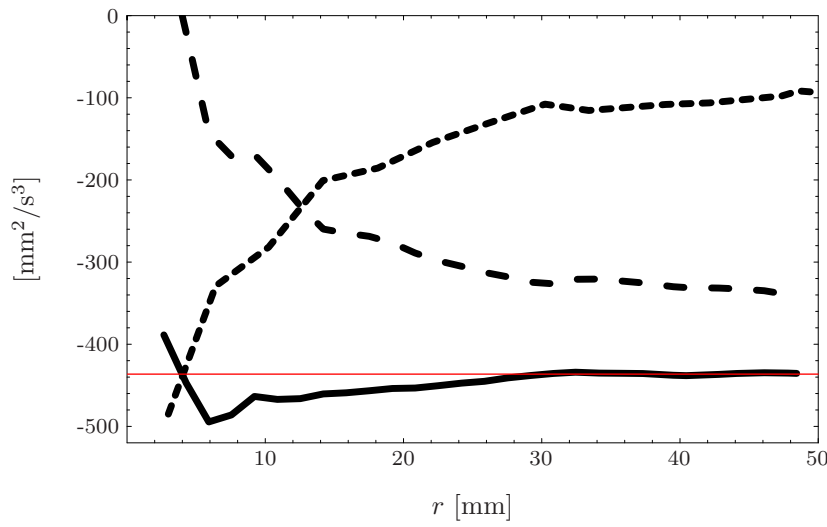


Figure 40. The three terms in (107). The almost constant solid curve is  $\langle \delta \mathbf{a} \cdot \delta \mathbf{v} \rangle$ , which in a locally homogeneous flow is  $-2 \langle \varepsilon \rangle$ . The increasing short dashed curve is  $\nabla \cdot \langle \delta \mathbf{v} \frac{1}{2} \delta v^2 \rangle$ , which should be equal to  $\langle \delta \mathbf{a} \cdot \delta \mathbf{v} \rangle$  if local stationarity is assumed. The long dashed curve is  $\langle \partial / \partial s \frac{1}{2} \delta v^2 \rangle$ , which is clearly non-zero, i.e. kinetic energy is decaying in a co-moving coordinate system.

energy, where energy at the origin is maintained by feeding on the energy at larger separations. It can therefore be claimed that assuming local stationarity would be to neglect the energy cascade. This argument should hold for most experimental flows. For DNS the situation is different because energy is normally maintained by a stirring force, which acts globally. Therefore local stationarity holds for the DNS flows. This could explain why the four-fifth law seems to work better in the computer than in the laboratory.

Recently, Lindborg (1999) has argued that spatial variations contribute to non-stationarity in a frame of reference following the mean flow and that the term  $\nabla \cdot \langle \mathbf{v} \rangle \langle 1/2 \delta v^2 \rangle$  should be retained. However, this does not help us here since  $\langle \mathbf{v} \rangle \approx 0$ .

Finally, we shall prove the four-fifth law. We believe this is the first proof based on local homogeneity. For the sake of simplicity we drop viscous terms and terms involving  $F_{ii}$  and  $G_{ii}$ . First  $B_{dii}$  is eliminated from (108) by means of (82)

$$\frac{1}{r^2} \int_0^r r'^2 \frac{\partial}{\partial s} B_{ii}(r') dr' + \left( \frac{4}{3} + \frac{r}{3} \frac{\partial}{\partial r} \right) B_{ddd} = -\frac{4}{3} \langle \varepsilon \rangle r. \quad (109)$$

Then we multiply both sides by  $r^3$  and integrate to obtain

$$\frac{3}{r^4} \int_0^r r' \int_0^r r''^2 \frac{\partial}{\partial s} B_{ii}(r'') dr'' dr' + B_{ddd}(r) = -\frac{4}{5} \langle \varepsilon \rangle r. \quad (110)$$

Finally we apply local stationarity in order to get rid of the first term and the four-fifth law follows. Our measurements show that this last step is inappropriate even though the flow is globally stationary.

For the sake of completeness we give the result when  $F_{ii}$ ,  $G_{ii}$  and the viscous terms are included. It is convenient also to eliminate  $B_{ii}$  using (77). This gives

$$B_{ddd}(r) = -\frac{4}{5} \langle \varepsilon \rangle r + 6\nu \frac{\partial B_{ddd}}{\partial r} - \frac{3}{r^4} \int_0^r r'^4 \frac{\partial}{\partial s} B_{ii}(r') dr' + \frac{8r^3}{105} F_{ii} - \frac{2r^3}{105} \frac{\partial G_{ii}}{\partial s}. \quad (111)$$

# 7 Relative dispersion

Having determined the energy dissipation  $\varepsilon$  we now turn to the investigation of Richardson–Obukhov’s law for two-particle diffusion

$$\langle |\mathbf{r}(\Delta t)|^2 \rangle = C\varepsilon\Delta t^3, \quad (112)$$

where  $\mathbf{r}(\Delta t)$  is the vector separating two fluid particles, and  $\Delta t = t - t_0$  is time measured from an initial time  $t_0$ , where the two particles were close together. The relation is believed to be valid for inertial subrange separations, corresponding to time lags  $\Delta t$  ranging roughly from the Kolmogorov time scale to the Lagrangian integral time scale. Being ‘close’ is also to be understood in the context of the inertial range, i.e. the initial separation should still be large compared to the Kolmogorov length scale. As discussed in the Introduction the constant  $C$  is not very well determined.

When we designed our tank experiment we thought of different ways of releasing a puff of particles in the water in order to be able to measure the relative dispersion. However, we could think of no way of doing this without disturbing the flow. Therefore, we decided to run the experiment with particles ‘well mixed’ with the water and observe pairs of particles that come close to each other simply by accident. This requires that the particle density is high enough for this to happen often.

Examples of tracks of particles that initially are close together are shown in figure 41. Some pairs stay together for a while, others diverge almost immediately. An ensemble of such double tracks is defined by selecting for each time instant  $t_0$  all pairs of particles separated by less than 3 mm. In other words being ‘close’ is interpreted here as being closer than 3 mm (about ten Kolmogorov length scales). A small initial separation should be preferred, but for smaller initial separations we get fewer pairs, and 3 mm seems to be a good compromise for the present data. Each pair is tracked in time starting from the time  $t_0$  where the particles were ‘close’. In this way the same two particles can contribute to many pairs in the ensemble, because a new separate pair is defined each time they get ‘close’. The reason for counting this way is that the selection of a pair then becomes independent of the separation in previous time steps<sup>17</sup>. The ensemble is used to estimate  $\langle r^2(\Delta t) | r(t_0) < r_0 \rangle$  with  $r_0 = 3$  mm.

In figure 42 separations as a function of time is shown for pairs that at  $\Delta t = t - t_0 = 0$  are closer than 3 mm. In order not to cover this figure with ink we have only shown tracks that at the time step before  $t_0$  were further apart than 3 mm, even though these are only a subset of the tracks that go into the average.

The resulting averages for all the runs are shown in figure 43. We have shown  $\langle |\mathbf{r}(\Delta t)|^2 \rangle^{1/3}$  so according to (112) these should be straight lines for  $r$  in the inertial subrange. The integral scale  $L_{\text{int}} \approx 22$  mm (see table 7) so  $|\mathbf{r}(\Delta t)|^{2/3}$  should be less than  $8 \text{ mm}^{2/3}$ . Looking at figure 42 this only seems to be true for the most of the track up to around 1 second. Two parameters are obtained by fitting a straight line to  $\langle |\mathbf{r}(\Delta t)|^2 \rangle^{1/3}$ . The slope is the parameter  $(C\varepsilon)^{1/3}$ . The second parameter of the fit is the zero crossing is  $T_0$ , which is generally found to be negative. This is to be expected because the initial separation  $r_0$  is finite. If we choose a smaller  $r_0$  some of the pairs of tracks will disappear from the ensemble. For those that remain, there will be fewer restarted pairs resulting from particles that ‘meet again’. The remaining double tracks will therefore tend to start earlier.  $T_0$  can be regarded as a compensation for this. For very small  $\Delta t$  we have  $\mathbf{r} \sim \mathbf{r}_0 + \delta\mathbf{v}(t_0)\Delta t$  so that  $\langle \mathbf{r}^2 \rangle \sim \langle \mathbf{r}_0^2 \rangle + \langle \delta\mathbf{v}^2 \rangle \Delta t^2$ . In figure 43 it looks as if such a regime exists for small  $\Delta t$ .

<sup>17</sup>If you just *wait* until a ‘close’ pair appears you will get a pair that was definitely not ‘close’ at the previous time step, and that would bias the ensemble.

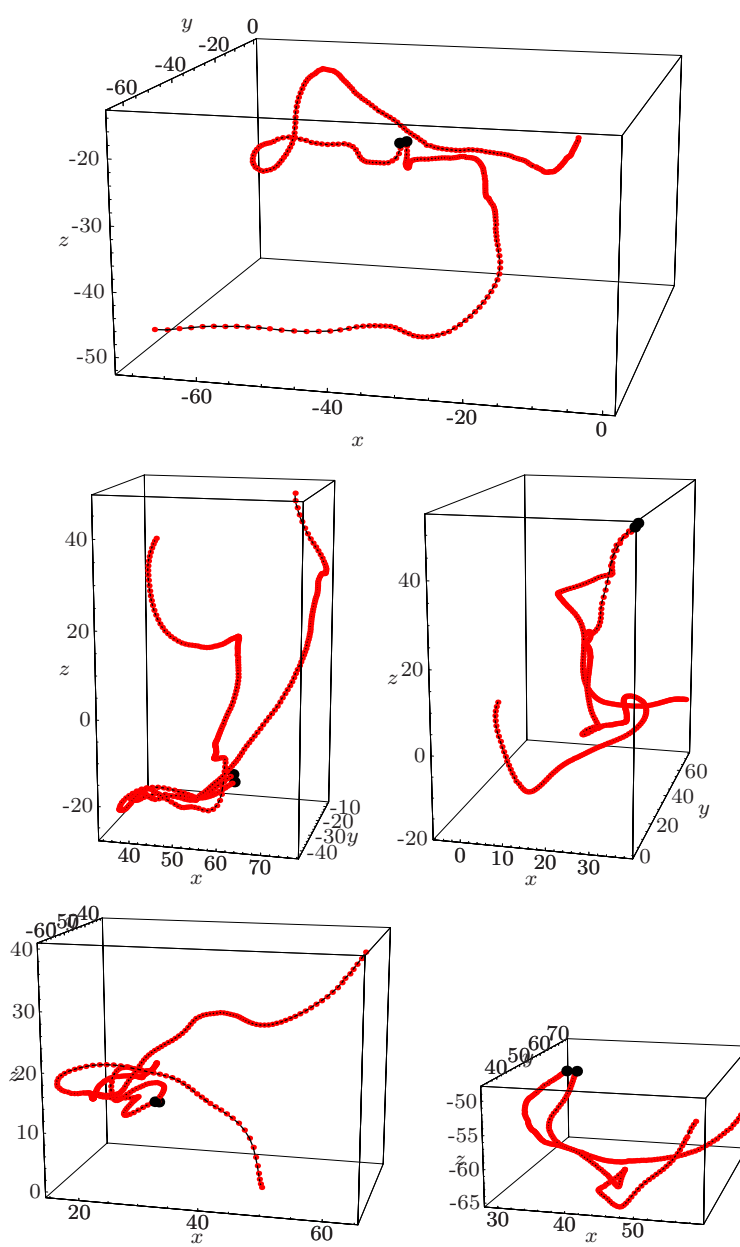


Figure 41. Tracks of pairs of particles that are initially within 2 mm of each other. The tracks start with a large black dot. The top plot and the middle left are from run 20, the lower left from 16 and two to the right from run 17.

This is not a violation of the Richardson-Obukhov law because it is not supposed to be valid for small  $\Delta t$ .

In figure 44 the curves of figure 43 have been translated in time with the amount  $T_0$ , i.e.  $\tau = \Delta t - T_0$  is used instead of  $\Delta t$ . Here the proportionality to  $\tau^3$  is seen more clearly. It is also seen that for small  $\tau$  the mean squared separation is not proportional to  $\tau^3$ .

From figure 44 the parameter  $C\varepsilon$  is derived, and using  $\varepsilon$  determined by the second order velocity structure method with  $C_K = 2.0$  (see table 7) we finally get

$$0.4 \lesssim C \lesssim 0.6 \quad (113)$$

as shown in figure 45.

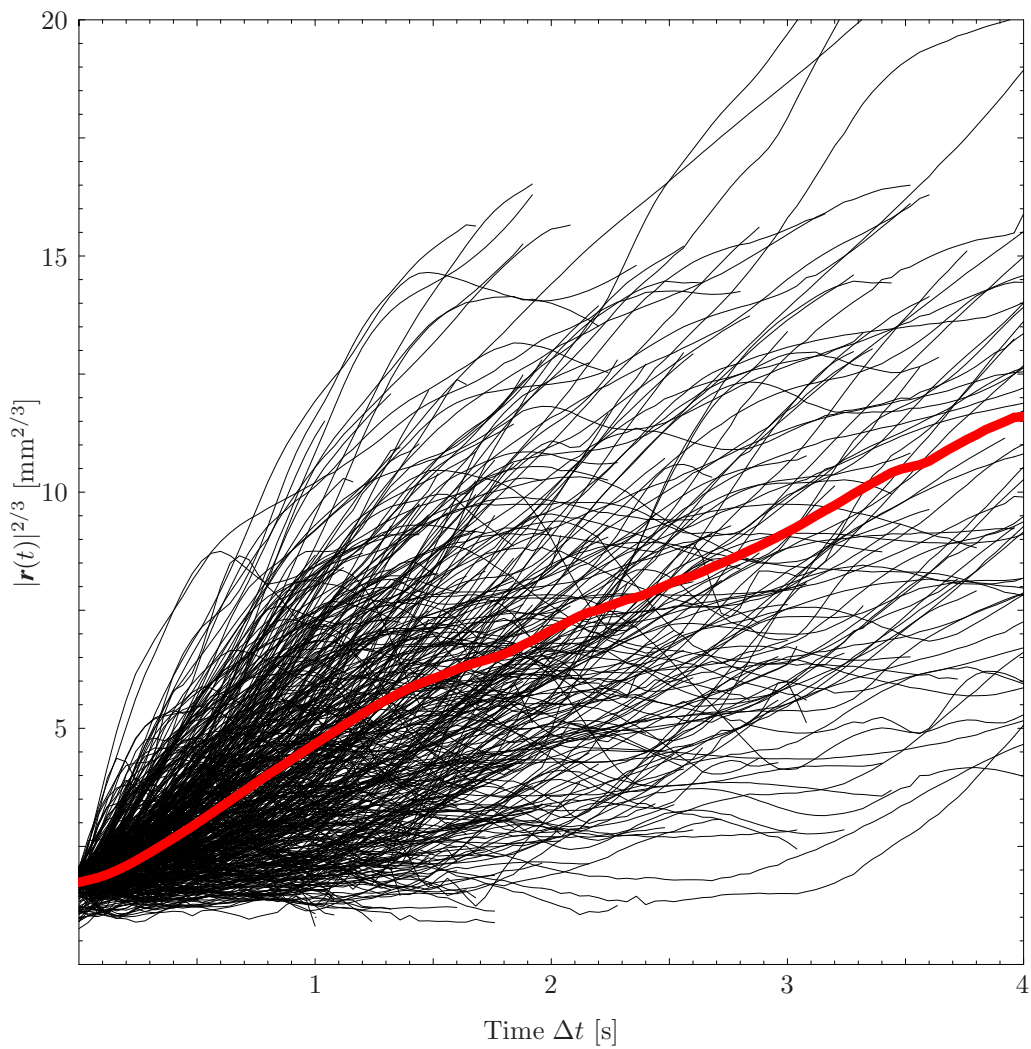


Figure 42. Tracks going into the calculation of  $\langle |\mathbf{r}(\Delta t)|^2 \rangle$  for run 17. The resulting average is superimposed as a thick, gray curve.

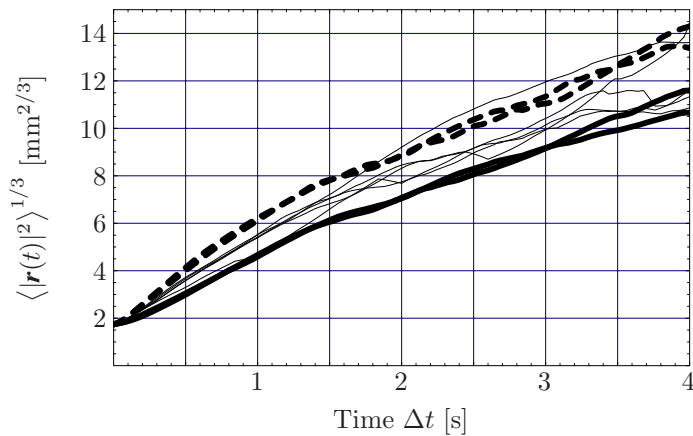


Figure 43. The mean squared separation as a function of time. Thick curves: 2 Hz, thin curves: 3 Hz, dashed curves: 3.5 Hz.

## 7.1 The Distance–Neighbour Function

Once the mean squared separation has been investigated the next step is to look at the underlying probability density function of separations giving rise to (112). To be more precise, we want to study the shape of the *distance–neighbour function*

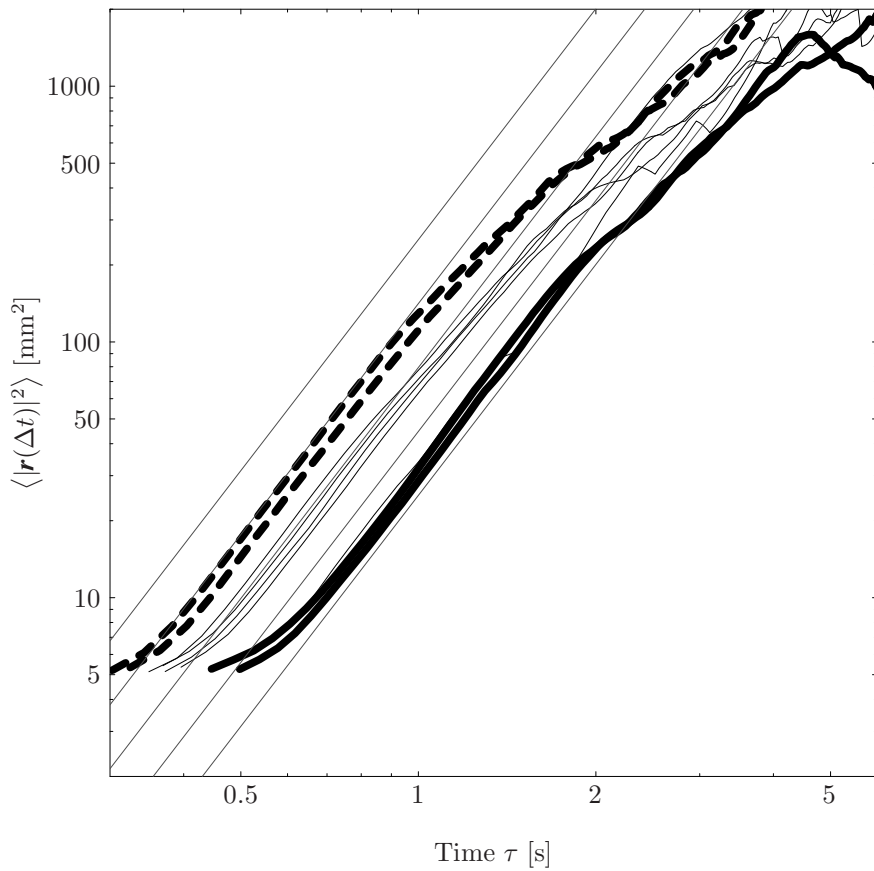


Figure 44. The same as figure 43 except that time has been corrected by  $T_0$  and axes are logarithmic. The thin straight lines are  $\propto \tau^3$ .

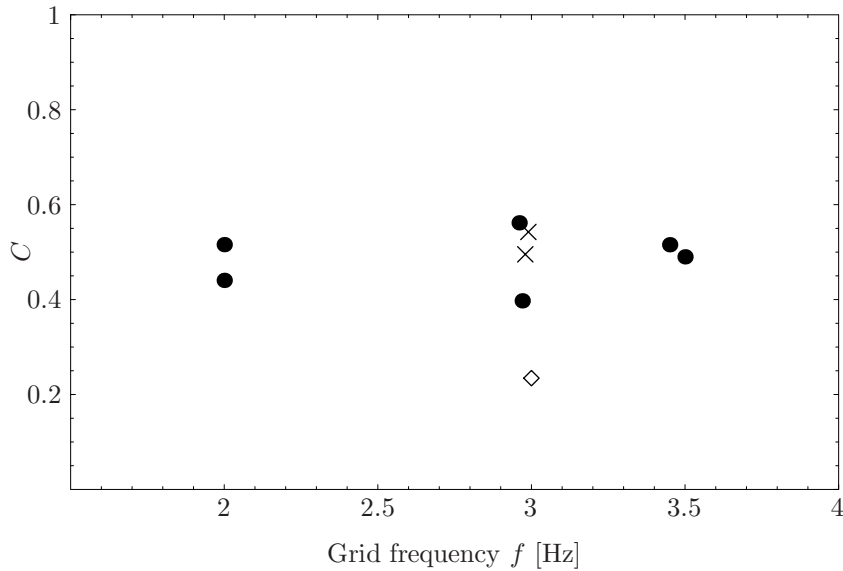


Figure 45. The Richardson-Obukhov constant  $C$  as a function of grid frequency. Dots are runs with many particles, crosses with fewer, and the diamond have even less. See table 5

$q$ , defined such that

$$q(\mathbf{r}, \tau) d^3\mathbf{r}$$

is the probability of finding the two particles in a small volume  $d^3\mathbf{r}$  in the space of separations at the time  $\tau$ , given that they initially, at  $\tau = 0$ , were close to each

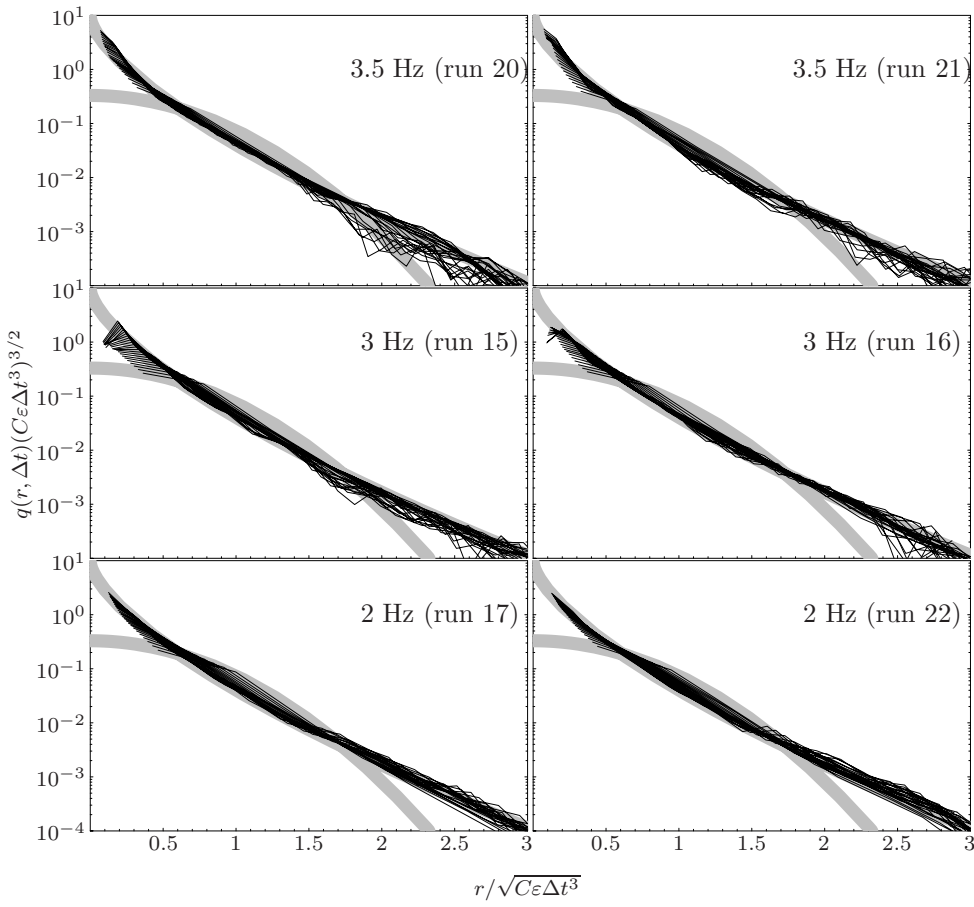


Figure 46. Distance neighbour functions with  $0.25 s < \Delta t < 1.25 s$  for the six runs with the most particles compared to the expressions of Richardson (118) and Batchelor (119). The theoretical curves are gray and broad. Richardson's is almost obscured by the 25 measured functions.

other. Usually, it is assumed that  $q$  only depends on  $r = |\mathbf{r}|$ .

There are two competing models for the shape of  $q$ . Richardson (1926) suggested

$$\log q(r, \tau) \propto \left( \frac{r^2}{\varepsilon \tau^3} \right)^{1/3} \quad (114)$$

while Batchelor (1952) proposed

$$\log q(r, \tau) \propto \frac{r^2}{\varepsilon \tau^3}. \quad (115)$$

In order for these to be probability density functions they must obey

$$\int_0^\infty 4\pi r^2 q(r, \tau) dr = 1 \quad (116)$$

for all  $\tau$ , and they must also fulfill the Richardson-Obukhov law (112), i.e

$$\int_0^\infty 4\pi r^2 q(r, \tau) r^2 dr = C\varepsilon \Delta t^3. \quad (117)$$

Solving these constraints for the case of the model of Richardson leads to

$$q_R(r, \tau) = \frac{429}{70} \sqrt{\frac{143}{2}} \pi^{-3/2} (C\varepsilon \tau^3)^{-3/2} \exp \left[ - \left( \frac{1287 r^2}{8 C \varepsilon \tau^3} \right)^{1/3} \right], \quad (118)$$

and for the Batchelor case

$$q_B(r, \tau) = (2\pi)^{-3/2} (C\varepsilon \tau^3/3)^{-3/2} \exp \left[ - \frac{1}{2} \frac{r^2}{C\varepsilon \tau^3/3} \right]. \quad (119)$$

To estimate  $q(r, \tau)$  experimentally, we count the number pairs in a spherical shells given by some interval in  $r$  of for a given  $\tau = \Delta t - T_0$  that were closer than 3 mm at  $\Delta t = 0$ . By normalizing with the total number of pairs in all shell at the given  $t$  and dividing by the volume of each shell we get an estimate of  $q(r, \tau)$  as a function of  $r$ . It is reasonable to restrict the analysis to time lags that are large enough for the distribution to become independent of the initial conditions. Based on figure 43 we believe that this is the case when  $0.25 s < \Delta t < 1.25 s$ . In figure 46 we show a comparison of Richardson and Batchelor's model with the experiment. The data are in excellent agreement with Richardson's expression (118). It is also clear that they are incompatible with Batchelor's expression (119).

This result is in direct conflict with the recent measurements by Virant and Dracos (1997) who at an comparable  $R_\lambda$  get an excellent agreement with Batchelor's expression. However, their initial puff is larger than the integral scale, so their experiment has nothing to do with relative diffusion at inertial subrange distances.

## 8 Further investigations

In this section we describe examples of ongoing work, which has not yet completed.

### 8.1 Expansion of the Eulerian velocity tensor

It is clear that the two-grid flow is not isotropic, but how anisotropic is it?

One way of answering this question is to decompose the second order structure tensor  $\langle \delta v_i(y) \delta v_j(y) \rangle$  using spherical harmonics. We recall that any scalar function on a sphere can be decomposed the following way

$$f(\theta, \phi) = \sum_{l=0}^{\infty} \sum_{m=-l}^l C_{jm} Y^{jm}(\theta, \phi) \quad (120)$$

where  $C_{lm}$  are constants uniquely specifying  $f$  and  $Y^{jm}(\theta, \phi)$  is a spherical harmonic specified by two integers  $l$  and  $m$ , which we can refer to as quantum numbers.  $j$  is non-negative and  $m$  can range between  $-j$  and  $+j$ , thus each  $j$  corresponds to a family of  $2j + 1$  orthogonal spherical harmonics. The significance of the  $j$  and  $m$  are as follows. When  $f$  is rotated around any axis we get a new function, with new coefficients  $C'_{jm}$ . The relation between these and  $C_{jm}$  is not simple, but it is linear and it does not mix different values of  $l$ . In other words, the linear space spanned by the  $j$ -family of spherical harmonics is invariant to rotations. For  $j=0$  there is only one member, which itself must be invariant to rotations, i.e. it is isotropic. It is of course constant. All other families mix under a rotation, and none of the members are isotropic. Furthermore rotations can mix all members of a family, so the family cannot be reduced. This means that  $l$  can be regarded as a measure of the degree on anisotropy. For example  $Y^{1,-1}$ ,  $Y^{1,0}$  and  $Y^{1,1}$  can describe a flattened sphere, the simplest deviation from a perfect sphere. The quantum number  $m$  describes cylinder symmetry with respect to the quantization axis, which we choose to be the  $z$ -axis, so that  $m = 0$  corresponds to perfect cylinder symmetry and increasing asymmetry for increasing  $|m|$ .

For the squared norm we have

$$\int_{4\pi} |f|^2 d\Omega = \sum_{l,m} |C_{lm}(r)|^2 \quad (121)$$

Things are more complicated for  $\langle \delta v_i(y) \delta v_j(y) \rangle$  because it is a tensor rather than a scalar, but the families remain. It is still possible to construct an orthogonal set

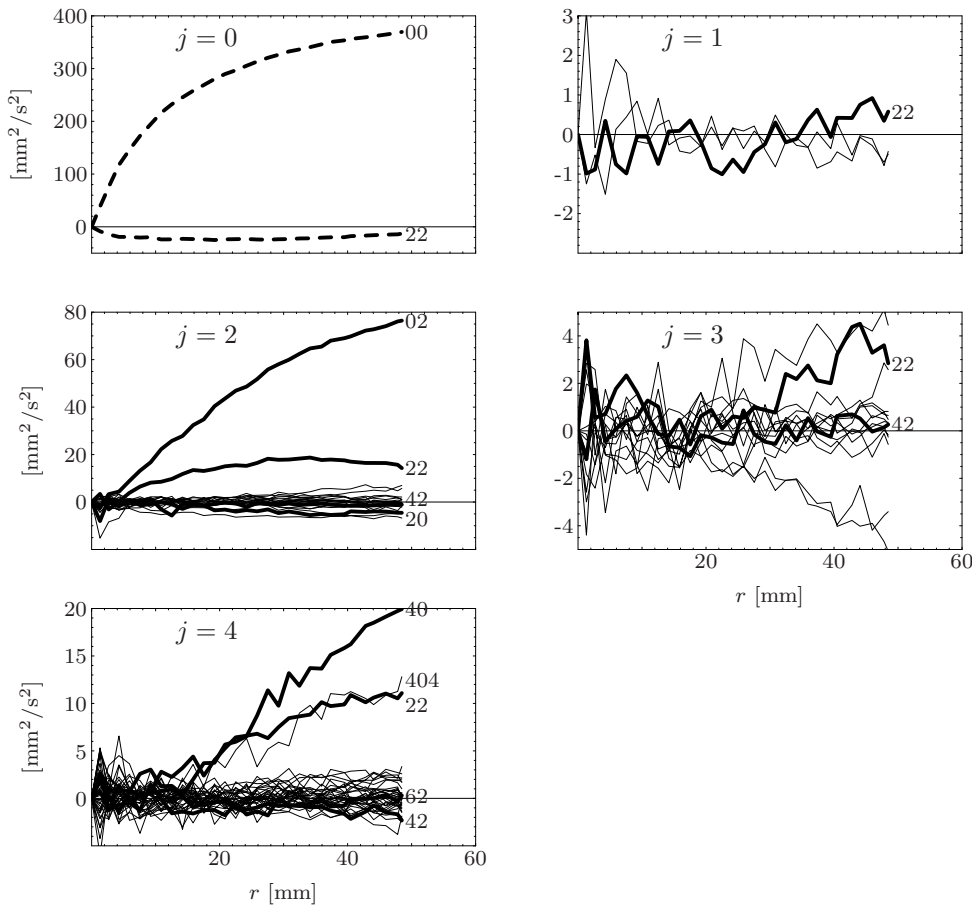


Figure 47. Coefficients  $C_{j l s m}$  as functions of  $r$  for the structure tensor of rank two. All isotropic (dashed curves) and axisymmetric coefficients (solid thick curves) are labeled with the quantum numbers  $l$  and  $s$ , and selected non-axisymmetric coefficients (thin curves) are labeled with the numbers  $l$ ,  $s$  and  $m$ .

of tensors functions on the sphere with irreducible families. The quantum numbers  $j$  and  $m$  can be given the same interpretation as for the scalar case, but besides  $j$  there additional quantum numbers are needed to specify a family uniquely. It would lead too far to explain how these families are constructed, we refer to Edmonds (1957). The decomposition of the second order structure tensor looks like this

$$\langle \delta v_p(\mathbf{r}) \delta v_q(\mathbf{r}) \rangle = \sum_{j=0}^{\infty} \sum_{s=0}^2 \sum_{l=|j-s|}^{j+s} \sum_{m=-j}^j C_{j l s m}(r) Y_{pq}^{j l s m}(\theta, \phi), \quad (122)$$

The squared norm is

$$\begin{aligned} \int_{4\pi} \langle \delta v_q \delta v_p \rangle^2 d\Omega &= \sum_{j l s m} |C_{j l s m}|^2 \\ &= \underbrace{\sum_{j=0} |C_{j l s m}|^2}_{\text{isotropic}} + \underbrace{\sum_{\substack{m=0 \\ j>0}} |C_{j l s m}|^2}_{\text{axi-symmetric}} + \sum_{\text{the rest}} |C_{j l s m}|^2 \end{aligned} \quad (123)$$

There are similar and even more complicated expressions for the tensors of rank 3 and 4 etc. For fixed  $j$  and  $m$  we use the sum of  $|C_{j l s m}|^2$  over all other quantum

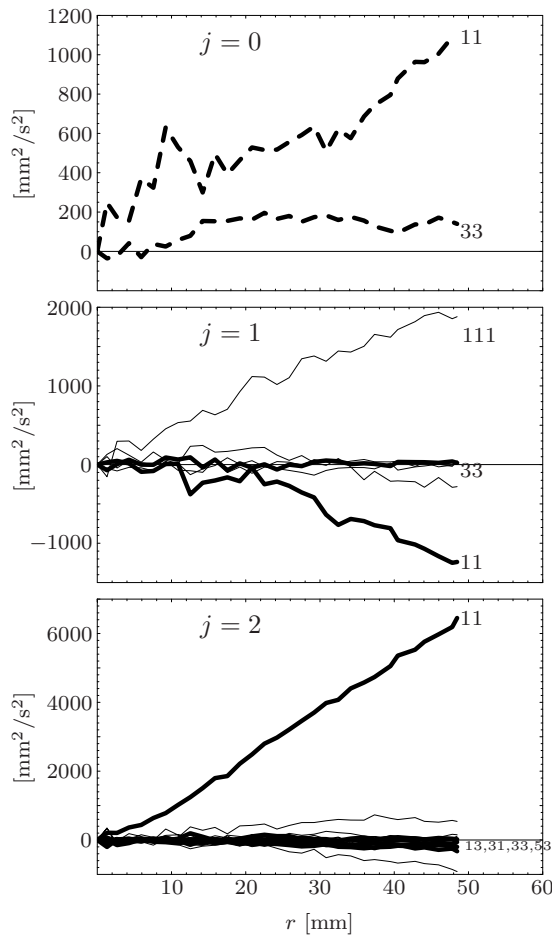


Figure 48. Coefficients  $C_{jls m}$  as functions of  $r$  for the structure tensor of rank three. All isotropic and axisymmetric coefficients are labeled with  $l$  and  $s$ , and selected coefficients are labeled with  $l$ ,  $s$  and  $m$ .

numbers as a measure of the anisotropy. In (123) we have split  $\int_{4\pi} \langle \delta v_p \delta v_q \rangle^2 d\Omega$  into just three parts: the isotropic part, the axi-symmetric part and the rest.

Experimentally it becomes very difficult to measure things as  $j$  and  $m$  increase. We have not attempted to go beyond  $j=4$  for the second order structure function. There are 75 coefficients with  $j \leq 4$ . For the rank 3 and rank 4 tensors we limit ourselves to  $j \leq 2$ , giving 33 and 44 coefficients, respectively.

We have not gone very far with this analysis and at present only results for run 20 are available. For the analysis we use pairs of points where each point is within  $[-60, 60] \times [-60, 60] \times [-70, 40]$  mm<sup>3</sup> with a maximum separation of  $r = 50$  mm. See figure 47, 48 and 49

The results are summarized in figure 50. It appears that the isotropic component  $j = 0$  is large and completely dominates as  $r \rightarrow 0$ . This confirms isotropy at small scales. The axi-symmetric part increases for increasing separation, while 'the rest' is so small that it could be just noise. It therefore seems that the two-grid turbulence is very close to being axi-symmetric even at large separations.

These results demonstrate that the decomposition into spherical harmonics is within reach with the particle tracking technique. It would be instructive to rewrite the NSE in terms of spherical harmonics in order to see how dynamics mix the families. However that project tends to drown in Clebsch-Gordon coefficients. A more streamlined notation, tailored specifically to non-linear differential equations, is needed. We hope to be able to continue these investigations.

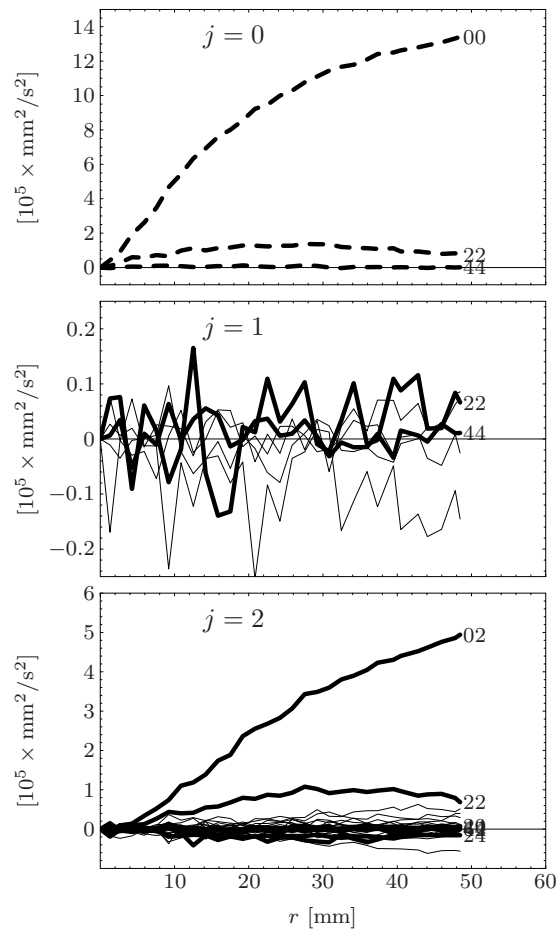


Figure 49. Coefficients  $C_{j l s m}$  as functions of  $r$  for the structure tensor of rank four. See caption of figure 47.

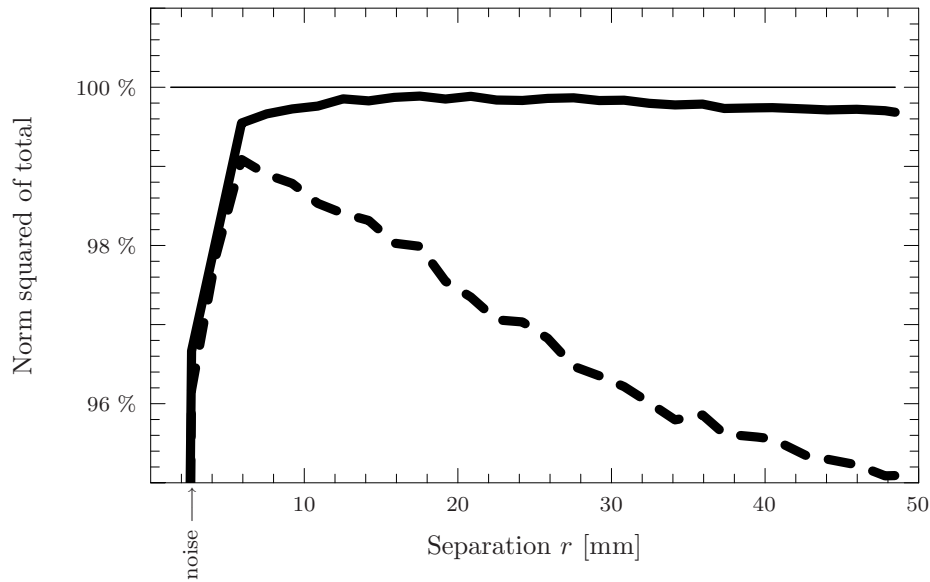


Figure 50. Vanishing of anisotropy for  $r \rightarrow 0$ . The dashed curve is the isotropic contribution to the squared norm, i.e. the first term in (123). The solid line is the isotropic plus the axi-symmetric terms.

## 8.2 One particle Lagrangian autocorrelation functions

Autocorrelation functions of the individual components of the acceleration are defined as

$$\rho_{a_i}(\tau) = \frac{\langle a_i(t) \cdot a_i(t + \tau) \rangle}{\langle a_i^2 \rangle}, \text{ with } i \in \{x, y, z\}, \quad (124)$$

where  $\tau$  denotes the time lag and  $i$  denotes the components. Figure 51 shows these autocorrelation functions as well as the similarly defined autocorrelation function of the magnitude of the acceleration.

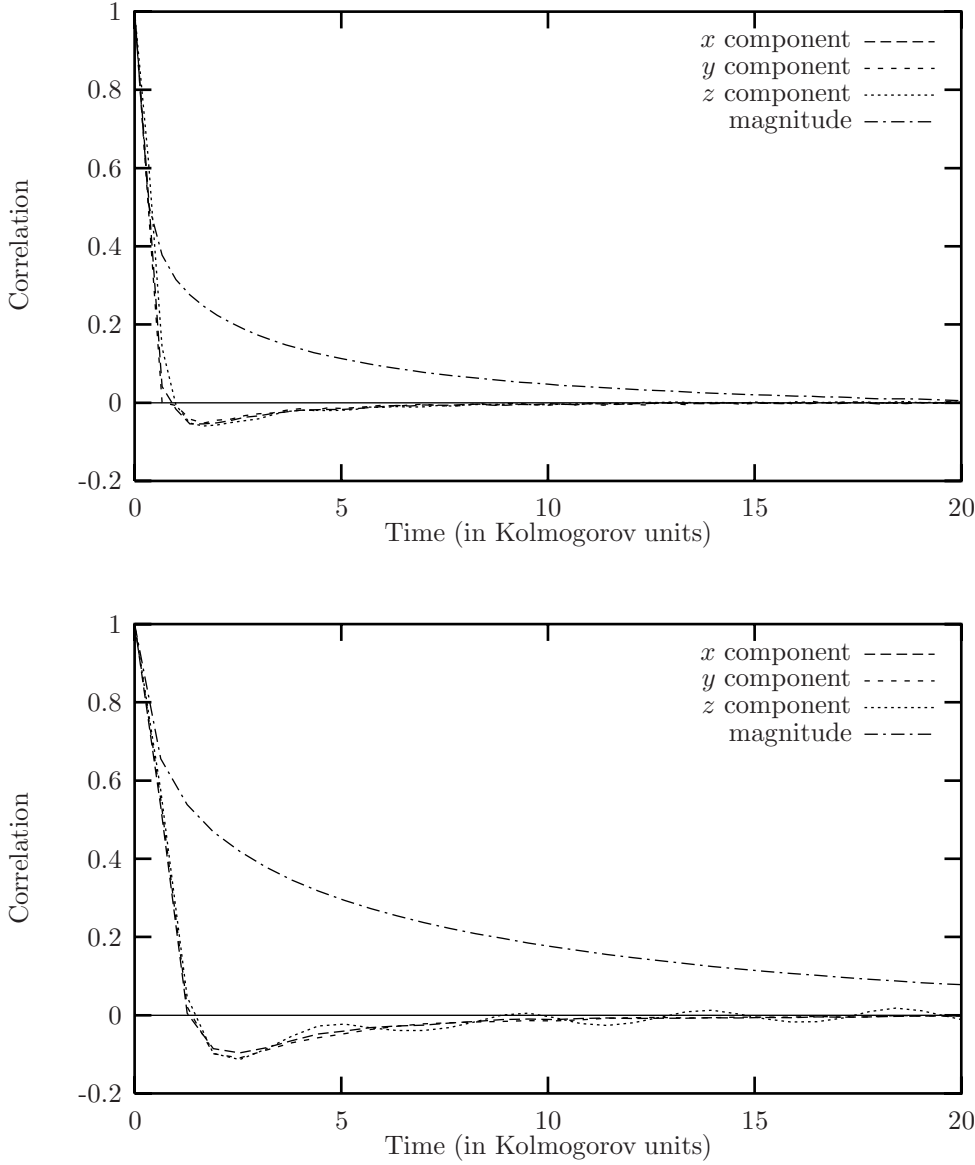


Figure 51. Lagrangian acceleration autocorrelations: The upper graph shows data set 17 (2.00 Hz, grids in counter-phase). The lower graph shows data set 21 (3.46 Hz, grids in phase).

We see that the component correlation functions have approximately the same area above and below the axis. This indicates that the particle velocity could be

a stationary random function, since the time derivative of a stationary time series has integral scale zero.

We see that the magnitude of the acceleration of a particle is correlated over a significant period of time, more than one Kolmogorov time scale, compared to the time the individual components of the acceleration are correlated.

The zero-crossing of the component correlations is at about 1.0 Kolmogorov time scales, which is significantly lower than the 2.2 Kolmogorov time scales found in (Yeung 1997). The difference could be due to the inhomogeneous flow or to the Lagrangian non-stationarity of the flow.

The relative values of the correlation time for the magnitude of the acceleration and the zero-crossing time of the component correlations is similar to what (Yeung 1997) reports.

## 9 Summary and conclusions

A system for tracking particles immersed in a turbulent flow has been established. The design and the construction of the system took place in 1997 and is to a large extent based on Dracos (1996). Due to advances in technology there are some improvements and simplifications compared to previous systems, f.ex. the real time compression and storage on hard disks using hardware implemented JPEG compression on two PCs. Other differences are the use of a stroboscope and the way particle positions are reconstructed in three-dimensional space. With the technology of today (1999) further improvements are possible. With the increasing speed of PCs it should be possible to run the data acquisition for all four cameras on *one* PC without using compression cards, but by using a software compression algorithm which is optimized for black images with white spots. (JPEG is optimized for ordinary pictures, e.g. faces, flowers, etc.)

The accuracy of the determination of particle positions is approximately 40  $\mu\text{m}$ . This is actually much better than we had aimed at.

The two-grid generated turbulent flow is characterized by very low mean velocities, less than  $\sim 10\%$  of the rms value. In the experiments reported here we have obtained Reynolds numbers based on Taylor's microscale of about one hundred. Higher values of  $R_\lambda$  can probably be obtained rather easily. For example the grid frequency could be increased or stacks of grids could be used in order to make the energy transfer more efficient. The integral length scale could be increased by moving the grids further apart and a larger grid spacing could be used. This too would increase  $R_\lambda$ . However, obtaining large Reynolds numbers has not been the primary objective.

A main objective of this work has been the experimental determination of the constant in the Richardson-Obukhov relation. We find  $C \approx 0.4 - 0.6$ . The largest source of uncertainty probably lies in the determination of the energy dissipation.

Several methods were used to determine  $\langle \varepsilon \rangle$ . Apart from statistical uncertainty, the results indicate rather large spatial variation. The agreement between the four methods of estimating  $\langle \varepsilon \rangle$  described in section 5 is fair.

The experiments show that Richardson's estimate of the distance-neighbour function is far superior to that of Bachelor. This could be taken as an indication that the simple first order closure used by Richardson is correct.

Preliminary results of an investigation of anisotropy of structure tensors of rank two, three and four is reported. Intensive use is made here of the fact that the particle tracking method is truly three-dimensional. The results indicate that the turbulence is very nearly axi-symmetric, even for large separations, with a strong isotropic component that dominates at small separations.

One particular aspect of the experiment has been much more difficult (and also more rewarding) than anticipated, namely the search for a fundamental way to estimate the energy dissipation (i.e. not merely using the second order velocity structure function, which assumes knowledge of the empirically determined Kolmogorov constant). We do not claim to have developed these methods to a level where we trust them more than the method based on the structure function. However, the search for better methods leads us to consider more fundamental aspects of symmetry in turbulence. The simple relation  $\langle \delta v \cdot \delta a \rangle = -2 \langle \varepsilon \rangle$  and the relatively simple proof of Kolmogorov's four-fifth law, based on local homogeneity, are spin-offs of these investigations. We also explain and demonstrate experimentally that local *non-stationarity* is important at moderate Reynolds numbers.

## Acknowledgments

This project was funded by the Danish Technical Research Council (STVF) under contract 9601244. An early preparatory project was funded by Risø. The authors are grateful to Professor Arkady Tsinober of Tel Aviv University, Dr. Bjarne Stenum and Mr. Jan Nielsen both of Risø for many important suggestions in the design of the experiment. The company Image House, Copenhagen, has been very helpful explaining various aspects of video recording. Thanks to comments from Dr. Leif Kristensen, Risø, and Professor Hans Pecseli, University of Oslo, the report has improved substantially.

## References

- AG&G: 1995, Linear flashlamps. Technical note from AG&G Electro-Optics.
- Antonia, R. A., Zhou, T. and Zhu, Y.: 1998, Three-component vorticity measurements in a turbulent flow, *Journal of Fluid Mechanics* **374**, 29–57.
- Batchelor, G. K.: 1952, Diffusion in a field of homogeneous turbulence. ii the relative motion of particles., *Proc. Cambridge Phil. Soc.* **48**, 345–363.
- Chasnov, J. R.: 1991, Simulation of the Kolmogorov inertial subrange using an improved subgrid model, *Phys. Fluids A* **3**(1), 188–200.
- De Silva, I. P. D. and Fernando, H. J. S.: 1994, Oscillating grids as a source of nearly isotropic turbulence, *Physics of Fluids* **6**(7), 2455–2464.
- Dhruva, B., Tsuji, Y. and Sreenivasan, K. R.: 1997, Transverse structure functions in high-Reynolds-number turbulence, *Phys. Rev. E* **56**(5), R4928–4930.
- Dracos, T.: 1996, *Three-dimensional velocity and vorticity measuring and image analysis techniques. Lecture notes.*, Vol. 4 of *ERCOFTAC*, Kluwer Academic Publishers, Dordrecht.
- Durbin, P. A.: 1980, A stochastic model of two-particle dispersion and concentration fluctuations in homogeneous turbulence, *J. Fluid Mech.* **100**, 279.
- Edmonds, A. R.: 1957, *Angular Momentum in Quantum Mechanics*, Princeton University Press, New Jersey.
- Fernando, H. J. S. and Silva, I. P. D. D.: 1993, Note on secondary flows in oscillating-grid, mixing-box experiments, *Phys. Fluids A* **5**(7), 1849–1851.

- Frisch, U.: 1995, *Turbulence, The Legacy of A. N. Kolmogorov*, Cambridge University Press, Cambridge.
- Fung, J. C. H., Hunt, J. C. R., Malik, N. A. and Perkins, R.: 1992, Kinematic simulation of homogeneous turbulence by unsteady random Fourier modes, *J. Fluid Mech.* **236**, 281–318.
- Giesberts, T.: 1994, Stroboscope light, *Elektor Electronics* **4**, 62–66.
- Hill, R.: 1997, Applicability of kolmogorov’s and monin’s equation of turbulence, *Journal of Fluid Mechanics* **353**, 67–81.
- Hinze, J. O.: 1975, *Turbulence*, 2nd edn, McGraw-Hill, New York.
- Jullien, M.-C., Paret, J. and Tabeling, P.: 1999, Richardson pair dispersion in two-dimensional turbulence, *Physical Review Letters* **82**(14), 2872–2875.
- Koecher, W.: 1976, *Solid-State Laser Engineering*, Springer-Verlag. Springer Series in Optical Sciences.
- Kolmogorov, A. N.: 1941a, Dissipation of energy in locally isotropic turbulence, *Dokl. Akad. Nauk SSSR* **32**(1). English translation in *Proc. R. Soc. Lond. A* (1991) **434**, 15–17.
- Kolmogorov, A. N.: 1941b, The local structure of turbulence in incompressible viscous fluid for very large Reynolds numbers, *Dokl. Akad. Nauk SSSR* **30**(4). English translation in *Proc. R. Soc. Lond. A* (1991) **434**, 9–13.
- Kraichnan, R. H.: 1966, Dispersion of particle pairs in homogeneous turbulence, *Physics of Fluids* **10**(9), 1937–1943.
- Kristensen, L. and Kirkegaard, P.: 1987, Puff kinematics, *Technical Report R-548*, Risø National Laboratory.
- Larchevêque, M. and Lesieur, M.: 1981, The application of eddy-damped Markovian closures to the problem of dispersion of particle pairs, *J. Méc.* **20**, 113–134.
- Lindborg, E.: 1996, A note on kolmogorov’s third-order structure-function law, the local isotropy hypothesis and the pressure-velocity correlation, *Journal of Fluid Mechanics* **326**, 343–356.
- Lindborg, E.: 1999, Corrections to the four-fifth law due to variations of the dissipation, *Physics of Fluids* **11**, 510–512.
- Malik, N. A., Dracos, T. and Papantoniou, D. A.: 1993, Particle tracking velocimetry in three-dimensional flows. part ii: Particle tracking, *Experiments in Fluids* **15**, 279–294.
- Mikkelsen, T.: 1982, A statistical theory on the turbulent diffusion of gaussian puffs, *Technical Report Risø-R-475*, Risø National Laboratory.
- Moisy, F., Tabeling, P. and Willaime, H.: 1999, Kolmogorov equation in a fully developed turbulence experiment, *Phys. Rev. Lett.* **82**(20), 3994–3997.
- Monin, A. S.: 1959, Theory of locally isotropic turbulence, *Dokl. Akad. Nauk SSSR* **125**, 515–518.
- Monin, A. S. and Yaglom, A. M.: 1975, *Statistical Fluid Mechanics*, Vol. 2, The MIT Press.
- Mydlarski, L. and Warhaft, Z.: 1996, On the onset of high-reynolds-number grid-generated wind tunnel turbulence, *J. Fluid Mech* **330**, 331–368.

- Novikov, Y. A.: 1963, Random force method in turbulence theory, *Sovjet Phys. JETP* **17**, 1449–1453.
- Obukhov, A. M.: 1941, Spectral energy distribution in turbulent flow, *Izv. Akad. Nauk SSSR* **5**, 453–566.
- Ott, S.: 1992, *Perturbative Methods in Turbulence and Turbulent Diffusion*, PhD thesis, University of Copenhagen.
- Press, W. H., Flannery, B. P., Teukolsky, S. A. and Vetterling, W. T.: 1992, *Numerical Recipes*, 2nd edn, Cambridge University Press.
- Richardson, L. F.: 1926, Atmospheric diffusion shown on a distance-neighbour graph, *Proc. Roy. Soc. London A* **110**, 709–737.
- Saddoughi, S. G. and Veeravalli, S. V.: 1994, Local isotropy in turbulent boundary layers at high reynolds number, *J. Fluid Mech* **268**, 333–372.
- Srdic, A., Fernando, H. J. S. and Montenegro, L.: 1996, Generation of nearly isotropic turbulence using two oscillating grids, *Experiments in Fluids* **20**(5), 395–397.
- Sreenivasan, K. R.: 1999. Private communication.
- Sreenivasan, K. R., Vainshtein, S. I., Bhiladvala, R., Gil, I. S., Chen, S. and Cao, N.: 1996, Asymmetry of velocity increments in fully developed turbulence and the scaling of low-order moments, *Physical Review Letters* **77**, 1488–1491.
- Taylor, G. I.: 1921, Diffusion by continuous movements, *Proc. London Math. Soc.* **20**, 196–211.
- Thomson, D. J.: 1990, A stochastic model for the motion of particles pairs in isotropic high-Reynolds-number turbulence, and its application to the problem of concentration variance., *J. Fluid Mech.* **210**, 113–153.
- Tsinober, A., Kit, E. and Dracos, T.: 1992, Experimental investigation of the field of velocity gradients in turbulent flows, *Journal of Fluid Mechanics* **242**, 169–192.
- Virant, M. and Dracos, T.: 1997, 3D PTV and its application on Lagrangian motion, *Meas. Sci. Technol.* **8**, 1529–1552.
- von Kármán, T.: 1948, Progress in the statistical theory of turbulence, *Proc. National Akad. Sci.* **34**, 530–539.
- Yeung, P. K.: 1997, One- and two-particle Lagrangian acceleration correlations in numerically simulated homogeneous turbulence, *Physics of Fluids* **9**(10), 2981–2990.

---

 Title and author(s)

Experimental Study of Relative, Turbulent Diffusion

Jakob Mann, Søren Ott and Jacob Sparre Andersen

---

 ISBN

87-550-2370-3; 87-550-2603-6 (Internet)

ISSN

0106-2840

---

 Dept. or group

Date

22nd September  
1999

---

 Groups own reg. number(s)

1100 034-00

Project/contract No.

STVF-9601244

---

 Pages

75

Tables

8

Illustrations

51

References

45

---

 Abstract (Max. 2000 char.)

The purpose is to study relative turbulent diffusion under controlled, reproducible conditions in the laboratory in order to estimate the constant  $C$  in Richardson-Obukhov's law. We get  $C \approx 0.4 - 0.6$ . We furthermore measure the distance-neighbour function, which is the probability density function of the separation of two fluid particles that are initially close to each other. We find that the model proposed by Richardson is far superior to the one suggested by Batchelor.

To obtain these results we use the Particle Tracking (PT) technique to measure trajectories of fluid particles in a water tank with two oscillating grids generating turbulence. In the experiments reported here we have obtained Reynolds numbers based on Taylor's microscale of about one hundred. The PT system, which is also described in this report, consists of four CCD cameras, a synchronous light source and a recording system with two computers each equipped with a frame grabber card.

In the search for the best experimental methods we have revised the concept of local homogeneity and derived a law for the velocity-acceleration structure function. A second by-product of this effort is a relatively simple derivation of Kolmogorov's four-fifth law based on the assumption of local homogeneity. Finally, we measure the full velocity structure tensor.

---

 Descriptors INIS/EDB

---

 Available on request from:
Information Service Department, Risø National Laboratory  
(Afdelingen for Informationservice, Forskningscenter Risø)

P.O. Box 49, DK-4000 Roskilde, Denmark

Phone (+45) 46 77 46 77, ext. 4004/4005 · Fax (+45) 46 75 56 27 · Telex 43 116